Operation of a germanium detector in the strong magnetic field of TRIUMF's TITAN-EBIT

by

Zachary Hockenbery

Department of Physics

McGill University, Montreal

August 2018

A thesis submitted to McGill University

in partial fulfillment of the requirements

of the degree of Master of Science

Abstract

We provide results in a quest towards a detailed understanding on the consequences of operating a high-purity low-energy germanium (LEGe) detector in a magnetic field. This detector is operated at TRIUMF's Ion Traps for Atomic and Nuclear science (TITAN) facility as a part of the spectroscopy setup for the TITAN Electron Beam Ion Trap (EBIT). At the TITAN-EBIT, in-trap decay spectroscopy is performed on singly- or highly-charged radioactive isotopes for measurements to study nuclear structure, nuclear astrophysics, and fundamental interactions. To perform these experiments, the detector must be placed inside one of the radial bores of the EBIT's superconducting Helmholtz coils where it can be as close as ∼100 mm from the central axis of the coils. At this location the magnetic field strength at the Ge crystal is simulated to be approximately 60% of the maximum value occurring at the center of the coils. To study the performance of our detector in the magnetic field, we use three different data acquisition devices: an Ortec Digital Gamma-Ray Spectrometer (DSPEC), a Mesytec MDPP-16 time and amplitude digitizer, and a Lecroy Wavesurfer 3054 oscilloscope. We study the leakage current through the detector as well as the characteristics of the radiation-induced voltage steps. Results confirm that the detector's leakage current does increase under the influence of the magnetic field, but we did not see a significant change in characteristics of the voltage signals. We also study the photon spectra using ^{133}Ba and ^{137}Cs calibration sources. Results show that when the magnetic field value is increased from 0 T to 2.5 T, the resolution of the detector deteriorates, but the

detection efficiency is not affected. For stronger values of the maximum magnetic field, the resolution and detection efficiency are severely affected.

Résumé

Nous fournissons des résultats dans la quête d'une compréhension détaillée des conséquences de l'exploitation d'un détecteur de germanium de basse énergie et haute pureté (LEGe) à l'intérieur d'un champ magnétique. Ce détecteur est opéré dans les installations du "TRIUMF's Ion Traps for Atomic and Nuclear science" (TITAN) dans le cadre du montage spectroscopique du "Electron Beam Ion Trap" (EBIT) de TITAN. Au TITAN-EBIT, la spectroscopie de désintégration effectuée à même le piège à ion est réalisée sur des isotopes radioactifs à charge simple ou multiple pour des mesures visant à étudier la structure nucléaire des atomes, l'astrophysique nucléaire et les interactions fondamentales. Pour réaliser ces expériences, le détecteur doit être placé dans l'un des alésages radiaux des bobines Helmholtz supraconductrices de l'EBIT, où il peut se rapprocher jusqu'à ∼100 mm de l'axe central des bobines. À cet endroit, la force du champ magnétique appliqué sur le cristal de germanium est simulée comme étant approximativement égale à 60% de la valeur maximale retrouvée au centre des bobines. Pour étudier les performances de notre détecteur dans le champ magnétique, nous utilisons trois dispositifs d'acquisition de données : le "spectromètre à rayons gamma numérique" (DSPEC) dévelopé par Ortec, le "numériseur de temps et d'amplitude MDPP-16" de Mesytec et l'oscilloscope "Wavesurfer 3054" de Lecroy. Nous étudions le courant de fuite à travers le détecteur ainsi que les caractéristiques des pas de tensions induits par les radiations. Les résultats confirment que le courant de fuite du détecteur augmente sous l'influence du champ magnétique, mais nous n'avons pas con-

staté de changement significatif des caractéristiques des pas de tension. Nous étudions également les spectres des photons en utilisant des sources de calibration de ^{133}Ba et ^{137}Cs. Les résultats montrent que lorsque la valeur maximale du champ magnétique est comprise entre 0 et 2,5 T, la résolution du détecteur se détériore, mais l'efficacité à détecter de événements n'en est toutefois pas affectée. Pour des valeurs plus élevées de champ magnétique maximal, la résolution et l'efficacité à détecter de événements sont gravement affectées.

Acknowledgements

I would like to thank Professor Thomas Brunner for giving me the opportunity to work at McGill under his guidance. Thank you for the experiences traveling to TRIUMF and LBNL and for the support and patience while I wrote this thesis. I also thank the entire TITAN team for their diligence and lightheartedness. During the few months that I visited, I learned so much and I enjoyed every minute of it. I look forward to being back for my PhD! I am also very grateful to Robert Schneider of Mesytec, Andreas Ruben of Wiener and Pierre-André Amadruz and Chris Pearson of the DAQ group at TRIUMF. Their technical support in helping to prepare the MDPP-16 for experiment S1478 was crucial to the results presented in this thesis.

I also want to thank everyone who provided useful feedback at the International Workshop on Germanium Detector Technology 2017 in Berkeley, California. In particular, to David Radford of Oak Ridge National Laboratory for his insightful remarks and suggestions. Without them, I might have spent a significant time rambling and not getting much done.

Lastly, I am thankful to my family and friends for their support and interest in my work. Thank you mom for reminding me to take a break and relax. Thank you dad for sending me all of your new music so I can rock out while I work.

Preface and Contributions of Authors

All chapters of this thesis were written by myself, the author. I gratefully acknowledge the support and assistance of the following people for their contributions to this work:

- The data analysis detailed in section 3.2 was made possible by the preceding work of Thomas Brunner. Thomas performed all of the work to setup and collect this data.

All figures in chapter 4 were created by the author. All data acquisition with the MDPP-16 was performed by the author with a VME controller and the default programming provided by Mesytec. All data analysis presented in this work was performed by the author.

Contents

List of Figures

List of Tables

Chapter 1

In-trap decay spectroscopy at the TITAN facility

1.1 The TITAN experimental setup at TRIUMF

Located in Vancouver, BC, TRIUMF is Canada's premier particle accelerator center, providing for research in the areas including particle physics, nuclear physics, nuclear medicine, materials research and accelerator and detector development [1]. The hub of TRIUMF that allows for such research is the 520 MeV H^- cyclotron [2] that is capable of delivering multiple proton beams simultaneously at different energies to various experiments. Currently, the facilities which receive beam from the cyclotron are the Isotope Separator and Accelerator (ISAC) facilities, the Center for Molecular and Materials Science (CMMS), and the Proton Treatment Facility. The ISAC facilities house a number of experiments for research with radioactive ion beams (RIBs) [3]. The CMMS provides beams of spin-polarized muons and lithium-8 for materials research covering a wide range such as superconductors, semiconductors and batteries [4].

The process begins with a source of H^- ions that are directed to the cyclotron to be accelerated. The cyclotron is able to cater to various beamlines with multiple beam

energies by using thin graphite foils placed at various radii. The thin graphite foils strip the two electrons from the proton which is then directed out of the cyclotron to beamlines. Beam line 2A provides 500 MeV proton beams at up to 100 μA to the ISAC facilities [5], which use the Isotope Separator On-line (ISOL) method to produce the RIBs. The ISOL method at TRIUMF bombards thick high power targets with the high energy proton beam to induce spallation and fragmentation reactions and produce the desired radioactive species [6].

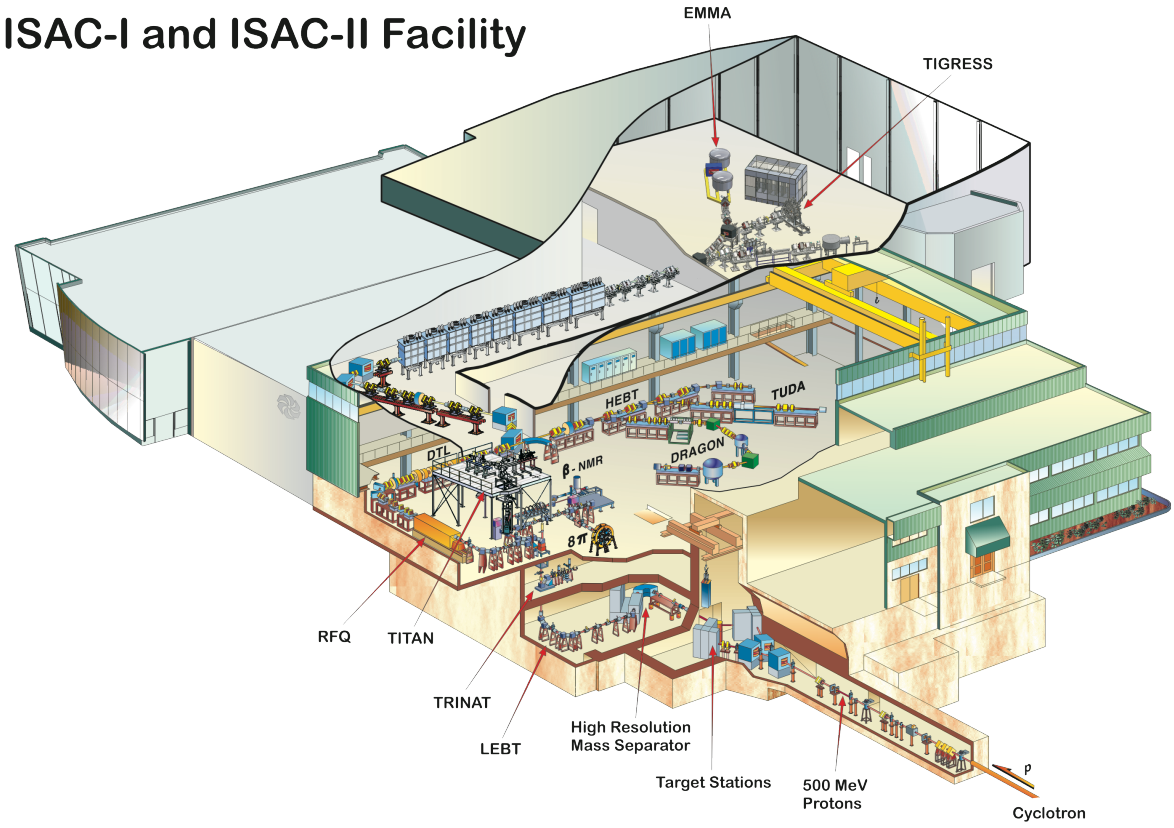

Figure 1.1: The ISAC facility at TRIUMF houses many experimental setups including TITAN. Figure reproduced from [7]

Figure 1.1 depicts the ISAC RIB target station with the connected experiments as well as the post-accelerator stages. The target material is composed of many thin foils that are stacked along the axis of the proton beam [8]. The reaction products are formed in neutral charge state in the target material and quickly diffuse to the target

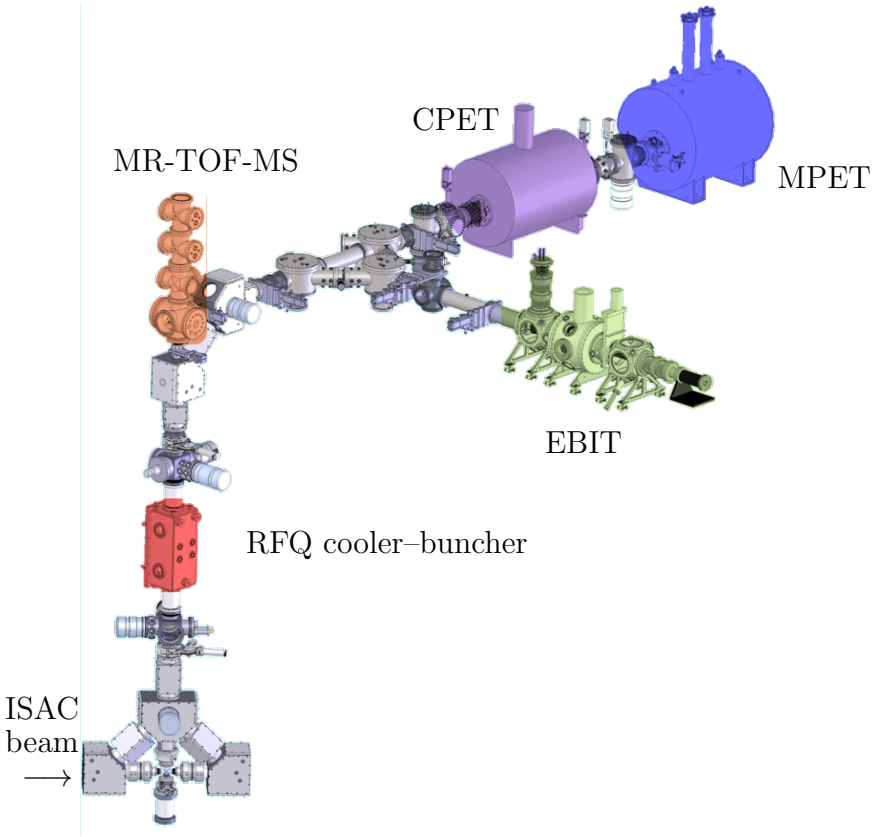

Figure 1.2: The TITAN experimental setup in the ISAC-I experimental hall at TRIUMF. Precision measurements in ion traps require a low-energy, low-emittance, bunched RIB. As such, the RIB from ISAC first reaches the RFQ Cooler-Buncher in preparation for measurements at the MPET or the EBIT. Figure from [11].

surfaces where they are then ionized to be guided to ISAC experiments. A number of available ion sources including surface, plasma (FEBIAD) and laser (TRILIS) are coupled in close proximity to the targets to deliver the required isotopes [5]. After RIB generation, the cocktail containing various isotopes is cleaned by the use of two dipole magnets which spatially separate the ensemble based on mass-to-charge ratio with a resolving power of $m/\delta m \approx 2500$ [9]. RIBs are then delivered to the two experimental areas called ISAC-I and ISAC-II. TRIUMF's Ion Trap's for Atomic and Nuclear science (TITAN) facility is located in ISAC-I in the low-energy area of the experimental hall [10], where it receives continuous RIB with energies ranging from 20–40 keV.

The TITAN experimental setup is a system of multiple ion traps dedicated to

high-precision mass measurements of short lived radioactive isotopes and in-trap decay spectroscopy. There are currently five ion traps at TITAN and they are the buffer gas-filled radio frequency quadrupole linear Paul trap (RFQ Cooler and Buncher) [12], the multi-reflection time of flight mass spectrometer (MR-TOF-MS) [13], the TITAN electron beam ion trap (EBIT) [14], the cooler penning trap (CPET) [15] and the measurement penning trap (MPET) [16]. An illustration of the TITAN setup is shown in figure 1.2. The high-precision mass measurements are primarily performed at the MPET and the in-trap decay spectroscopy is performed at the EBIT. The main research fields that these measurements contribute to are nuclear structure, nuclear astrophysics and fundamental interactions and symmetries. Historically, measurements at TITAN have been used as input for reaction paths in nuclear astrophysics (r-process [17, 18], rp-process [19]), tests of fundamental properties (symmetries [20], nuclear models [21, 22]), nuclear structure (shell closure [23], halos [24, 25], shape coexistence) and neutrino physics (Q values [26, 27, 28]). In addition, TITAN holds the record for the shortest-lived isotope ever measured in a Penning trap (Lithium-11 at $t_{1/2} \approx 8.75$ ms [24])

The TITAN system has a versatile layout and can be used in a number of configurations for experiments. The choice of which traps to use largely depends on the type of measurement, the required precision of the measurement, the half-life of the nuclide of interest, and production yields from ISAC. Descriptions of the ion traps are given below. This thesis is centered around the in-trap decay spectroscopy experiments at TITAN-EBIT, so more detail about the EBIT is given.

1.1.1 RFQ cooler and buncher

Ion trapping facilities for precision measurements require RIBs that are bunched and have a low emittance, low energy dispersion and low kinetic energy [29, 30]. As such, the first ion trap that the typically singly charged RIBs from ISAC encounter at TITAN is the RFQ linear Paul trap [31]. RIB from ISAC is continuous and transported to TITAN

at $\sim$ 20 keV and the RFQ linear Paul trap is used to bunch and cool the beam in preparation for injection to the MR-TOF-MS, EBIT, or MPET. The RFQ is equipped with a set of four RF driven quadrupole rods to confine the ions radially. These rods are spaced such that the inner diameter of the ion trap is $\sim$20 mm [12]. These rods are also longitudinally segmented into 24 pieces that are individually bias-able and used to accumulate and bunch the ions. This is achieved when the DC potentials are used to drag the ions near to the end of the trap where they are accumulated as a small cloud. The total length of the trap is $\sim$700 mm. The emittance of the beam is reduced through collisions with a He buffer gas which is injected to the trap volume at a pressure of 1×10^{-2} mbar [12] and retards the ions down to a few keV. When sufficiently cooled, an extraction potential is applied and the RIB is extracted as a pulse from the RFQ and transported at an energy of $\sim$2 keV to the next ion trap.

1.1.2 The multi-reflection time of flight mass spectrometer

The RIBs created at ISAC are cleaned with two dipole magnets that have a mass resolution of $m/\delta m \approx 3000$. This results in a strong isobaric contamination that restricts access to certain nuclei of interest for mass measurements and in-trap decay spectroscopy at the TITAN facility. Therefore, an MR-TOF-MS based isobar separator has been added into the TITAN system. As shown in figure 1.2, the MR-TOF-MS is placed directly after the RFQ cooler and buncher. The TITAN MR-TOF-MS uses a novel RFQ-based switchyard for injection and ejection from the device [32]. The ions are injected as bunches into a time-of-flight (TOF) analyzer where they travel with a kinetic energy of $\sim$1300 eV and are reflected for many turns by two electrostatic reflectors. Also inside of the TOF analyzer is a fast electrostatic deflector that is used to deflect the ions that fall outside of a desired mass range. The desired ions are then sent back through the RFQ switchyard, allowed to accumulate, and transported to the other ion traps. A commissioning experiment for the MR-TOF-MS demonstrated a

mass resolving power a factor of 6 higher than the dipole magnets at ISAC [13].

1.1.3 The Electron Beam Ion Trap

The TITAN EBIT was designed and built at the Max Planck Institute for Nuclear Physics (MPIK) in Heidelberg, Germany and had its commissioning experiment at TITAN in 2008 [14, 33]. It is a versatile trap that can be used for two purposes: a) to perform in-trap decay spectroscopy on trapped radioactive nuclei and b) to provide highly charged ions (HCI) to other ion traps in the TITAN system. The predominant mode of operation is to provide HCI to MPET to increase the precision of the mass measurements (see section 1.2). Shown in figure 1.3 is a simple illustration of the

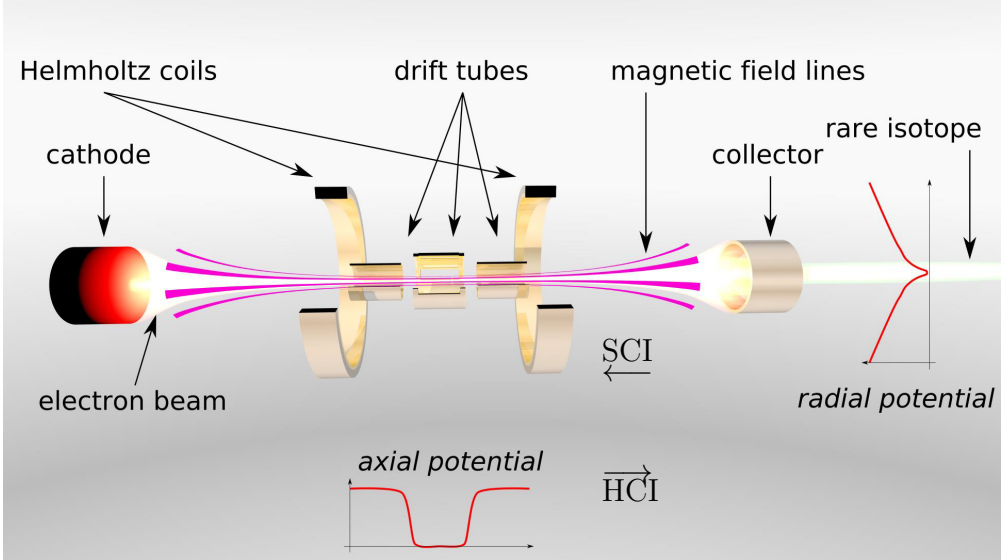

Figure 1.3: Illustration of the concept of an EBIT. Singly charged isotopes are injected axially from the right side into the trap center where they are trapped by the axial potential. They are then charge bred to the desired A/q and subsequently extracted from the EBIT as HCI. Figure from [34].

concept of an EBIT. An electron beam is generated at a hot cathode and accelerated through the trap center towards a cooled collector-electrode where it decelerates and is collected. In the trap center the electron beam is radially compressed by a strong magnetic field [35]. The magnetic field is created by two superconducting coils that

are in a semi-Helmholtz arrangement and can reduce the electron beam radius to tens or hundreds of μm, providing current densities in the thousands of A/cm^2 [14]. As an ion trap, the EBIT provides radial confinement of ions with the magnetic field and the radial potential well created by the space charge of the electron beam. Axial confinement of the ions is provided by a segmented structure of individually bias-able electrodes called drift tubes which create an axial potential. The electron beam exists not only to confine the ions radially but also to further ionize them by successive electron impact ionization [36]. Electron impact ionization occurs when the electrons carry enough kinetic energy to overcome the binding energy of a bound electron in the atomic shell. Provided that there is sufficient overlap between the electron beam and the ion cloud, the high density of the electron beam may quickly evolve the charge state of the ions. As such, the EBIT finds good use as a charge breeding machine. In 1994, the Super-EBIT at Lawrence Livermore National Laboratory (LLNL) produced bare uranium (U^{92+}) with its 200 keV electron beam [37]. For reference, the ionization energy of U^{91+} is about 130 keV [37].

Shown in figure 1.4 is a Solidworks rendering of the TITAN-EBIT with the main components highlighted. The electron gun of the TITAN-EBIT is equipped with a hot cathode that is capable of producing 500 mA beams with energies up to $\sim$4 keV [33]. The energy of the electron beam is chiefly determined by the potential difference between the hot cathode and the drift tubes. After the electron beam is produced at the cathode it is directed through the drift tube structure of the EBIT. The whole of the drift tube structure is made of nine axial segments and the central trap electrode is made of eight radial segments, for a total of sixteen electrodes. The drift tube structure is thermally coupled to the two superconducting coils which are used to produce a 6 T field at the trap center. A two-stage Gifford-McMahon helium cryo-cooler is used to cool the superconducting magnet and thermally coupled drift tubes to $\sim$4.5 K [14]. The electron beam is then decelerated and collected at the water-cooled collector. The

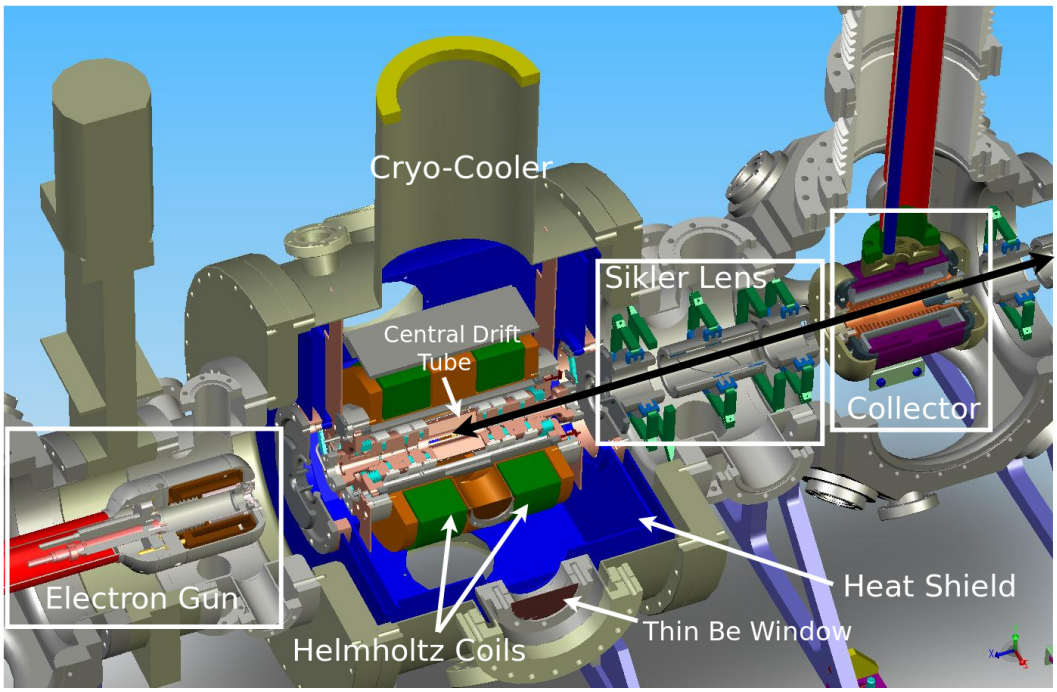

Figure 1.4: A Solidworks rendering of the TITAN-EBIT. RIB from ISAC are bunched and cooled by the RFQ and sent to the EBIT where they are injected into the trap center from the Collector side. The black arrow indicates the injection and extraction directions. Figure reproduced from [38].

combination of the cryogenic system and the vacuum pumps contribute to a vacuum in the trap chamber that is approximately 2×10^{-9} mbar [33].

The three steps to EBIT operation for HCI production are injection, charge breeding and extraction. During injection, the ions are guided into the trap by the drift tubes, which are equipped with fast high voltage switches to trap the ions into a potential well. As the ions evolve in charge state, they fall deeper into the radial potential well of the electron beam until they reach their highest charge state. The highest charge state is chiefly determined by the energy of the electron beam, which must be higher than the ionization energy to continue charge breeding. Depending on the species and desired charge state, charge breeding can take on the order of tens of ms [33]. A rough estimate of the number of elementary charges that can be stored within the EBIT is that it is proportional to the electron beam current and inversely proportional to the square-root of the electron beam energy [39]. At the TITAN-EBIT, roughly 10^9

electrons can be stored, which translates to about 10^7 HCIs with a charge state of 30^+ [39].

In the EBIT, charge breeding to a desired mass-to-charge ratio (A/q) results in a distribution of charge states around a specific A/q. This is due to a number of interactions that work against electron impact ionization, with the predominant being charge exchange (CE) with the environment. Maintaining a strong trap vacuum and cooling down to 4 K combats this as contaminants are adsorbed onto trap surfaces. Other processes including radiative recombination (RR) and dielectronic recombination (DR) can also work against electron impact ionization. The RR process is when a free electron falls into a vacant energy level of the ion. This process is written as,

$$A^{Z+} + e^- \longrightarrow A^{(Z-1)+} + \gamma, \tag{1.1}$$

where Z is the atomic number, γ represents a photon, and e^- represents an electron. The DR process is similar to the RR process, but the recombined electron also promotes a bound electron to an excited state. This is a resonant process and the doubly excited state decays by the emission of a photon.

To illustrate the charge breeding process in an EBIT for typical operational parameters, consider the plot given in Figure 1.5. This plot is generated by a program which simulates the temporal evolution of the charge state distribution in an EBIT. This ionization balance is calculated using empirical cross sections for electron impact ionization [41] and requires the parameters electron energy E_{e^-}, current I and the overlap between the electron beam and ion cloud. It also accounts for the effects of charge exchange with a background pressure, radiative recombination and dielectronic recombination.

In section 1.1.1 it was mentioned that precision ion traps such as the MPET require bunched beams with a low emittance and a low energy dispersion. Extraction of HCI

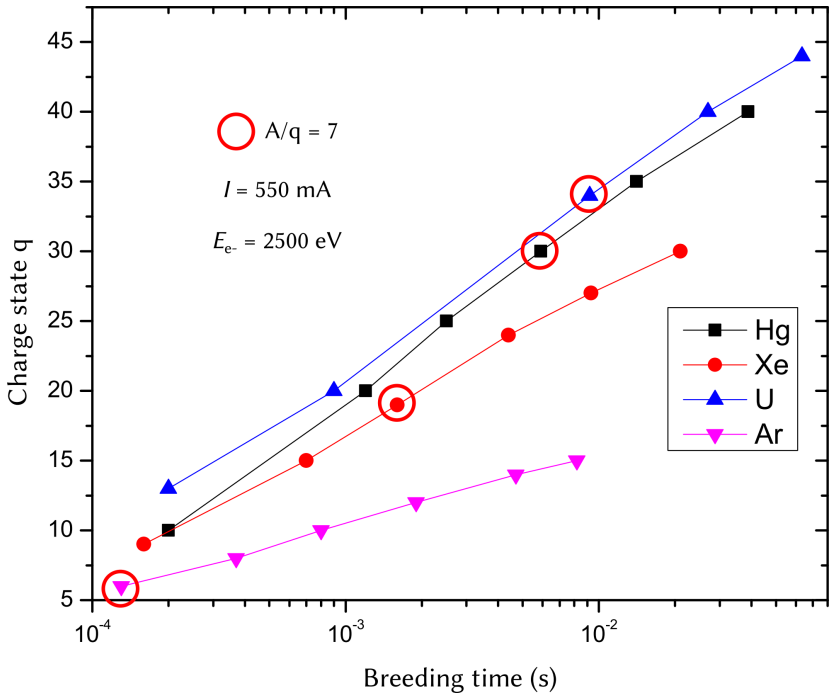

Figure 1.5: An example plot of the simulated temporal evolution of the ionization balance of Hg, Xe, U and Ar in an EBIT. The values for beam current I and electron energy E_{e^-} are given as well as red circles denoting where $A/q = 7$. Figure reproduced from [40].

from the EBIT pose a number of problems that must be overcome to prepare the HCI beam for the MPET. The charge breeding process introduces energy to the ion ensemble through collisions with the electron beam. In addition, switching electrode potentials during extraction of the HCI from the EBIT introduces kinetic energy to the ion ensemble. In general, EBIT extraction energy spread is on the order of 10 eV/q [42], while the MPET accepts energy spreads on the order of 1 eV/q [43]. For comparison, the RFQ Linear Paul trap is able to deliver SCI to MPET with an energy spread less than 10 eV [12]. In large part, this cannot be mitigated through modifications to EBIT extraction methods without losing a significant number of ions.

The solution to this problem is the Cooler PEnning Trap (CPET) which is currently being commissioned off-line at TITAN. This trap is designed to reduce the emittance of RIB for MPET by sympathetic cooling with electrons [15]. This trap is not relevant to the subject of this thesis and is not discussed further.

1.2 High precision mass measurements with the Measurement Penning Trap

At the crux of the TITAN program for mass measurements is the MPET. Once ions are injected into the trap, radial confinement is achieved with a strong 3.7 T solenoid magnet. Under the influence of a homogeneous magnetic field in the z-direction, the ions perform a circular motion with angular cyclotron frequency [44]:

$$\omega_c = \frac{qB}{m}, \tag{1.2}$$

where the magnetic field strength is B, and the charge-to-mass ratio of the ion is q/m. Since the magnetic field does not provide axial confinement, an additional axially symmetric electrostatic quadrupole field is used to provide full three-dimensional trapping

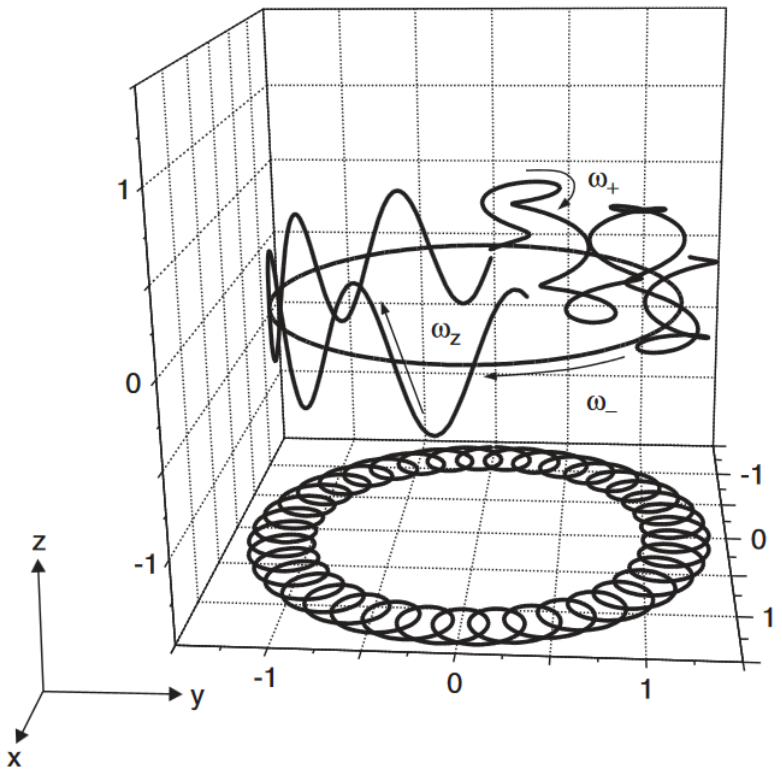

Figure 1.6: The three independent eigenmotions in a Penning trap. The axial motion is ω_z, the magnetron motion is ω_- and the reduced cyclotron motion is ω_+. The azimuthal RF quadrupole excitation couples the two eigenmotions in the radial plane, ω_- and ω_+. A conversion of the amplitude of the magnetron motion to the reduced cyclotron results in an increase in the radial kinetic energy of the ion. Figure reproduced from [29].

of the ions. This incites ion motion which is composed of three harmonic eigenfrequencies ω_z (axial), ω_- (magnetron) and ω_+ (reduced cyclotron) [44]. The cyclotron motion is the combination of the magnetron and reduced cyclotron motions in the radial plane perpendicular to the B-field: $\omega_c = \omega_- + \omega_+$. Figure 1.6 illustrates the eigenmotions of an ion in an ideal Penning trap. Mass measurements are then performed by determining the cyclotron frequency.

In the context of Penning traps, a number of methods for performing mass measurements are available. The Fourier Transform Ion Cyclotron Resonance (FT-ICR) [45] method measures currents induced by ion motion on the trapping electrodes. The Phase Imaging Ion Cyclotron Resonance (PI-ICR) method [46] maps the phase of an

ions motion in the trap onto a position sensitive detector. The MPET at TITAN employs a destructive method known as time of flight (TOF) [47] which measures the time of flight of ions after ejection from the trap onto an ion detector positioned away from the traps magnetic field.

To perform the TOF method, ion motion is excited by exposure of the ions to a RF electromagnetic field for a short period of time. This RF excitation selectively perturbs and manipulates the amplitudes of the modified cyclotron, magnetron and axial motions of the ions and can be used for cleaning the trap of unwanted species or to determine the eigenfrequency of the motion. With the appropriate choice of frequency and amplitude of an azimuthal RF quadrupole excitation, the amplitude of the magnetron motion can be converted completely to the modified cyclotron motion [48], resulting in an increase in the radial kinetic energy of the ions. This resonant coupling occurs at an applied frequency $\omega_{rf} = \omega_- + \omega_+$ and results in a beating between the two different modes. Upon release from the trap, the ion is accelerated by the gradient of the magnetic field towards the ion detector. This force to accelerate the ions towards the detector is proportional to the radial energy of the ions, so ions with a larger radial kinetic energy will reach the detector quicker. By scanning the excitation frequency and measuring the ion TOF for repeated experimental cycles, a resonance curve is built. Since the ions that are non-resonantly excited arrive slower than those that are resonantly excited, the curve displays a minimum in TOF when $\omega_{rf} = \omega_c$.

The relative statistical precision of the measured mass is given by [49]:

$$\frac{\delta m}{m} \propto \frac{m}{qBT_{rf}\sqrt{N}} \tag{1.3}$$

where T_{rf} is the time duration of the RF excitation, m and q the ion mass and charge state, N the number of ions measured, and B the magnetic field. Trapping facilities such as SMILETRAP have demonstrated the benefit of using stable HCI to increase

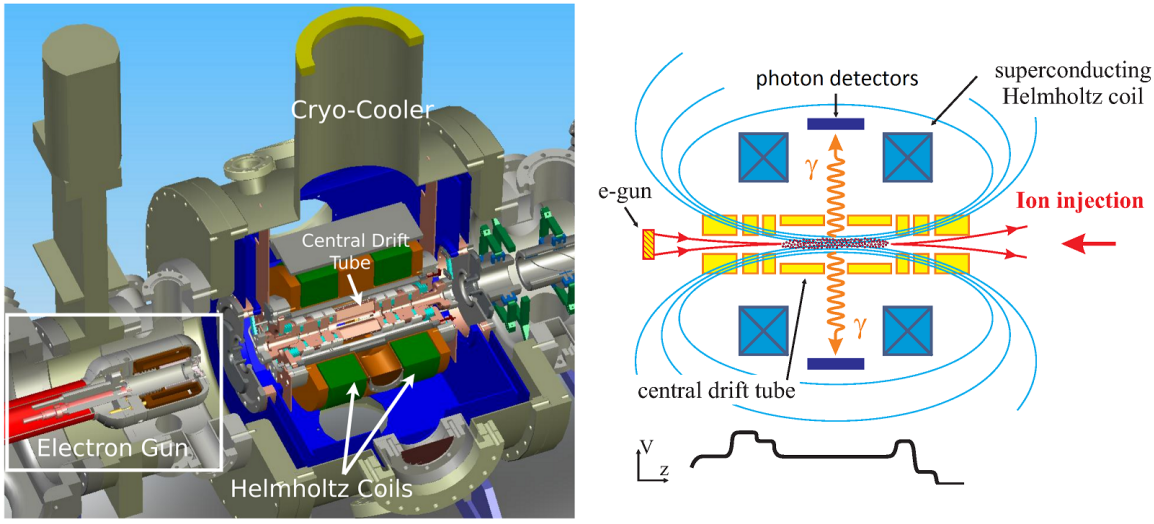

Figure 1.7: **(left)** a Solidworks rendering of the EBIT showing the central drift tube which is azimuthally segmented . **(right)** an illustration of the spectroscopy setup at the TITAN-EBIT (not to scale). The bottom plot shows the landscape of the axial potentials applied to the drifts tubes during EBIT operation. Figure reproduced from [52].

measurement precision [50]. The measurable relative mass precision is proportional to the charge state, therefore HCI outperform SCI. For this reason, the TITAN-EBIT is used as a charge breeder to provide HCI for mass measurements at the MPET.

In 2007 the TITAN program came on-line and began experiments. In 2008, the mass of the short-lived two-neutron halo nucleus ^{11}Li ($t_{1/2} \approx 8.8$ ms) was measured using SCI [24]. This is the shortest lived isotope ever measured in a Penning trap. In 2011, the mass of the lightest known two-neutron halo nucleus ^{6}He was measured [25]. Also in 2011, TITAN first used the HCI method with MPET to determine the mass of ^{74}Rb ($t_{1/2} \approx 65$ ms) in the 8+ charge state [51].

1.3 The TITAN-EBIT for in-trap decay spectroscopy

In addition to its capability as a charge breeder for MPET, the TITAN-EBIT allows for spectroscopic measurements of stored ions. Shown in figure 1.7 **(left)** is the EBIT geometry and **(right)** is an illustration of the in-trap spectroscopy setup (not to scale).

The horizontal bore of the magnet coils allows passage of the electron beam and ions. In addition, the magnet housing offers radially oriented bores between the coils that allow direct access to the central drift tube of the trap. The central drift tube is azimuthally segmented into eight pieces with slit apertures between each segment. The apertures are oriented at 45° from each other and each have a 35 mm radius opening which allows photon detectors direct access to observe the x-rays and gamma-rays originating from the trap center.

Development of in-trap decay spectroscopy methods at TITAN-EBIT have been primarily fueled by an experimental proposal by D. Frekers, J. Dilling, and I. Tanihata [53]. This letter proposes to use the TITAN-EBIT to measure the highly-suppressed electron capture (EC) branching ratios (BRs) of the odd-odd intermediate nuclei of the double beta ($\beta^-\beta^-$) decay parents. Measurements of the EC BRs provide an important experimental input for nuclear matrix calculations in two-neutrino double-beta ($2\nu\beta\beta$) decay and subsequently provide help in understanding neutrinoless double-beta ($0\nu\beta\beta$) decay. In most cases, the EC branches are highly suppressed ($3-5$ orders of magnitude) in comparison to the β^- counterparts. In this setup, the novelty of the EBIT for measuring the EC BRs is the suppression of the β-induced background by the strong magnetic field.

This thesis work builds upon the pioneering thesis work of T. Brunner [54] and A. Lennarz [38] which contain the bulk of the work that has been done so far to develop methods for in-trap decay spectroscopy at the TITAN-EBIT. This experimental technique is referred to as TITAN-EC, but with the current 2γ proposal (see section 1.3.3), we are moving towards decay spectroscopy. A description of the spectroscopy setup and a brief explanation of the in-trap spectroscopy methods developed for TITAN-EC is given below.

A structure (see figure 1.8) built around the trap center of the EBIT is used to support up to seven detectors mounted perpendicular to the electron beam axis. The

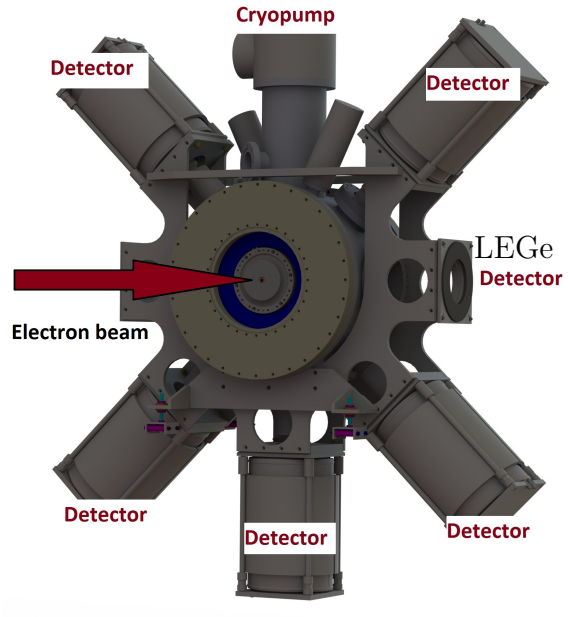

Figure 1.8: A Solidworks rendering of the spectroscopy setup around the trap center of the TITAN-EBIT. The top port is where the cold finger for the two-stage liquid-He cryogenic system is inserted to cool the magnet and drift tube assembly. The central ring shown in the figure is the housing for the EBIT magnet. Solidworks geometry obtained from [55].

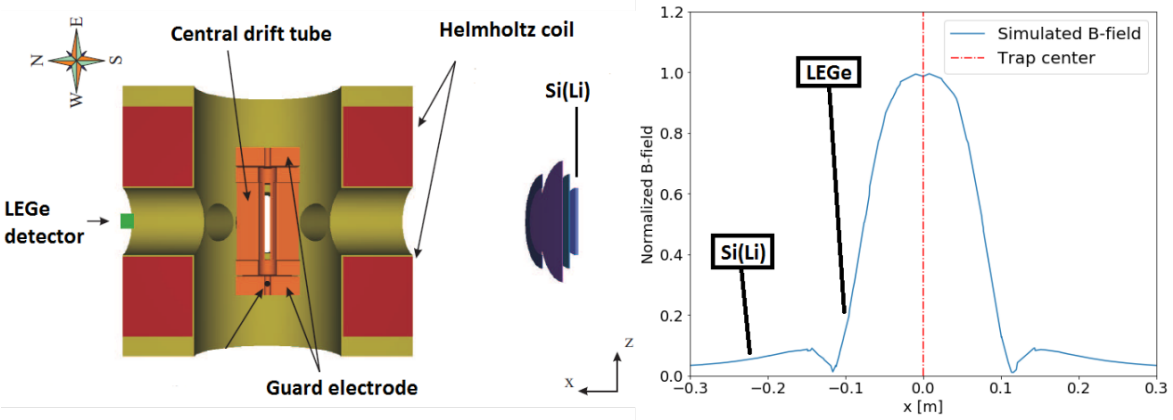

Figure 1.9: **(Left)** a drawing (not to scale) to illustrate the positions of the LEGe and a Si(Li) detector in the EBIT spectroscopy setup. The removal of a Be window from the EBIT vacuum chamber allows the LEGe to be placed inside of the radial bore of the magnet. **(Right)** a simulation of the normalized B-field transverse to the direction of the electron beam in the trap center. The approximate locations of the LEGe and Si(Li) detectors are given. The locations of the Si(Li) detectors are permanent, but the LEGe can be moved in or out. The LEGe position shown is with full extension in towards the trap center. Drawing reproduced from [54] and simulation performed with COMSOL Multiphysics® [56].

current setup is featuring six lithium-drifted silicon (Si(Li)) semiconductor diode detectors and one high-purity low energy germanium (LEGe) semiconductor diode detector (model № GUL0110P), all manufactured by Canberra Industries. Depending on the mounting port, the six Si(Li) detectors are located at distances of 226 or 230 mm from the trap center and have a total geometric acceptance of ∼1.8 % of the total 4π solid angle [38]. To act as vacuum barriers and heat shielding, each Si(Li) detector capsule has a 0.25 mm thick Be window [38]. In addition, the EBIT vacuum chamber has 0.8 mm thick Be windows on all ports containing Si(Li)'s [38].

This thesis work is focused on the LEGe detector (mounting port indicated in figure 1.8). The detection element is a small disk (10 mm thickness × 11.3 mm diameter) that is housed in an aluminum endcap with a thin 25 μm Be window. This endcap is mounted at the tip of a retractable cryostat which allows extending the detector element to as close as ∼100 mm to the trap center [54]. To allow such access, the Be window in the EBIT port is removed and the only window between the detector crystal

and the trap center is the 25 μm Be window on the endcap [57]. A schematic of the retractable cryostat and LEGe endcap is given in appendix A.

Figure 1.9 **(left)** illustrates (not to scale) the positioning of the LEGe and a Si(Li) detector near the trap center of the EBIT. The positioning of the LEGe is as a means to maximize the solid angle of the detector for measuring weak x-rays and gamma-rays. At this position, the geometric acceptance of the LEGe detector is $\sim 0.08\%$ of the total 4π solid angle [58]. A consequence of placing the LEGe so near to the trap center is that it is operated in the region of the strong magnetic field. Figure 1.9 **(right)** shows a simulation of the normalized B-field transverse to the direction of the electron beam in the trap center. A review of current literature on semiconductor detectors operating in magnetic fields is given later in section 1.4.

1.3.1 TITAN-EBIT as a spectroscopy Penning trap

As progress towards measuring EC BRs in transition nuclei in $\beta\beta$ decay, the thesis work of T. Brunner [54] demonstrated the feasibility of in-trap decay spectroscopy by successfully measuring the EC BRs of ^{107}In and ^{124}Cs. This was achieved by using the TITAN-EBIT as an open-access spectroscopy Penning trap. In this configuration the electron beam of the EBIT is turned off and the trap electrodes are used to create a static electric quadrupole potential for axial trapping of SCI that are injected into the trap. Radial trapping of the ions is provided by the strong magnetic field. With the electron beam turned off the electron gun is replaced by a β particle detector and x-ray detectors are positioned around the trap center as discussed in section 1.3.

Figure 1.10 illustrates the EBIT setup for this experiment. Singly charged RIB from the RFQ cooler buncher is injected into the EBIT and stored in the trap center while the measurement takes place. In this configuration, storage times are typically on the order of 1 second [59]. The EC decay mode emits characteristic x-rays from atomic electronic transitions to the K or L shell and these would normally be washed out by

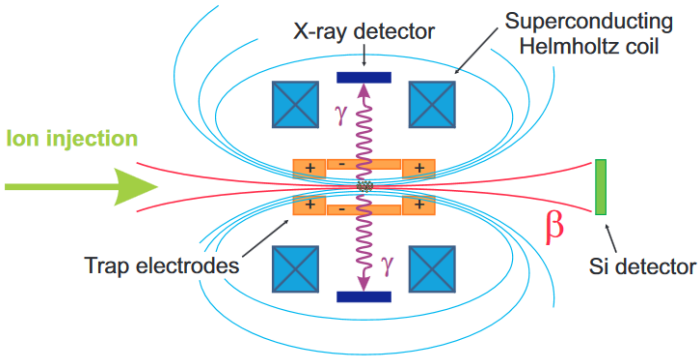

Figure 1.10: An illustration of the TITAN-EC setup. Figure reproduced from [59].

the competing β particle contamination. The uniqueness of using the EBIT for these measurements is that the strong axial magnetic field radially constrains β particles from reaching the x-ray detectors positioned around the trap center, thus lowering the background of the measurement. The β particles are instead guided out of the trap center by the magnetic field lines and onto the β particle detector as shown in figure 1.10. The β-detection is used to determine the number of isotopes that are stored in the trap.

1.3.2 In-trap decay spectroscopy with HCI

In later developments of this technique, the EBIT was used in its intended operation mode: ions were captured and stored by charge breeding them to HCI for in-trap spectroscopy. This was performed with an in-trap experiment of radioactive ^{124}Cs [60, 38] and successfully demonstrated two objectives: a) suppression of the β-induced background by spatial separation of the β particles and b) longer ion storage times in the trap using HCI and a special cooling method to allow decay studies of short- and medium-lived isotopes. As discussed earlier, the ions are trapped in an axial potential well and by the radial space charge of the electron beam. An ion with a charge state Z_i in a potential well V_w must then have an energy greater than eZ_iV_w to escape from

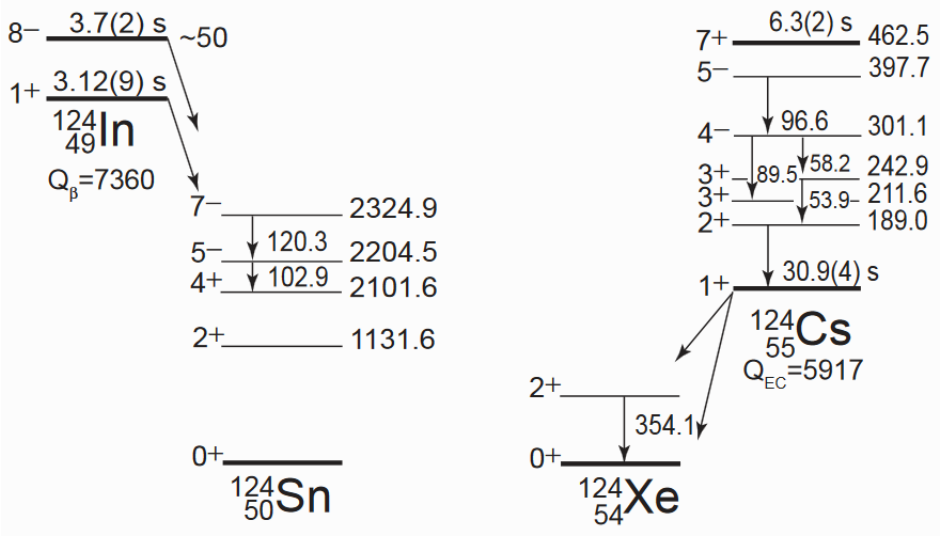

Figure 1.11: The decay schemes of ^{124}Cs and ^{124}In. Arrows indicate the transitions that were observed during the experiment. Figure reproduced from [38].

the trap [61]. For this reason, it is possible to achieve much longer storage times with HCI.

The measurement is published in full [60] and a brief summary is given here. At ISAC, a 480 MeV 9.8 μA proton beam was impinged upon a uranium carbide (UC) target and the subsequent products were surface ionized to produce a RIB. This RIB was composed primarily of two isomers of ^{124}Cs ($J^{\pi} = 1^{+}$ and 7^{+}) and a contamination of ^{124}In in 8^{+}. The decay schemes of both of these are shown in figure 1.11. In the EBIT, the RIB bunch was bombarded with an 85 mA electron beam at energies of 1.5 and 2.0 keV to produce charge states ranging between 26 and 32 in approximately 100 ms. These charge states correspond to a complete removal of the N shell and partial removal of the M shell.

Measurement periods consisted of 20 seconds of trapping and measurement time and 10 seconds of background measurement while the trap was empty. Six Si(Li) detectors were used to record time-stamped photon spectra in the X-ray region and one HPGe detector was used to monitor the ions in the trap by observing γ-ray events.

Following the EC decay of ^{124}Cs to ^{124}Xe with a half life $t_{1/2}$=30.9 s, there are

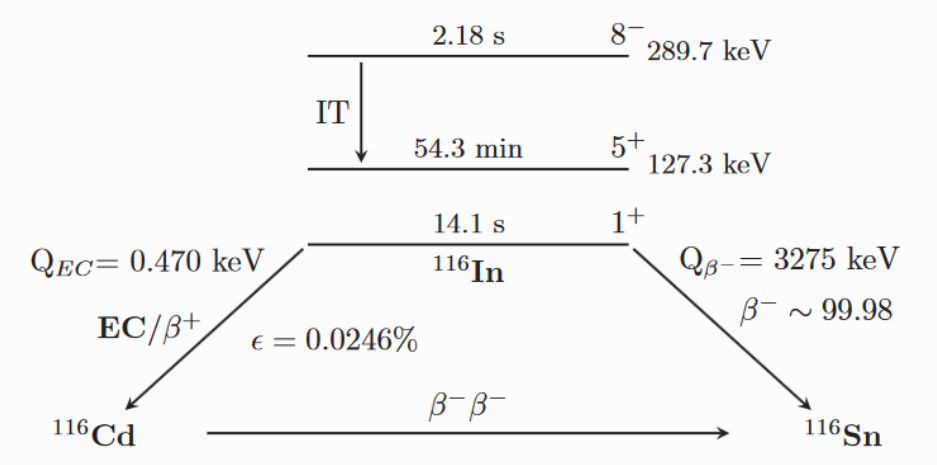

Figure 1.12: A partial decay scheme of ^{116}In and some of its lowest isomeric states. Figure reproduced from [38].

two x-ray peaks at 29.7 keV and 33.7 keV. Also in this region are x-rays from internal conversion of the metastable ^{124}Cs state ($t_{1/2}$=6.3 s) and the contaminant ^{124}In ($t_{1/2} \approx$ 3 s). The time-dependence of the photon spectra showed a disappearance of the short-lived components and a successive enhancement of the signature from the ^{124}Cs EC mode. To make the EC BR measurements, one needs to cross-check with intensities of other reliable photopeaks such as high intensity γ-rays. In this case, the ^{124}Cs ground state populates not only the ground state of ^{124}Xe, but also the first excited 2^+ state at 354.1 keV with a transition intensity of 47 %. With the observation of the 354.1 keV γ-ray peak, one can calculate the number of ^{124}Cs ground-state decays. This number has to be consistent with the number of EC decays observed within the same measurement period. In this experiment, they were consistent with each other and this proved the capability to measure the EC BRs with the EBIT setup.

In addition to the commissioning experiment above, a first attempt at measuring EC BRs of relevant isotopes for $\beta\beta$ decay was made. The ^{116}Cd isotope is capable of double beta decay to ^{116}Sn. The isotope ^{116}In can decay through EC/β^+ to ^{116}Cd with a very weak branch of ∼0.0246% and through β^- to ^{116}Sn with a strong branch of ∼99.98% [62]. Through isomeric transitions and β^- decay, the isomers of ^{116}In can

also contribute to the population of the ^{116}Sn state. In this way, ^{116}In is called a transitional/intermediate nucleus in $\beta\beta$ decay. This decay scheme is illustrated in figure 1.12. Due to limited experimental time and problems with ISAC beam stability, the experiment did not obtain enough total collected statistics to observe the weak EC branch ($\sim$0.02 [62]) of the ^{116}In ground state to ^{116}Cd. However, the experiment did demonstrate the ability to use a multiple-injection technique [63] for storing a larger number of ions in the EBIT trap. This technique offers the obvious advantage of allowing more statistics to be gathered per measurement shift. Future in-trap decay spectroscopy measurements are planned and experimental proposals have been accepted by the TITAN Experiments Evaluation Committee (EEC). Currently accepted proposals are S1066 [64], S1478 [65], S1622 [66], and S1695 [67].

1.3.3 Proposals for future measurements

Recently, a TITAN experimental proposal (experiment number S1695) to study nuclear 2γ-decay at the TITAN-EBIT facility was accepted by the TRIUMF EEC [67]. A second order process analogous to $\beta\beta$-decay, 2γ-decay is an electroweak process where two γ quanta are simultaneously emitted during a single quantum transition. In the past, measurements of 2γ-decay have only been performed on nuclei where both ground and first excited states have $J^{\pi}=0^{+}$ spin-parity. In the few species that exhibit this condition, γ-decay is forbidden between the two states by conservation of angular momentum. This condition is termed non-competitive 2γ-decay and has already been observed in ^{16}O [68] , ^{40}Ca [69, 70], and ^{90}Zr [71, 69].

In nuclei that do not exhibit the spin-parity sameness between ground and first-excited states, it is much more difficult to observe 2γ-decay because the matrix element for γ-decay is several orders of magnitude larger. However, a recent experiment [72, 73] was able to measure the branching ratio of *competitive* 2γ-decay (written as $(\gamma\gamma/\gamma)$), the nuclear transition where the competing γ-decay is not forbidden. This measurement

was performed on the ∼662 keV transition of the $11/2^-$ isomer of ^{137}Ba decaying to its $3/2^+$ ground state. This measurement was made possible with high efficiency LaBr detectors with moderate energy resolution and significant measurement time to provide evidence for contributions from the 2γ branch. Good timing resolution was critical to identifying and removing coincident events from sequential Compton scattering between detectors. The observed distributions in energy and emission angle provide evidence for dominant M2–E2 and minor E3–M1 contributions to the 2γ branch in competition with the M4 γ-transition. A Quasiparicle Phonon model is in good agreement with the experimental results [72]. The $(\gamma\gamma/\gamma)$-decay BR was measured at $\sim 10^{-6}$.

The uncommon spin-parity sameness between ground and first excited states is also exhibited in ^{72}Ge, ^{98}Zr and ^{98}Mo. However, despite the forbiddenness of γ-decay in these isotopes, the alternative decay mode internal conversion (IC) is present and competes with and overwhelms the 2γ-decay mode. The IC decay mode is when an excited nucleus electromagnetically interacts with and ejects an inner shell electron [74]. If these isotopes can be charge-bred to the bare state, the IC mode can be suppressed and the 2γ-mode is much more accessible. In the specific case of these $0^+ \rightarrow 0^+$ transitions, the width of nuclear de-excitation through 2γ emission to the final state can be approximated as [68],

$$\Gamma_{2\gamma} = \frac{\omega_0^7}{105\pi}\left(\alpha_{E1}^2 + \chi_{M1}^2 + \frac{\omega_0^4}{4752}\alpha_{E2}^2\right), \tag{1.4}$$

where ω_0 is the transition energy, χ_{M1} is the magnetic dipole transition susceptibility, and α_{E1} and α_{E2} are the electric dipole and quadrupole transition polarizabilities of

the final ground state, respectively. The full distribution is given as [68],

$$\begin{aligned}\frac{d^2\Gamma_{2\gamma}}{d(cos(\theta))d\omega_1} =& \frac{\omega_1^3\omega_2^3}{\pi}\Bigg[\alpha_{E1}^2+\chi_{M1}^2+\frac{\omega_1\omega_2\alpha_{E2}\chi_{M1}}{6}+\frac{\omega_1^2\omega_2^2\alpha_{E2}^2}{144}+(4\alpha_{E1}\chi_{M1})cos(\theta)\\ &+\left(\alpha_{E1}^2+\chi_{M1}^2-\frac{\omega_1\omega_2\alpha_{E2}\chi_{M1}}{2}-\frac{3\omega_1^2\omega_2^2\alpha_{E2}^2}{144}\right)cos^2(\theta)\\ &-\frac{\omega_1\omega_2\alpha_{E1}\alpha_{E2}}{3}cos^3(\theta)+\frac{4\omega_1^2\omega_2^2\alpha_{E2}^2}{144}cos^4(\theta)\Bigg],\end{aligned} \tag{1.5}$$

where ω_1 and ω_2 are the energies of the two emitted photons that sum to the transition energy ω_0 and θ is the emission angle between them. As such, measurements of the energy and angular distributions of the 2γ transition provide a unique access to these nuclear structure observables. The experiment proposed for TITAN-EBIT relies upon using the high charge states and long storage times achievable in the EBIT to suppress these competitive decay modes and to measure the complete decay of the 0_2^+ isomers in the trap. These cases have implications for studies of nuclear shape coexistence [67, 75] and also for evaluating properties of 0^+ states near the $0\nu\beta\beta$ decay candidates ^{76}Ge, ^{96}Zr, and ^{100}Mo [67]. Table 1.1 lists some properties of the three measurement

Nuclide	ω_0 [MeV]	$t_{1/2}^{gs}$ [s]	$t_{1/2}^{0_2^+}$ [ns]	$\Gamma_{2\gamma}/\Gamma_{total}$
^{72}Ge	0.691	stable	444.2(8)	–
^{98}Zr	0.854	30.7(4)	64	–
^{98}Mo	0.735	stable	21.8(9)	–

Table 1.1: 2γ-decay candidate properties. Table reproduced from [67].

candidates [62], in particular the half-lives which are much shorter than the ion trapping times demonstrated in the EBIT. In addition, the other techniques developed for TITAN-EC for background suppression and time dependent photon spectrum analysis demonstrates that the EBIT is particularly well suited for a 2γ experiment. The placement of the seven detectors allows for angular correlations at 45°, 90°, 135°, and 180° for two-coincidence photons. However, the current Si(Li) detectors will need to

be replaced by a set of HPGe detectors to achieve better detection efficiencies in the region of spectroscopic interest. In the case of ^{72}Ge and with current ISAC production yields and beam transport efficiencies taken into account, it is estimated that a rate of approximately 32 2γ decays per second would occur inside of the EBIT [67]. Furthermore, with the spectroscopic setup detailed in section 1.3, it is estimated that approximately 2.6×10^{-3} of all 2γ decays will have one photon detected and 1.8×10^{-5} of all 2γ decays will be detected in coincidence with two detectors [67].

1.4 Semiconductor detectors in magnetic fields

An impediment to the continued development of the in-trap decay spectroscopy program at TITAN-EBIT is the operation of the very-precise semiconductor diode detectors in the vicinity of the magnetic field of the EBIT. It was mentioned earlier that one of the beryllium windows in the trap has been removed to allow a LEGe detector to be placed very near to the trap center. The reason for this is to utilize a larger solid angle when measuring characteristic x-rays from the weak EC BRs in the experiments mentioned earlier. A side effect of this is that the LEGe detector is placed inside of the strong magnetic field of the EBIT. Throughout the long history of the development of semiconductor detectors, a few studies of how a magnetic field affects detector operation have been made [76, 77, 78, 79, 80, 81]. Studies by Belau *et al.* [79], Castoldi *et al.* [80] and Pandey *et al.* [81] have focused on the effects of magnetic fields on silicon strip detectors designed for high resolution tracking of charged particles. Studies by Sanchez Lorente *et al.* [77], Szymanska *et al.* [76], and Agnello *et al.* [78] have focused on gamma-ray spectroscopy with coaxial HPGe detectors operating in magnetic fields.

The two general concerns when operating a semiconductor detector within a magnetic field are **1)** that the signal created within the detection medium by incident radiation may be altered by the magnetic field and **2)** that the magnetic field may

increase the amount of noise in the detection system. In the case of number 1, the event signal is subsequently incorrectly processed by the electronics readout system leading to a faulty measurement or no measurement at all. In the case of number 2, the increased noise is registered as false events by the system or it degrades the overall resolution of the measurements.

In brief, the studies involving silicon strip detectors observed how signal transport properties within the detection medium differ as a function of the applied electric and magnetic fields at various relative orientations. They concluded that the tracking resolution of the detectors was lessened due to the detector signal being distorted by the magnetic field. They also remarked that the resolution could be retained if the detectors are oriented with a field-strength-dependent rotation perpendicular to the magnetic field vector. The general magnetic field range was $0 - 4.7$ T and the thickness of the detectors was on the order of 300 μm. As a part of the signal readout electronics, all studies used charge sensitive field effect transistor (FET) amplifiers which were also engulfed in the magnetic field. None reported any problems caused by operating the FET amplifiers in the magnetic field.

The studies for gamma-ray spectroscopy with coaxial HPGe detectors in magnetic fields have focused on detection efficiency, energy resolution, and measurement stability over time. Sanchez Lorente *et al.* studied magnetic field effects on the 1.332 MeV gamma-ray line from a radioactive ^{60}Co source for a magnetic field up to 1.6 T. Szymanska *et al.* used a magnetic field up to 0.8 T to study the effects on six different gamma-ray sources with photopeak energies ranging from 0.088 to 1.33 MeV. Agnello *et al.* used a magnetic field up to 2.5 T to study the effects with various crystal orientations and with three different radioactive sources with gamma-ray energies ranging from 0.060 to 1.33 MeV.

General conclusions from HPGe studies are that the effect of the magnetic field is some combination of **a)** reducing the detection efficiency by increasing the number of

counts lost and **b)** altering the photopeak spectrum through distortion of the charge collection process in the detection volume. Both of these effects can be attributed to either the deflection of charge carriers in the sensitive detection volume due to the Lorentz force or an enhanced Penning ionization effect in the vacuum surrounding the detector crystal [77]. From the discussions in sections 1.3.1 and 1.3.3 it is clear that the magnetic field raises some concerns for in-trap decay spectroscopy experiments at TITAN-EBIT.

In the magnetic field range used by Szymanska *et al.*, there was no significant observation of a loss in detection efficiency. However, at the higher magnetic fields used by Agnello *et al.*, a moderate loss in detection efficiency which increased with gamma-ray energy was observed. All studies observed a shifting and broadening of photopeaks that was more severe at higher gamma-ray energies and lead to a reduced energy resolution. In performing these studies, Agnello *et al.* and Sanchez Lorente *et al.* were both able to determine correlations between the magnetic field strength and the effects of the photopeak distortion. This allowed them to apply a correction to the photopeak spectrum and to partially recover some of the resolution lost through the effects of the magnetic field.

Paper	Type	Geometry	B-field [T]	Magnet and positioning
Szymanska *et al.*	n	Closed-ended coaxial	0 – 0.8	Center of Helmholtz coil
Agnello *et al.*	n	Closed-ended coaxial	0 – 2.5	Center of solenoid
Sanchez Lorente *et al.*	n	Tapered hexagonal closed-ended coaxial (EUROBALL cluster)	0 – 1.4	Center of Helmholtz coil
	n	Closed-ended coaxial (VEGA detector)	0 – 1.6	

Table 1.2: Some of the characteristics of past studies of HPGe in magnetic fields

To conclude this section, table 1.2 lists some general characteristics of the studies performed with HPGe detectors. Briefly mentioned in section 1.3 is that our detector

has the geometry of a small cylindrical disk and can be positioned only in the fringe field of a two-coil dipole magnet. It is also a p-type HPGe crystal (more detail in chapter 2). These characteristics distinguish our situation from the studies listed in table 1.2. Therefore, in addition to these studies being required for the development of in-trap decay spectroscopy at TITAN, we report observations to this area of research.

Chapter 2

Theory of Semiconductor Detectors

In this section we give an introduction to the theory and operation of HPGe detectors for gamma-ray spectroscopy. A more detailed exposition can be found in the textbooks by G. Lutz [82], H. Spieler [83] or G. F. Knoll [84]. Unless otherwise cited, the information given in this chapter comes from one of these three textbooks. For figures and equations reproduced from the textbooks, we explicitly cite which one was used.

2.1 Introduction

The radiation detector is a useful tool in the physicist's toolbox for observing physical processes that occur at scales not directly observable by humans. To construct a radiation detector, the physicist must first find a medium that will reliably and predictably interact with the radiation to produce a signal. Next, the physicist must devise a method for observing and storing the signal for later analysis. In practice, there is always some amount of noise produced within the detection medium or other instruments involved in the detection system. This noise needs to be limited such that the signal from the incident radiation can be identified with good resolution. The science of radiation detection covers a wide range of topics and applications: astronomical observations, integrated circuit analysis, medical imaging, and more recently gravitational

waves to name a few.

Since the discovery of radiation that carries enough energy to ionize most molecules and atoms, many types of radiation detectors have been developed for specific applications to detect, identify and/or track the different types of ionizing particles [85, 86]. Depending on the desired measurement, detector types can be classified as tracking detectors, dosimeters, or counting detectors and in general they are based upon either photographic emulsion, scintillation light, or direct ionization mechanisms [87]. In many cases of radiation detection, a complex arrangement of detection mechanisms is used to infer as much information about the incident radiation as possible.

At TITAN-EBIT we are most interested in accurately measuring the energy of x-rays and gamma-rays emitted from singly- or highly-charged radioactive ions as they decay in the trap. In the context of nuclear physics, a gamma-ray is any photon emitted from the nucleus during a nuclear process like radioactive decay or a nuclear reaction. Gamma-rays from radioactive decay are typically characterized as being within the energy range of 100 keV to 10 MeV [84]. A characteristic x-ray is any photon emitted from an atomic transition. In many cases, a characteristic x-ray is emitted from an excited daughter state following a radioactive decay. These are most commonly observed as the result of an electron in the L shell decaying to a vacancy in the K shell (K_α). Other transitions such as M shell to K shell (K_β) and M shell to L shell (L_α) are observed, but with less intensity than K_α lines. Characteristic x-rays are generally within the energy range of 100 eV to 100 keV [84].

Gamma spectroscopy provides access to a variety of observables about excited nuclear states that are used to scrutinize theoretical models and study unique phenomena: energies and intensities provide information about nuclear energy levels and their positions; emission times provide information about radioactive lifetimes; polarization can provide information about spin and level parity; and angular correlations and distributions can provide information about shape deformation and nuclear transition

moments, among other observables [88]. In a similar manner, x-ray spectroscopy can provide useful information about atomic structure observables.

2.2 Spectroscopy with photons

In the historical development of radiation detectors for ionizing radiation, the detection of gamma-rays has provided a significant challenge due to their uncharged nature. Charged particles will continuously transfer energy to most media via the Coulomb interaction, but gamma-rays will often pass through a medium unnoticed. It is for this reason that they are classified as *deeply penetrating* radiation and require detectors with special designs to increase the probability of interaction. A number of possible mechanisms for interaction between photons and matter exist; the primary modes are the photoelectric effect, the Compton effect, and pair production [84].

In the photoelectric interaction mode, the incident photon interacts with an entire atom and is absorbed. In its place is an electron (called a *photoelectron*) that is ejected from the atomic shell with energy [84],

$$E_{e^-} = h\nu - E_b, \tag{2.1}$$

where $h\nu$ is the incident photon energy and E_b is the initial binding energy of the ejected photoelectron. As the energy of the incident photon increases, the origin of the photoelectron becomes closer to the tightest bound K and L shells of the atom. After the interaction, the lone ion will then capture a free electron from the medium and/or the electrons in the atomic shells will rearrange [84]. This results in at least one characteristic x-ray that will either escape the medium or be absorbed in another interaction.

In the Compton interaction mode, the incident photon interacts with an electron and is scattered at an angle θ with respect to the angle of incidence. Depending upon

the scattering angle, the outgoing photon retains only a portion of the incident energy and this is given as [84],

$$h\nu' = \frac{h\nu}{1 + \frac{h\nu}{m_0c^2}(1 - \cos(\theta))}, \tag{2.2}$$

where m_0c^2 is the rest-mass energy of the electron. The outgoing photon will either escape the medium or undergo another interaction. The pair production mode of interaction occurs at photon energies above ∼1.02 MeV (twice the electron rest-mass energy) [84] which is outside of the range of spectroscopic interest at TITAN-EBIT so we will forgo its description.

Depending upon the characteristics of the medium and the energy of the incident photon, these interactions will lead to either a partial or a full transfer of the energy of the photon to the the medium. In principle, it is desirable that the incident photon is fully absorbed, liberating many electrons from the atoms and thereby creating mobile charge carriers within the detection medium. The motion of these mobile charge carriers in the presence of an applied electric field is then the fundamental electrical signal that gives indication of a radiation event.

Figure 2.1 shows the regimes of the three main photon-matter interaction processes as functions of the atomic number (Z) of the atoms and incident photon energy. The photoelectric effect has a cross section that is proportional to $\sim Z^{4-5}$, while for Compton scattering it is proportional to $\sim Z$, and for pair production to $\sim Z^2$ [90]. As such, a crucial aspect of material selection is the effective atomic number because this will dictate how the signal within the medium is generated. If a low to medium number is chosen, the increased number of Compton interactions leads to a higher probability of photons escaping after depositing only a portion of their energy. The signal from this type of partial-deposition event is undesirable because it is not an accurate representation of the source and thus contributes to the background. Therefore, there are essentially only two paths through which a photon's energy can be fully deposited: directly through the photoelectric effect or through a cascade of multiple Compton

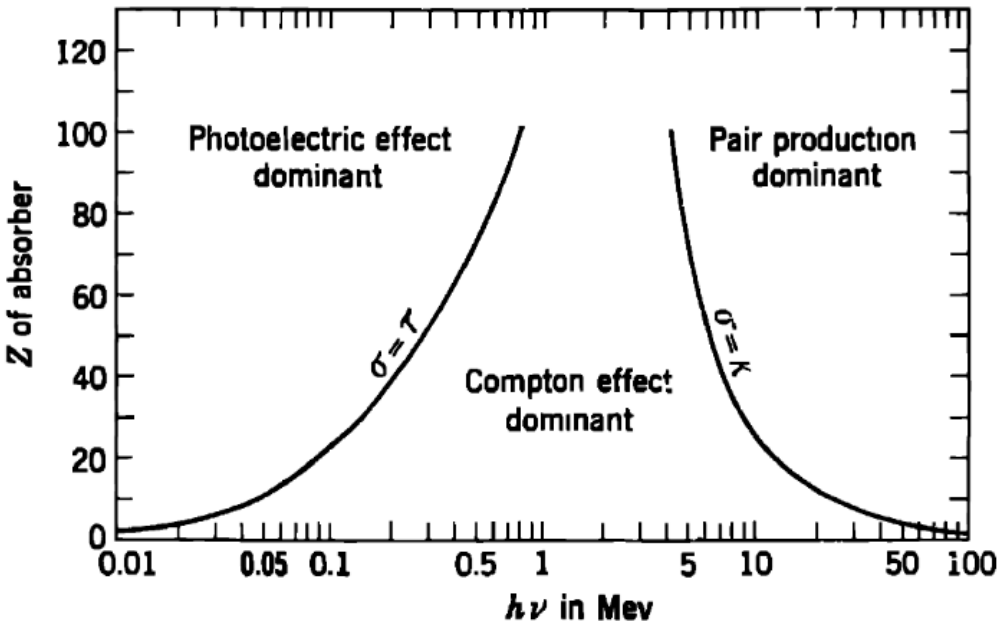

Figure 2.1: The three most dominant interaction processes between γ-rays and matter with atomic number Z. The lines at $\sigma = \tau$ and $\sigma = \kappa$ trace the values of Z and $h\nu$ where the neighboring processes are equal. Figure reproduced from chapter 25 of the textbook *The Atomic Nucleus* by R. D. Evans [89].

scattering events ending with the photoelectric effect. It is for this reason that a higher Z material with more electron density is generally preferred when choosing a detection medium.

Currently a number of detector types with liquid, gas or solid media are available for x-ray and gamma-ray spectroscopy. Among these, scintillation and semiconductor detectors are the most preferable for good energy resolution and full-energy photon peak efficiency [84]. When choosing between these types for a specific detection application, it is always a trade off between the pros and cons of each. Scintillation detectors operate by measuring low-energy photons generated in a scintillating material in response to incident gamma-rays. A photomultiplier tube (PMT) is then used to observe and convert the low-energy photons to an electrical signal via the photoelectric effect [87]. One of the first scintillation materials was thallium-activated sodium iodide (NaI(Tl)) and since then other materials such as bismuth germanate ($Bi_4Ge_3O_{12}$/BGO [91]) and

cerium doped lanthanum bromide ($LaBr_3$(Ce) [92]) have become available. Generally, scintillation detectors provide good density, high Z and large volumes but in comparison to modern semiconductor detectors they are limited in resolution due to the relatively large amount of energy required to produce a photoelectron. On average, a scintillation detector requires 100 eV to produce a photoelectron [84]. For a typical gamma-ray, this results in only a few thousand charge carriers contributing to the produced electrical signal. Statistical fluctuations in such a small number place an intrinsic limitation on the achievable resolution of scintillation detectors. The only way to overcome this limit is to produce more charge carriers per incident photon.

In contrast to scintillation detectors, semiconductor detectors function by directly collecting charge carriers that are created by the photon interactions. They have much better resolution than scintillation detectors and are therefore preferred for x- and gamma-ray spectroscopy, when high spectroscopic detail is important [86]. On average, the energy to produce a photoelectron in a semiconductor is about two orders of magnitude smaller than a scintillation detector [84]. As such, a typical incident gamma ray will produce many more charge carriers which in turn leads to a better resolution.

There are currently many semiconductor materials available to use in a radiation detector: silicon (Si), germanium (Ge), cadmium telluride (CdTe), and gallium arsenide (GaAs) to name a few. During the early development of semiconductor detectors, lithium (Li) atoms were drifted into semiconductor materials to compensate for intrinsic crystal impurities [93]. This lead to the development of lithium-drifted silicon (Si(Li)) detectors and lithium-drifted germanium (Ge(Li)) detectors, which perform well with short-range radiation such as alpha particles. However, the most pressing limitation with semiconductor detectors was to create a semiconductor crystal with a volume sufficient for deeply penetrating gamma-rays. In the 1970s, techniques were developed by a research group in Berkeley, California [94, 95] to fabricate large volume high purity germanium (HPGe). This is the crucial development that has allowed Ge to supplant

other semiconductor materials for high resolution spectroscopy. HPGe detectors are now the most widely used and preferred detectors for high resolution x-ray and gamma-ray spectroscopy [96, 97, 90].

2.3 High purity germanium semiconductor detectors

A bulk of pure germanium semiconductor material is structured as a crystalline periodic lattice within which an electron can only occupy certain allowed energy states [82]. In intrinsic semiconductors such as Ge and Si which have an electron valence of 4, this lattice structure is due to the strong covalent bonding between the atoms. Electrons which exist in valence shells are bound to specific sites within the crystalline lattice and are said to be in the *valence band*. At a higher energy and adjacent to the valence band is the *conduction band*, wherein electrons are free to migrate throughout the crystal. The spacing between the valence and conduction bands is known as the *bandgap*.

2.3.1 Charge carrier creation

When a photon enters the detection medium and interacts through one of the mechanisms described in section 2.2, an electron is liberated from the valence band and promoted to the conduction band, thereby leaving an empty space in the valence band. This empty space in the valence band is termed a *hole* and will act as a quasiparticle due to the aggregate motion of electrons in the valence band [82]. As such, an electron and hole are always created together as an electron-hole (e–h) pair and they can both contribute to the signal generated by incident radiation.

Table 2.1 lists the material properties of some semiconductor materials in comparison to Ge. The reader will notice that the energy required for the creation of an e–h pair is larger than the bandgap energy. This is because a portion of the deposited

Property	Si	GaAs	Ge	CdTe
Density (300 K) [g/cm^3]	2.33	5.32	5.33	5.85
Average atomic number Z	14	31.5	32	50
Bandgap (300 K) [eV]	1.115	1.43	0.665	1.44
e–h creation energy (77 K) [eV]	3.76	4.2	2.96	4.43

Table 2.1: Material properties for different semiconductor media. Values from [84]

energy will contribute to vibrations in the lattice (phonon excitations) [98].

In the absence of ionizing radiation, an electron can also be promoted to the conduction band by thermal excitations. In practice it is desirable that the number of charge carriers created by thermal excitations is far less than those produced by the radiation one wants to detect. The probability per unit time and unit volume that an e–h pair is thermally generated is given by [84]:

$$p(T) = CT^{3/2}\exp\left(-\frac{E_g}{2k_BT}\right), \tag{2.3}$$

where T is the absolute temperature, k_B is the Boltzmann constant, E_g is the bandgap energy and C is a constant that depends upon the semiconductor. The quotient in the exponential tells us that this probability is critically dependent upon the temperature and the bandgap energy of the semiconductor. Therefore, practical solutions for minimizing thermally generated noise are to operate the detector at a reduced temperature or to increase the bandgap of the material.

In Table 2.1 we gave the bandgap energies of pure Si and Ge, but in practice it is very difficult to manufacture a semiconductor crystal with absolute purity. The level of impurities within a semiconductor strongly dictate the electrical characteristics of the material and if these impurities have a valence of 3 or 5 they are considered *shallow impurities* [84]. When an impurity of valence 5 is inserted into a lattice of Ge, the extra electron does not participate in strong covalent bonding and is therefore loosely bound and easily susceptible to thermal excitations [84]. This process is illustrated in Figure 2.2 where the impurity is called a *donor* atom. If a small concentration of these donor

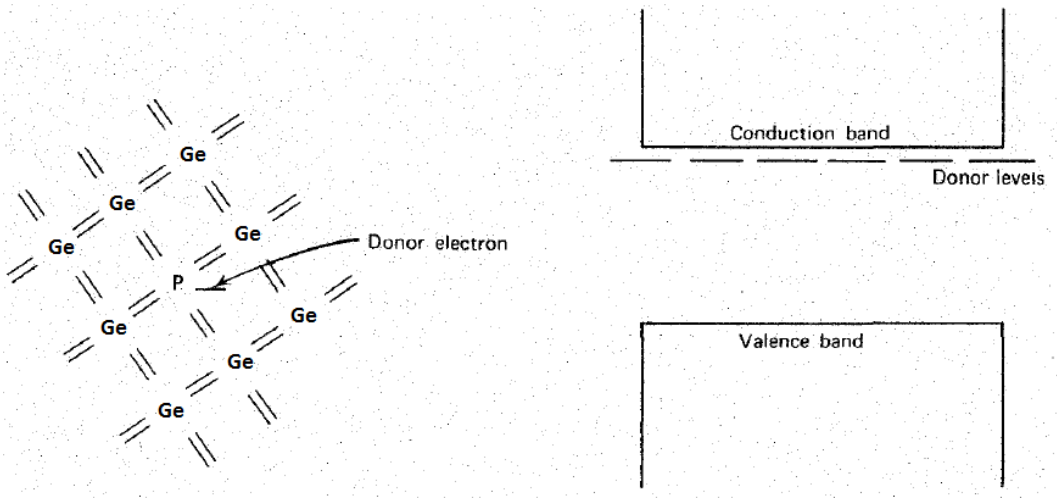

Figure 2.2: An illustration showing a valence 5 impurity (phosphorus) inserted into a lattice of Ge atoms. Figure taken and modified from [84].

impurities are evenly distributed within a lattice of Ge, the extra electrons will populate an energy state that is above the valence band but slightly below the conduction band of the intrinsic Ge material. Since the promotion of the donor electrons to the conduction band does not leave behind any holes, a large number of electrons populate the conduction band and a smaller number of holes populate the valence band. This in turn increases the e–h recombination rate and on average the holes become a minority carrier as the electrons become a majority carrier [84].

This same mechanism will occur if impurities of valence 3 are introduced to a lattice of Ge and the resulting material will have a majority of holes and a minority of electrons. When impurities are purposefully introduced into a semiconductor material the process is termed *doping*. A valence 5 impurity is called a *donor* impurity and the resulting material is called an *n-type* semiconductor. A valence 3 impurity is called an *acceptor* impurity and the resulting material is called a *p-type* semiconductor. A superscripted + such as p^+ is used to denote elevated doping concentrations in a given semiconductor. The standard for semiconductors is that HPGe material is any Ge material that contains an impurity concentration less than 10^{10} atoms/cm^3 [84]. As it

is impossible to remove all impurities, HPGe materials are usually designated as mildly p-type or mildly n-type.

2.3.2 Signal generation

In the absence of an electric field, any generated charge carriers will move throughout the medium with random thermal motion until they eventually recombine after some average lifetime has elapsed [82]. In order for the charge carriers to produce a current useful for signaling radiation events, an electric field must be placed across the detection medium to impart a net average drift velocity to the charge carriers. The net average drift velocity of electrons and holes is different in response to an applied electric field and each is given as [82]:

$$\overrightarrow{v_{e^-}} = -\mu_{e^-}\overrightarrow{E}, \tag{2.4}$$

and

$$\overrightarrow{v_h} = \mu_h\overrightarrow{E}, \tag{2.5}$$

where $\overrightarrow{E}$ is the electric field vector, and μ_{e^-} and μ_h are the mobilities of the electrons and holes, respectively. Generally this relationship is not adhered to at higher values of the electric field. As the strength of the electric field increases, the drift velocity of a charge carrier increases until it reaches a saturation point and is independent of the electric field. The mobility of a charge carrier depends upon temperature, lattice structure, and doping concentration, among other things, because these introduce scattering mechanisms [82]. In general, the saturated drift velocity of a charge carrier in a semiconductor is on the order of 10^7 cm/s [84]. With a 10 mm thick crystal, this means that a charge carrier would traverse half of the thickness in $\sim$50 ns.

Table 2.2 gives the electrical characteristics of Si and Ge and shows how the electron and hole mobilities are behave at different temperatures. It should be noted here that the current produced by an electron or a hole in the presence of an electric field cannot

Property	Ge	Si
Electron mobility (300 K) [$cm^2/(V{\cdot}s)$]	3900	1350
Electron mobility (77 K) [$cm^2/(V{\cdot}s)$]	$3.6{\times}10^4$	$2.1{\times}10^4$
Hole mobility (300 K) [$cm^2/(V{\cdot}s)$]	1900	480
Hole mobility (77 K) [$cm^2/(V{\cdot}s)$]	$4.2{\times}10^4$	$1.1{\times}10^4$
Intrinsic carrier density (300 K) [cm^{-3}]	$2.4{\times}10^{13}$	$1.5{\times}10^{10}$
Resistivity (300 K) [Ω cm]	50	$2.3{\times}10^5$

Table 2.2: Some electrical characteristics of Si and Ge given at different temperatures. Values obtained from [84].

be discerned by a simple measurement. Under the influence of an electric field the electron moves opposite to the electric field vector and the hole moves along the field vector. The currents created by both charge carriers add together to form a net current. From this point on, we will refer to the current generated by ionizing radiation as a *signal current*.

In addition to the shallow impurities mentioned in section 2.3.1, another class of impurities called *deep impurities* can exist within a semiconductor. These impurities are generally elements such as zinc, gold, cadmium or other metallic atoms and create energy states that are closer to the middle of the bandgap [84]. Deep impurities will act to degrade the signal current by temporarily or permanently removing charge carriers from the signal. In the former case, the impurity will trap a charge carrier for a period of time before eventually releasing it. If the trapping time is significant, then the charge carrier will not contribute to the signal current from the ionizing radiation. In the latter case, an impurity can act as a site where one charge carrier is first trapped and a second complementary charge carrier is then trapped at a later time. The two charge carriers recombine and the impurity site is returned to its initial state, allowing it to continue causing trapping and recombination events [84].

An important semiconductor parameter is the *charge carrier lifetime*, which is the average amount of time that a charge carrier can exist in a mobile state before being trapped or recombining. Together with the charge carrier mobility, these two param-

eters determine the performance of the detectors signal. With a high mobility, the charge carriers can be quickly collected onto the contact electrodes to contribute a signal before trapping or recombination can cause any degradation. In semiconductors, typical collection times are on the order of 10^{-7} s – 10^{-8} s while carrier lifetimes are on the order of 10^{-5} s [84].

In table 2.2, the electrical property *Resistivity* is a direct consequence of the density of mobile charge carriers and the charge carrier mobility. When an electric field is applied to the semiconductor medium, some amount of current will flow even in the absence of ionizing radiation. This current is due to the finite amount of mobile charge carriers that exist in the semiconductor due to thermal excitations. This response to the applied electric field is called the *leakage current* and depending on it's magnitude and fluctuations, it can obfuscate the signal current.

As an example calculation, consider the geometry of our detector, the GUL0110P: the surface area is 100 mm^2 and the thickness is 10 mm [57]. If we assume that the semiconductor adheres to Ohm's Law in low field [84], we can estimate the leakage current that we would observe if we apply a bias voltage:

$$I = \frac{VA}{\rho l}, \tag{2.6}$$

where V is the applied voltage bias, A is the surface area, l is the thickness, and ρ is the resistivity of the material. If we bias a pure Ge semiconductor with 500 V, the observed leakage current would be 10 A! In contrast, a typical gamma-ray will produce current on the order of $\sim \mu$A [84, 83]. To mitigate this problem, *blocking contacts* are employed. These are discussed in the next section.

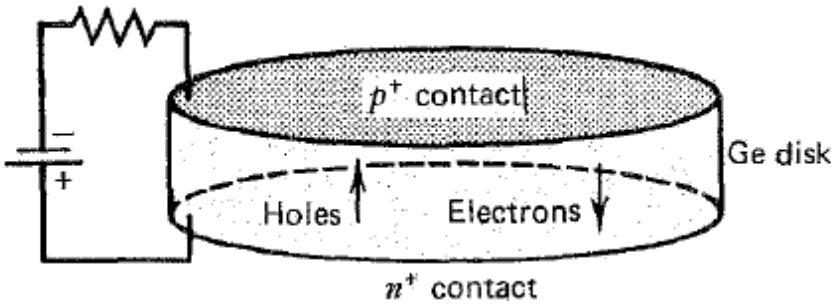

Figure 2.3: A basic HPGe detector configuration with contacts and biasing shown. In reverse biasing the crystal, a positive voltage is applied to the n^+ electrode and a negative voltage is applied to the p^+ electrode. Figure reproduced from the textbook *Radiation Detection and Measurement* by G. F. Knoll [84].

2.3.3 Contacts and signal collection

Detector contacts are crucial in the design of a semiconductor detector because they must support multiple functions. This includes application of the electric field (biasing), collection of the signal current, and the minimization of leakage current. These functions are discussed in this section.

Figure 2.3 shows the generic configuration of a disc shaped HPGe detector. Attached on either side of the Ge disc are the contacts (p^+ and n^+) and applied to these contacts is a voltage bias that places an electric field across the bulk material. The electric field is applied to induce a drift in the charge carriers such that electrons are pulled towards the n^+ contact and holes are pulled towards the p^+ contact. In this configuration of the voltage bias, the crystal is said to be *reverse biased* and the reason why is explained next.

As was mentioned earlier, the HPGe material is either mildly p-type or mildly n-type. If it is mildly p-type, then the junction between the n^+ contact and the p-type HPGe creates a semiconductor diode junction. When this p–n junction is created, some of the electrons in the n^+ material will diffuse over to the side of the p-type HPGe and recombine with the majority holes in that region. Conversely, holes in the p-type region will cross the junction and recombine with electrons in the n^+ contact.

In doing so, this creates a region that is largely depleted of thermally generated mobile charge carriers and is therefore a suitable, high resistance region for measuring signal current from ionizing radiation [84]. This region is commonly known as the *depletion region* or the *active region* of the detector.

In the absence of an applied electric field, diffusion of charge carriers across the p-n junction is eventually balanced by an opposing electric field due to the accumulation of space charge [84]. The application of a reverse bias voltage will increase the extent of the depletion region and an approximation for the thickness of the depletion region is given as [84]:

$$d = \left(\frac{2\epsilon V}{eN}\right)^{1/2}, \tag{2.7}$$

where ϵ is the dielectric constant of the medium, V is the reverse bias voltage, e is the electronic charge, and N is the net impurity concentration. The depletion region begins at the p-n junction and extends out into both the p and n regions. If the carrier concentrations on either side of the junction are not equal, the depletion region will extend predominantly into the region with a lower concentration [84]. Because the net impurity concentration N of HPGe is so low, the achievable volume of the depletion region is much larger than with other semiconductor detectors. It is for this reason that HPGe is the best type of detector for gamma-ray spectroscopy. As a voltage applied to the crystal increases, typically the maximum extent of the depletion region is achieved first. Increasing the voltage further than this will increase the electric field in the detector and thereby increase charge carrier mobilities until they reach their respective saturation points [84]. At some voltage above this, the p-n junction will breakdown and the semiconductor can no longer be used as a radiation detector. HPGe is typically operated with a voltage bias between 1 and 3 keV [84].

To fabricate the highly doped p^+ and n^+ contacts on the surface of the Ge crystal, there are two standardized methods in the semiconductor detector industry. The n^+ electrode is typically created by exposing the surface to a vapor of n-type atoms and

allowing them to diffuse through the material at a high temperature. This is commonly performed with Li atoms and typically results in contact thicknesses on the order of 0.5 to 0.6 mm [99]. To form the p^+ electrode, an accelerator is used to implant p-type ions into the surface. This is typically performed with boron ions and results in contacts that are approximately 0.3 μm in thickness [84]. There are also developments to produce contacts with amorphous Ge (a-Ge) and amorphous Si (a-Si) through a RF-sputtering deposition process [100]. This is primarily for the development of position sensitive detectors that require electrode segmentation.

When mobile charge carriers are created within the active volume of the detector, their motion induces a current on nearby electrodes [101]. In this way, charge carriers that are produced by incident radiation and then drifted by an electric field induce a current onto the contact electrodes. The signal on the contact electrodes is then amplified by a charge sensitive amplifier and processed by electronics for storage and subsequent analysis [83]. This instantaneously induced electric current is best understood by the application of the Shockley–Ramo theorem ([102] and [103]). A treatment of the Shockley–Ramo theorem for semiconductor gamma-ray detectors is given in [101] and not repeated here.

As an electron and hole are generated within the crystal and subsequently collected at their respective electrodes, an electron and hole are injected at the opposite electrodes to maintain equilibrium charge carrier concentrations in the semiconductor [84]. Therefore, contacts that block the injection of charge carriers into the semiconductor bulk, but allow transfer out of the bulk are employed [104]. These are called blocking contacts and are the reason for employing heavily doped p^+ and n^+ materials. If we consider the p-n junction diode, it is difficult to inject electrons from the p-side because the majority carrier in this place is holes. Therefore the highly doped contacts provide a barrier against this process which is called *electron/hole injection*. The ability for a single contact to block both carrier types is the reason that research efforts are being

made to produce a-Ge and a-Si contacts [100].

At this point we have discussed two out of three types of leakage current that contribute noise to the detector: thermally generated charge carriers and charge carrier injection. In the next section we discuss leakage current at the surface of the detector. A final remark to make is that it is important to consider the electrical circuit used to bias the detector. In many circuits, a large valued series resistor is used when biasing the detector for signal isolation purposes [84]. If the leakage current through the detector increases, the voltage drop across the Ge crystal will lessen and the drop across the series resistor will increase. Because most detectors are biased to a value well above the full-depletion voltage, it seems that this would only affect the charge carrier mobilities and not the extent of the depletion region.

2.3.4 Detector geometry and surfaces

In this section we consider the geometry of our detector, which is the simplest and is shaped like a disc. This is called the *planar* geometry and it is essentially made with two cross sectional cuts from an HPGe crystal ingot [99]. As such, the diameter of the crystal is constrained by the methods used to fabricate the ingot. The thickness of the crystal is constrained by the ability to fully deplete the volume of the crystal. For a mildly p-type HPGe crystal of thickness h, the voltage at which the depletion region extends fully from the side of the n^+ contact to the p^+ contact is [84]:

$$V_d = \frac{\rho h^2}{2\epsilon}, \tag{2.8}$$

where ϵ is the dielectric constant, ρ is the charge density in the material. For p-type semiconductor ρ is given as negative the product of electronic charge and the density of acceptor impurities. In the case that the applied voltage is well past this depletion

voltage, the electric field within the crystal is [84]:

$$-E(x) = \frac{V}{h} + \frac{\rho}{\epsilon}\left(\frac{h}{2} - x\right), \tag{2.9}$$

where x is the distance from the side of the n^+ contact and V is the applied voltage. As such, the electric field within a planar HPGe detector varies linearly as a function of x. The highest value is at the side of the n^+ contact and the lowest value is at the side of the p^+ contact.

All detectors have an inherent capacitance because of the build up of static charges on either side of the high resistivity depletion region. Because the increased voltage bias also increases the volume of the depletion region, the capacitance of a semiconductor detector generally decreases with increased bias until the depletion voltage is reached. The capacitance per unit area of the fully depleted planar HPGe detector is [84]:

$$C = \left(\frac{\epsilon\rho}{2V}\right)^{1/2} \tag{2.10}$$

When considering detectors for low energy x-ray or gamma-ray spectroscopy, it is imperative that there is a maximal exposure of the sensitive detection volume to the radiation source. Any inactive material in the detector is typically called a *dead layer* and is an important consideration in low-energy x-ray spectroscopy because it will disrupt the signal current [105]. This disruption occurs because these layers do not provide a good electric field for charge carrier mobility. For performance in the low-energy x-ray and gamma-ray region, the semi-planar geometry is usually preferred ([106, 107] and chapter 12 of [84]). The primary reason for this is because it is easy to maximize the active volume of the detector and reduce *dead layers* [84].

There are two sources for dead layers in a semiconductor detector: the contacts themselves and the surfaces between the contacts. As was mentioned earlier, the p^+ contact formed by ion implantation is much thinner than the n^+ contact. Because of

this, a planar HPGe detector purposed for low energy x-rays will generally be configured such that the thin p^+ contact is facing the radiation source. This thin front-facing contact is sometimes referred to as an *entrance window* for low energy x- and gamma-rays.

In addition to the dead layers between the contacts and the fully depleted region, the side surfaces of the crystal need to support the bias voltage placed across the contacts with a high resistivity. Although the crystal structure of Ge in the bulk of the crystal is highly symmetric, the termination of the crystal at the surface leads to a strong disturbance [82]. The open bonds at the surface rearrange and the lattice in this region is distorted. If the surface is left bare, it will react with whatever chemicals are in the ambient atmosphere and humidity of the detector enclosure. Therefore it is good practice to intentionally place a passivating layer on top of the exposed crystal surface. Chemical passivation is used to prevent interactions with the atmosphere and electrical passivation is used to avoid creating states in the electronic band structure at the surface [108]. Exposure to air usually results in the formation of an oxide layer and for silicon detectors, SiO_2 is a good and stable passivation layer. However, germanium oxides are unstable so passivation is usually carried out by sputtering with a-Ge or SiO_2 [90]. Depending on passivation methods, it has been shown that the depth of the passivated surface dead layer is on the order of mm and varies considerably in thickness between the p^+ and n^+ contacts [109, 90].

It is also well known that over time active charges can accumulate in surfaces and form p-type or n-type regions which affect the charge collection process [110, 111]. These are called surface channels and have an effect to distort the electric field in that region to a depth of approximately $\sim$ mm [112]. If a photon interacts near this region, the surface channel will either affect the mobility of the electron or hole produced. This effect is illustrated in figure 2.4 where a p-type surface channel affects the collection time of the hole. The decreased mobility of the hole results in an overall detector signal

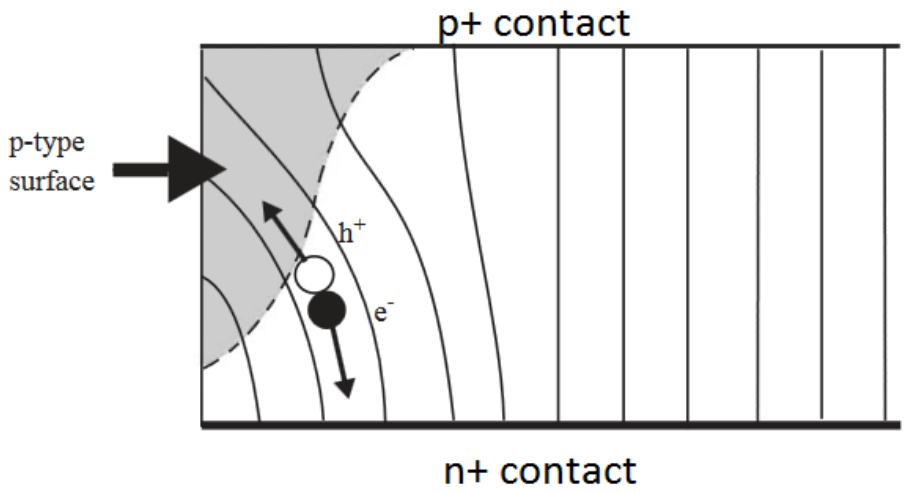

Figure 2.4: An illustration of the surface channel effect. A p-type surface channel (grey area) forms on an n-type HPGe crystal and distorts the electric field in the region. If a photon interacts in the detector near the surface channel, the hole collection time is affected. Figure modified from [110].

that has a modified pulse height. To mitigate some of the surface effects, methods such as ring guard electrodes and grooved surfaces have been developed [84, 99].

2.4 Detector systems

In gamma-ray spectroscopy, the detector system measures the magnitude of the response of the detection medium. The electronic circuit that performs these steps must be tailored to optimize for the minimum detectable signal (count or no count), accuracy of energy measurement, event rate, accuracy of timing measurement, and sensitivity to the pulse shape. The basic sequence of functions for a detector system are shown in figure 2.5. First, the energy deposited by the incident photon produces mobile e-h pairs that are directed to their respective electrodes, inducing a signal current. The number of e-h pairs generated is proportional to the energy deposited by the photon, so integrating the detector's signal current gives the total charge deposited. This signal current is a rectangular pulse that can be as short as ∼ns in width [84, 83]. Integration of the signal current results in a voltage step that is characterized by the transfer

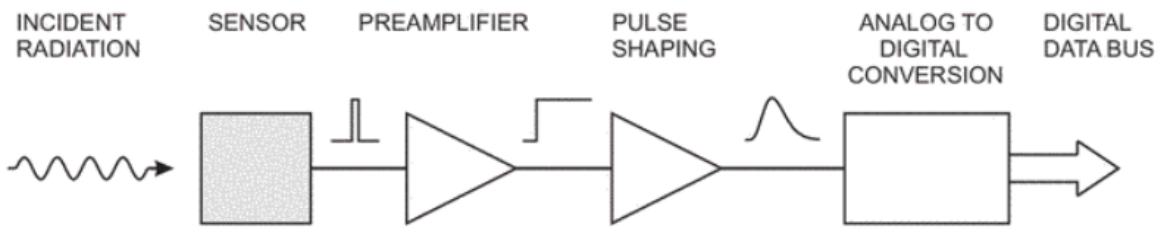

Figure 2.5: The basic flowchart of a detector system. The signal is generated in the sensitive detection volume, amplified and integrated, shaped, and finally converted to a digital signal for storage. Figure reproduced from [83].

function of the preamplifier and has a height that is proportional to the energy of the photon. The step is subsequently processed by a shaping circuit that optimizes the pulse for signal-to-noise ratio for digitization.

2.4.1 Preamplification

For an incident quantum of radiation of energy E_i, the average signal charge produced in the detector volume can be approximated as [83],

$$Q_s = \frac{E_i}{E_{e|h}} e, \tag{2.11}$$

where $E_{e|h}$ is the energy required to create an e-h pair and e is the charge of an electron. In high purity germanium, $E_{e|h} \approx 2.96$ eV and therefore a 1 keV photon will generate approximately 337 e-h pairs for a total charge of $\sim 5 \times 10^{-17}$ C. This is quite small and must be amplified by a charge sensitive amplifier before it can be digitized. A conventional circuit for this is an amplifier with a resistor (R_f) and capacitor (C_f) in parallel providing negative feedback. This integrates the signal current to produce a voltage step that then has an exponential decay with time constant $\tau = R_f C_f$ back to the baseline. The feedback resistor prevents cumulative summing of small DC signals which would saturate the amplifier. However, it is also a significant source of thermally generated Johnson noise [83]. Modern low-noise high-rate preamplifiers

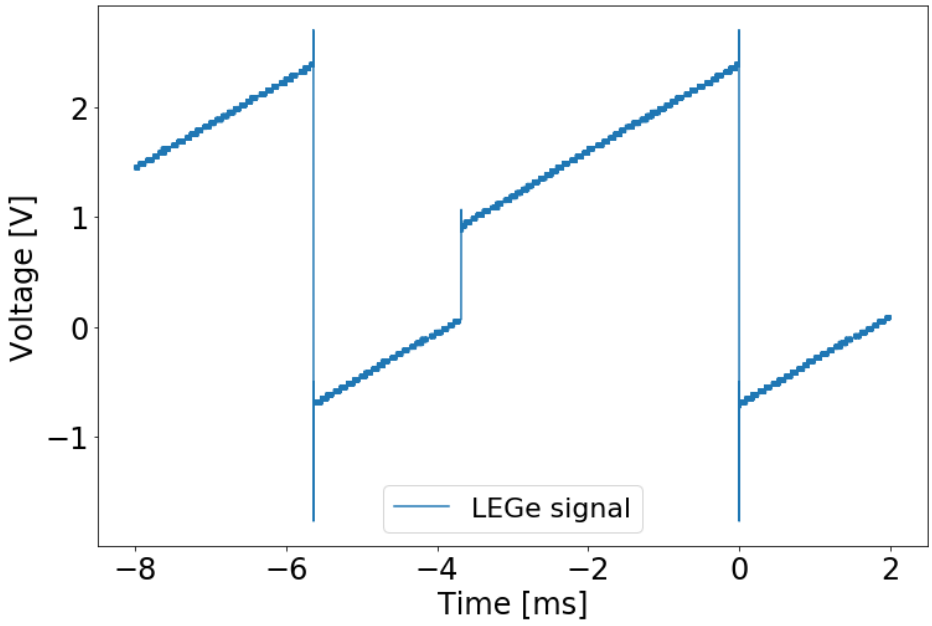

Figure 2.6: An example of the TRP signal from the LEGe detector at TITAN. A large voltage step occurring from an incident photon can be seen near the -4 ms mark.

remove the feedback resistor and simply let the voltage steps accumulate. Once the saturation voltage of the amplifier is reached, a circuit is used to reset the voltage that has accumulated across the capacitor. The two most common methods to actively reset the output are the pulsed optical and the transistor reset circuits [113].

The Canberra LEGe at TITAN employs a transistor reset preamplifier (TRP) and an example of the output is shown in figure 2.6. The output of the preamplifier is a superposition of the time-integrated constant leakage current through the detector and the voltage steps from incident radiation. Once the output is saturated, a circuit with a transistor connected to the input stage of the preamplifier shorts the capacitor. This reset period then constitutes a "dead time" wherein the system is not responsive to incoming radiation. The reset frequency increases with event rate and detector leakage current and the reset time can therefore lead to significant dead times.

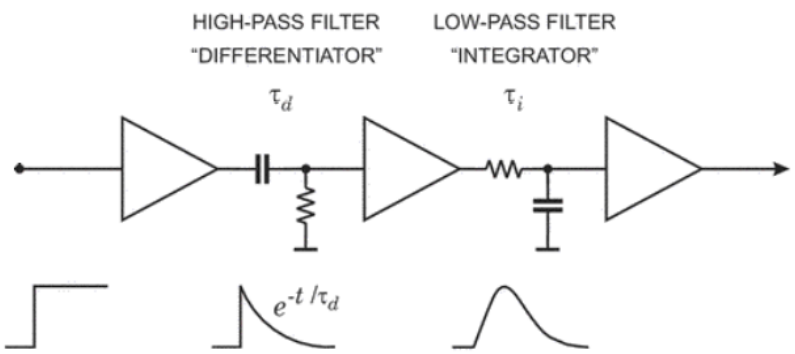

Figure 2.7: Basic components of a shaping circuit. The differentiator circuit sets the decay time (τ_d) of the pulse and the integrator circuit increases the rise time to form the nicely shaped pulse. Figure reproduced from [83].

2.4.2 Shaping and digitization

The voltage step output by the preamplifier is then shaped into a broad pulse with characteristic rise and fall times while preserving the amplitude. For accurate digitization it is desirable that the length of time the shaped pulse spends at full amplitude is maximized. However, in situations where the event rate is high, the tail end of one pulse can interfere with the height of a subsequent pulse. This condition is called pulse *pile-up* or *overflow*. Therefore there is a trade off and proper settings must be chosen for the measurement conditions.

In this work, a new digitizer (MPDD-16 from Mesytec GmbH & Co.) [114] was installed to handle the TRP signal from the LEGe. The shaping electronics for this module use a combination of a high-pass differentiator circuit followed by a low-pass integrator circuit to shape the pulse.

A simple diagram is given in figure 2.7 to illustrate the shaping circuit. Not shown in the illustration is the full differentiation stage of the Mesytec unit, which removes the leakage-induced DC component and contains a circuit for recovering from overflow or underflow to the ADC. The differentiation stage is adjusted by a logic circuit in the digital processing unit after digitization.

In practice, the voltage step output by the preamplifier is not perfect and has a rise time that depends on the charge collection process in the detector. To preserve the amplitude of the voltage step through the shaping circuit, it is optimal that the time constants of the shaping circuit are much larger than the rise time of the voltage step [84]. However, if the rise time becomes too large, the amplitude will suffer and this condition is called *ballistic deficit* [84]. In general, this is not so severe because every pulse will be reduced in amplitude by a constant fraction. But if the fluctuation in charge collection time within a detector is increased, this will lead to a significant loss in resolution. This is a possible mechanism present in our measurements within the external B-field.

The shaped signal is then digitized and various aspects can be stored. In the case of the Mesytec module, the signal is split and send to two separate units for time-to-digital (TDC) and amplitude-to-digital conversion. The TDC is used to provide timestamps for each event and allows for the construction of time dependent pulse height histograms.

2.4.3 The Photopeak Spectrum

During the measurement process the pulse height's are binned and stored and a histogram is constructed. For a mono-energetic signal and an ideal detector, a single bin would be incremented for each event that is processed. Statistical fluctuations within the detector and electronic noise add small fluctuations about the mean pulse height and the effect results in a broadening of the line about the mean bin towards a Gaussian shaped peak.

A number of other processes contribute additional counts to the spectrum and make it difficult to analyze. If an incoming photon interacts with an electron in the medium by the Compton interaction and then exits the medium, counts that are within a broad continuum that lies below the full energy photopeak are produced. The energy of the

scattered photon is given by [84],

$$h\nu' = \frac{h\nu}{1 + \frac{h\nu}{m_0 c^2}\left(1 - \cos(\theta)\right)}, \tag{2.12}$$

where m_0c^2 is the rest-mass energy of the electron and θ is the angle between the incident and scattered photon. The continuum is called the *Compton continuum* and the distance between the high-energy edge and the full photopeak is when θ=180°. If the scattering angle is 0°, it is possible that the photon escapes the medium without depositing any energy.

In practice, full energy photopeaks deviate from a Gaussian shape for a number of reasons. In general, there is a larger contribution of counts to the low energy side of the peak which is termed *low energy exponential tailing* [115, 116, 117]. This arises from incomplete charge collection that is most often due to charge trapping in the detection medium. In addition to the low energy tail, there is also a uniform background contribution to the low energy side of the peak. This arises from photoelectrons from the crystal when photons scatter *into* the detector [118].

Modern methods for photon spectrum analysis use a software to fit the peaks to analytical functions. For gamma-ray spectroscopy with Ge detectors, many fitting functions have been tested and a good summary is given here [119]. In the next chapter we discuss the methods and fitting functions used to study the photopeak spectra obtained with our LEGe.

2.5 The effects of a magnetic field

2.5.1 Within the semiconductor crystal

The motion of charged particles in the presence of electric and magnetic fields is given by the Lorentz force on the particle [120]:

$$\overrightarrow{F} = q(\overrightarrow{E} + \overrightarrow{v} \times \overrightarrow{B}), \tag{2.13}$$

where $\overrightarrow{E}$ is the electric field vector, q is the charge of the particle, $\overrightarrow{v}$ is the instantaneous velocity vector of the particle and $\overrightarrow{B}$ is the magnetic field vector. In the special case that the magnetic field direction is perpendicular to the electric field, the displacement of the charge carriers is sideways from the electric field lines. The charge carriers are deflected at angles θ_e and θ_h with respect to the direction of the electric field and can be approximated by [80, 82]:

$$\tan(\theta_e) = \mu_e^H \overrightarrow{B}, \tag{2.14}$$

and

$$\tan(\theta_h) = \mu_h^H \overrightarrow{B}, \tag{2.15}$$

where μ_e^H and μ_h^H are the Hall mobilities of the charge carriers which are distinct from the regular drift mobilities discussed in earlier sections.

This effect is well known as the Hall effect [82] and is used at low magnetic field strengths in conjunction with resistivity measurements of a semiconductor material to determine impurity concentrations [121]. The Hall effect for semiconductors is illustrated in figure 2.8. In the absence of a magnetic field, the electrons will move downward and the holes will move upward. When the magnetic field is present, both electrons and holes would move towards the left side of the material in turn generating

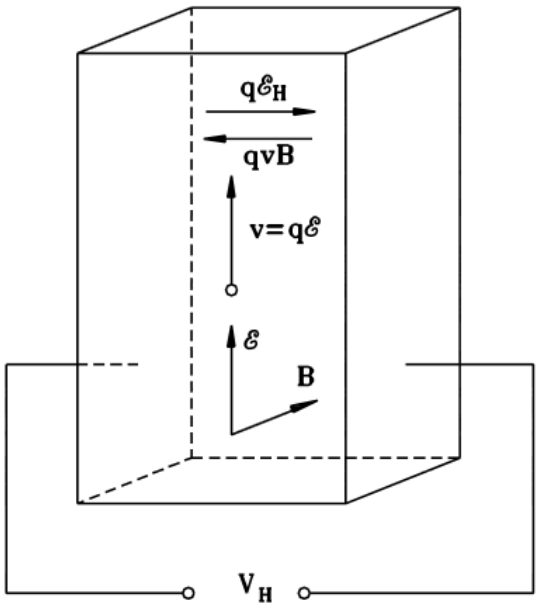

Figure 2.8: An illustration of the Hall effect in a semiconductor. The magnetic field is pointing into the page and the electric field from voltage bias is directed upward. The deflection of the charge carriers results in an induced electric field $\mathcal{E}_H$ and a Hall voltage is measured across the surfaces. Figure reproduced from [82].

an electric field denoted $\overrightarrow{E}_H$. Eventually the force from the naturally built-up electric field will counteract the Lorentz force such that the charge carriers can flow in the same direction as without the magnetic field present. A voltage across the side surfaces called the *Hall voltage* can be measured and depending on the majority carrier of the semiconductor will be positive or negative. The deflection angles of the charge carriers in room temperature silicon have been measured with a 1 T magnetic field to be θ_e=9.5° and θ_h=2.1° [82]. This corresponds to Hall mobilities of 1670 cm^2/(V·s) and 370 cm^2/(V·s) for electrons and holes, respectively.

In principle, it is possible that the deflection of the charge carriers in the magnetic field increases the probability of trapping and recombination events. This would lead to a reduced signal amplitude that would skew the photopeak distributions towards the low-energy side of the spectrum. In addition, it's possible that the magnetic field causes charge carriers to be deflected towards the surfaces of the detector where they could be affected by the surface channel effects described in section 2.3.4.

2.5.2 Outside of the semiconductor crystal

In addition to the effects described in the previous section, there is a particular case of a chemi-ionization process called Penning ionization (PI) [122] that could affect semiconductor detector performance. The PI mechanism is commonly represented as the reaction

$$A^{\star} + B \longrightarrow A + B^{+1} + e^{-}, \tag{2.16}$$

where * denotes an electronic excitation of some species A. Species A is either an atom or a molecule and the species B can vary in complexity from an atom to a molecule adsorbed onto a surface. In order for the reaction to occur, species B must have an ionization potential that is lower than the excited state of species A. B^{+1} is then the residual ion left after the electron becomes free.

It has been suggested by Sanchez Lorente *et al.* [77] and Agnello *et al.* [78] that the effect of the magnetic field could be to increase the effective ionization rate in the residual gas in the detectors vacuum capsule. In principle this occurs when an electron is created in the vacuum capsule and accelerated towards the detector contacts by the electric potential. The presence of the magnetic field will not change the mean free path between collisions that could potentially cause ionizations, but it would deflect the particle and lead to a longer overall travel time. The increased travel time could cause secondary ionizations that might eventually lead to a discharge onto one of the detector contacts.

Chapter 3

Experimental data and analysis methods

In this work there are three main methods that were performed towards the improvement of the spectroscopy system at TITAN-EBIT. These methods each used a different device to record data from the LEGe. These devices are an EG&G Ortec Digital Gamma-Ray Spectrometer (DSPEC) [123], a Mesytec MDPP-16 16-bit time and amplitude digitizer [114], and a Lecroy Wavesurfer 3054 high bandwidth oscilloscope [124].

First, the gathering of the data with the DSPEC was performed during the thesis work of T. Brunner [54] and in this work it is analyzed using simple channel integration and peak fitting. The purpose of this analysis is to elucidate the change in photopeak resolution and detection efficiency as a function of magnetic field. Second, the Mesytec MDPP-16 digitizer was installed into the EBIT spectroscopy setup and first used in an on-line experiment with the LEGe. The MDPP-16 digitizer is a fast, high resolution module for recording peak time and amplitude data and is specifically meant to handle the TRP signal from the LEGe. This digitizer was first used with TITAN on-line for the experiment S1478 [65], which is discussed in more detail in the next section. Third, the Wavesurfer 3054 was used to trigger on and record the voltage steps produced by

^{133}Ba			^{137}Cs		
	energy [keV]	intensity [%]		energy [keV]	intensity [%]
$K_{\alpha 2}$	30.625	33.9 % *10*	$K_{\alpha 2}$	31.817	1.99 % *5*
$K_{\alpha 1}$	30.973	62.2 % *18*	$K_{\alpha 1}$	32.194	3.64 % *10*
	79.6142	2.65 % *5*		661.657	85.10 % *20*
	80.9979	32.9 % *3*			
	276.3989	7.16 % *5*			
	302.8508	18.34 % *13*			
	356.0129	62.05 %			
	383.8485	8.94 % *6*			

Table 3.1: A table of important x- and gamma-ray lines from ^{133}Ba and ^{137}Cs. Data tabulated from the National Nuclear Data Center at Brookhaven National Laboratory [62].

the LEGe preamplifier. The purpose of recording this data is to observe the detector's leakage current and the characteristics of the voltage steps as a function of the magnetic field.

It is important to note that from here on all reported values of the magnetic field are the value at the EBIT trap center. Therefore the actual value of the magnetic field across the Ge crystal depends upon the positioning of the retractable cryostat during the measurement. Furthermore, the solid angle and therefore the count rate is also affected by this positioning. For the three different data acquisition methods described here, the cryostat position is different and will be noted in each section.

3.1 Sources

For all of the methods described in this chapter, the radioactive calibration sources ^{133}Ba and/or ^{137}Cs are used with the LEGe detector. Some of the relevant gamma- and x-ray radiation lines for these sources are produced in Table 3.1. Presently there is no method for positioning radioactive calibration sources into the EBIT trap center other than receiving RIB from ISAC. Instead, radioactive sources are mounted onto a cap that can be placed onto one of the detector ports surrounding the trap center. The

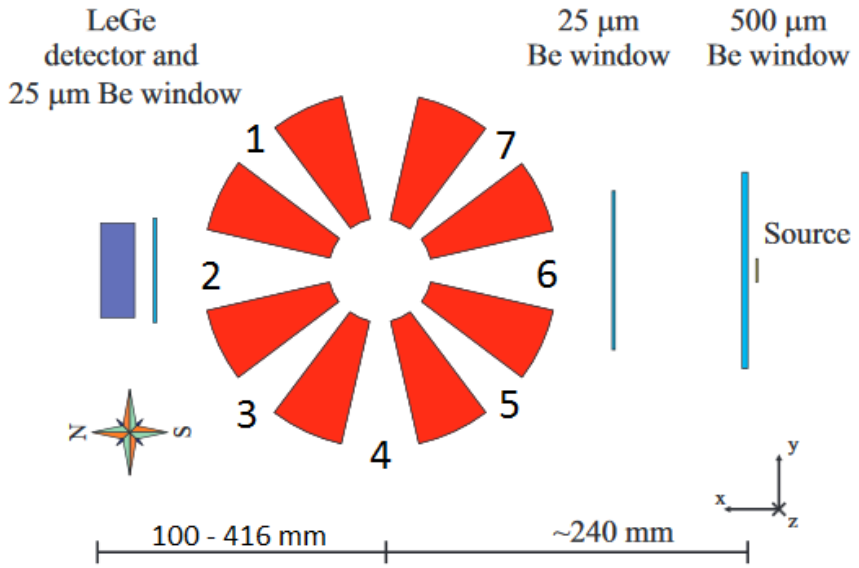

Figure 3.1: A schematic showing the fixed position of the calibration sources and the variable position of the detector. Figure reproduced from [54].

	^{133}Ba	^{137}Cs
Half life	10.551 ±0.11 years	30.17 ±0.16 years
Activity	20.2 kBq	343.5 kBq
Date measured	9 May 2017	15 Sept, 2008
TRIUMF inventory number	R-00794	R-000854

Table 3.2: Inventory numbers and activity of the radioactive calibration source. Both sources are produced by Isotope Products Laboratories.

LEGe on the retractable cryostat is mounted on port 2 on the north side of the EBIT trap and the sources are placed on port 6 on the south side so that they directly face the LEGe. This setup is illustrated in figure 3.1 which also shows the three Be windows between the source and detector. In this setup, the smallest possible distance between the detector and sources is approximately 340 mm when the detector is fully extended towards the trap center. Because of this distancing between the source and detector crystal, the strongest sources available were used to decrease the total measurement time required. Table 3.2 gives the TRIUMF inventory number and activity of both sources that were used. Despite providing only one usable line at 660 keV, the ^{137}Cs source was chosen because it was the highest activity source available at TRIUMF at

the time.

During measurements, it was found that the event rate registered by the detector is very sensitive to the centering of the sources on the mounting cap. This is due to the small angles of the drift tube slits that can block some of the radiation if the source is mounted off-axis. To maintain maximum exposure of the sources to the detector crystal, the two sources were mounted in a stacked orientation. To minimize attenuation of the low-energy peaks from the ^{133}Ba source, the ^{137}Cs source is placed behind. Despite choosing the strongest sources available, we observed a count rate between 1 and 10 events/second which placed certain constraints on our measurements. The consequence of this low count rate is that measurement periods had to be quite long to gain enough statistics.

The TITAN facility does have an off-line ion source for beam tuning to prepare for a measurement, but this only provides stable ion beams. Therefore, aside from an on-line experiment with ISAC beam, the only way to calibrate the detectors in TITAN-EBIT is with the method described above.

3.2 Analysis of DSPEC data

A dataset of photon spectra was recorded during calibration for the ^{124,126}Cs experiment outlined in section 1.3.1. At the time, the LEGe was paired with two digitizers (EG&G Ortec Digital Gamma-Ray Spectrometer (DSPEC) model [123]) to record x-ray and gamma-ray spectra [54]. During the measurements, one DSPEC was used to record spectra during ion storage and the other was used to record background spectra while the trap was empty. For benchmarking the DSPEC, calibration data was recorded with a ^{133}Ba source and is available for different settings of the EBIT magnetic field ranging from 0 to 5.5 T. During all of these measurements, the LEGe was at full extension towards the trap center and therefore approximately 340 mm from the ^{133}Ba source

and 100 mm from the trap center. For each value of the magnetic field, three sequential datasets, each with a measurement time of 1 hr, were made. There was an additional measurement performed at 5.5 T, but only a single 1 hr dataset is available.

All peak distribution and background fitting was performed with the *lmfit* module [125], which is a non-linear least squares minimization and curve-fitting module for Python 3.6. In section 2.4.3 we discussed the characteristics of the photopeak spectrum. The general components for a peak fitting function are the symmetric full-energy contribution, the low-energy background, and the low-energy tail to account for incomplete charge collection. In this analysis, three different fitting functions are used; they are given below.

Model 1 is a fitting function that is simply composed of a Gaussian distribution to model the symmetric full-energy peak. The well-known Gaussian distribution is given as:

$$f(x; A, \mu, \sigma) = \frac{A}{\sigma\sqrt{2\pi}} e^{-(x-\mu)^2/2\sigma^2}, \tag{3.1}$$

where x is the channel, A is the amplitude, σ is the standard deviation, and μ is the centroid.

To include the characteristics of peak asymmetry discussed in section 2.4.3, Model 2 is a piecewise function called a bi-Gaussian that is composed of two the halves of Gaussian functions. This function has been extensively reported on in [126] and [119]. In addition, the study by Agnello *et. al.* [78] involving coaxial HPGe operating in a strong B-field used this function in fitting the 1173 keV and 60 keV peaks from ^{60}Co and ^{241}Am, respectively. The bi-Gaussian distribution is given as:

$$f(x; A_1, A_2, \sigma_1, \sigma_2, \mu) = \begin{cases} \frac{A_1}{\sigma_1\sqrt{2\pi}} \times e^{-(x-\mu)^2/2\sigma_1^2} & x \leq \mu \\ \frac{A_2}{\sigma_2\sqrt{2\pi}} \times e^{-(x-\mu)^2/2\sigma_2^2} & x > \mu \end{cases}, \tag{3.2}$$

where the parameters are the same as for the Gaussian distribution and the subscripts

$_1$ and $_2$ indicate parameters on the left or right of μ, respectively.

Model 3 is a composite function that includes the symmetric Gaussian given in equation 3.1 and an asymmetric Gaussian that skews the peak towards the low-energy side. The asymmetric Gaussian can be realized in a number of ways [119] but is most commonly built using a convolution of an exponential tail with a Gaussian distribution or as a skewed Gaussian distribution. In this work we tested both the skewed Gaussian distribution and the exponentially tailed Gaussian. The skewed Gaussian distribution is given as:

$$f(x; A, \mu, \sigma, \gamma) = \frac{A}{\sigma\sqrt{2\pi}} e^{-(x-\mu)^2/2\sigma^2} \left[1 + \mathrm{erf}\left(\frac{\gamma(x-\mu)}{\sigma\sqrt{2}}\right)\right], \tag{3.3}$$

where erf is the error function and γ represents the parameter to control the skewness of the distribution. If γ is negative, the distribution is skewed towards the left. The form of the exponentially tailed Gaussian that we used is borrowed from the RadWare software package for gamma-ray analysis [118] and given as:

$$f(x; A, \mu, \sigma, \beta) = \frac{A}{\sigma\sqrt{2\pi}} \ \mathrm{erfc}\left(\frac{x-\mu}{\sigma\sqrt{2}} + \frac{\sigma}{\beta\sqrt{2}}\right) e^{(x-\mu)/\beta}, \tag{3.4}$$

where erfc is the complementary error function and β controls the skewness of the peak. If β is positive, the distribution becomes left-skewed.

For all peaks, the background components were estimated as a composition of a linear function and a step function. There are many ways to generate a step-like background contribution function (see [119] for a list) and we chose to use the complementary error function. The step background is given as:

$$f(x; H, \mu, \sigma) = \frac{H}{2} \,\mathrm{erfc}\left(\frac{x-\mu}{\sqrt{2}\sigma}\right). \tag{3.5}$$

3.3 Mesytec digitizer and commissioning experiment

The DSPEC modules mentioned above do not provide timestamped event data which is a necessary component of analyzing the time-dependent photon spectra for experiments at TITAN-EBIT. As such, a new fast and high-resolution pulse amplitude and time digitizer has been purchased from Mesytec GmbH & Co. KG. The Mesytec MDPP-16 [114] is a 16-bit digitizer that contains specific software for accepting the TRP signal from the LEGe. Internally, it is composed of a low noise amplifier, a variable differentiation stage, a shaping filter and 80 MHz sampling ADCs. After digitization, the digitized data are then analyzed by a TRP-specific software module stored on a field programmable gate array (FPGA). This FPGA digital processing unit first reconstructs the original staircase-like signal and then performs digital pulse processing with 180 signal processors to accurately resolve time and amplitude values of the events. Amplitude resolution is better than 32 k and timing is available down to 60 ps rms.

The Mesytec digitizer was installed into the EBIT spectroscopy system and setup to be synchronized in time with EBIT injection and extraction signals. To achieve this, the TITAN system uses a programmable pulse generator (PPG) which uses standard NIM signals to synchronize other devices in the system. With the MDPP-16 installed, calibration data was taken with both ^{133}Ba and ^{137}Cs sources in the arrangement detailed in section 3.1. Data acquisition parameters such as coarse gain, fine gain, shaping time, timing filter integration and differentiation time, and reset time were adjusted to obtain the best photopeak FWHM values.

Once the running parameters were optimized, the MDPP-16 was commissioned in the TITAN experiment S1478 [65]. S1478 is a proof-of-principle experimental proposal to study changes in the decay rate of the isotopes ^{64}Cu and ^{48}Cr in stellar-like conditions (i.e. highly charged) in the TITAN-EBIT. A decay by the electron capture of bound-state electrons is significantly influenced by the density of K-shell electrons around the nucleus [127]. In principle, the complete removal of all bound electrons will render an

isotope stable unless electrons are captured by the continuum or another decay mode is possible. Because the high plasma temperatures in stars are sufficient for ionization of various isotopes, this is important information to study reaction paths in stars such as the slow neutron capture process (s-process) [52].

Studies of the modified decay rate of highly charged isotopes have already been performed in the storage ring at GSI Darmstadt for H-like (one bound electron) and He-like (two bound electrons) $^{140}Pr^{58+,57+}$ [128], $^{142}Pm^{60+,59+}$ [129], and $^{122}I^{52+,51+}$ [130]. In principle, experiment S1478 is performed at TITAN-EBIT by charge breeding the isotopes that contain an EC-decay branch into bare, H-like or He-like ionization states. Once in these states, the modified decay rate (compared to terrestrial) is then measured by observing the change in population of the parent and daughter states of the EC decay mode.

3.4 Voltage step waveform capturing

To study how the magnetic field affects the signal current output by the detector, a high bandwidth oscilloscope (Lecroy Wavesurfer 3054 [124]) was used to trigger on and record the voltage steps output from the LEGe preamplifier. To explain how this was achieved, consider the example LEGe signal shown in figure 3.2. We will call the useful region of the detector signal occurring between reset periods the *live interval*. A simple way to capture the live intervals during measurement time is to trigger on one of the reset periods and record data after the trigger for a predetermined span of time. However, due to the low count rate explained in section 3.1, approximately 1 in every 100 of the captured live intervals would contain a voltage step from ionizing radiation. It is therefore very impractical to record every live interval because this would place a large burden on the post-measurement processing work to parse through and pick out voltage steps

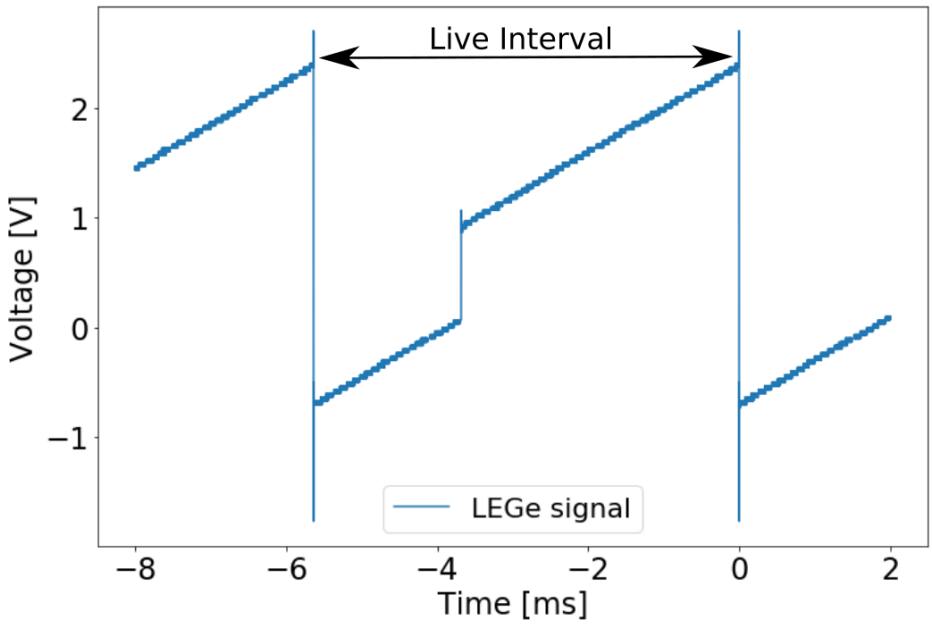

Figure 3.2: An example signal from the LEGe detector recorded on the Lecroy Wavesurfer oscilloscope. A large voltage step due to an incident photon is observed near the -4 ms mark between the two reset periods. A black arrow is used to indicate the portion of the signal that is the live interval.

In the absence of ionizing radiation, the time span of the live interval is only a function of the constant leakage current through the detector and as such has a constant slope. In the presence of ionizing radiation, the width of the live interval is shorter because the reset periods must occur at a higher frequency. As such, a trigger that only fires when two reset periods occur within a given time threshold will filter out the live intervals that do not contain voltage steps.

To determine the threshold time, we recorded approximately 800 live intervals in the absence of ionizing radiation and determined the average width of the live interval. We then manually toggled the trigger threshold and determined what fraction of the recorded intervals contained steps. Once we reached a reasonable fraction of the recorded intervals containing steps, we began to record data sets for further analysis. The possibility that the chosen threshold time cuts out a portion of the bottom end of the histogram of voltage steps is not lost on us. This is addressed in the results section.

Waveform capturing was performed at two different timing resolutions and with both sources ^{133}Ba and ^{137}Cs mounted onto the cap. At a lower time resolution, approximately 50,000 waveforms were captured. This data was captured at a low resolution to use as a proof-of-principle that we could use it to estimate voltage step heights and build a histogram. The higher time resolution data was recorded with the EBIT magnet at both 0 T and 4 T. This data was gathered to discover if we could see any characteristic differences in voltage steps between 0 T and 4 T. At 0 T, approximately 5000 waveforms were captured and at 4 T approximately 2000 waveforms were captured.

To process these waveforms, a program in Python 3.6 was written to identify the steps within the live interval, estimate the step height, and build the histogram. To estimate the step height, we first identify the position of all voltage steps within the live interval. Next, we perform a linear fit of both portions of the leakage current to the left and right of the identified step. Finally, we perform an interpolation between the two lines at the point of the step to determine the height of the step. It should be noted that the voltage resolution of the Wavesurfer 3054 is limited to only 8-bits (256 channels) and this severely limits the resolution of the histograms that were constructed. The consequences of this are discussed more in the next chapter.

Chapter 4

Results and Discussion

4.1 Positioning

Before we give the results, it is important to reiterate that the reported magnetic field values are at the center of the trap. During the DSPEC data collection, the detector was positioned at approximately 100 mm from the trap center. During the data collection with the MDPP-16 and the Wavesurfer, the detector was positioned at approximately 260 mm from the trap center. Figure 4.1 shows a plot of the simulated transverse magnetic field at the center of the EBIT. The approximate position of the LEGe for each of the three data acquisition methods is shown. During acquisition with the DSPEC, the magnetic field at the crystal was approximately 15% of the value at the trap center. During acquision with the MDPP-16 and the Wavesurfer, the value was much lower at approximately 5% of the value at the trap center.

4.2 Analysis of DSPEC data

To begin the analysis of the histograms recorded with the DSPEC as a function of magnetic field, we first take a qualitative look at some regions in the photon spectra. Here we define four regions in order of increasing photopeak energy from the ^{133}Ba

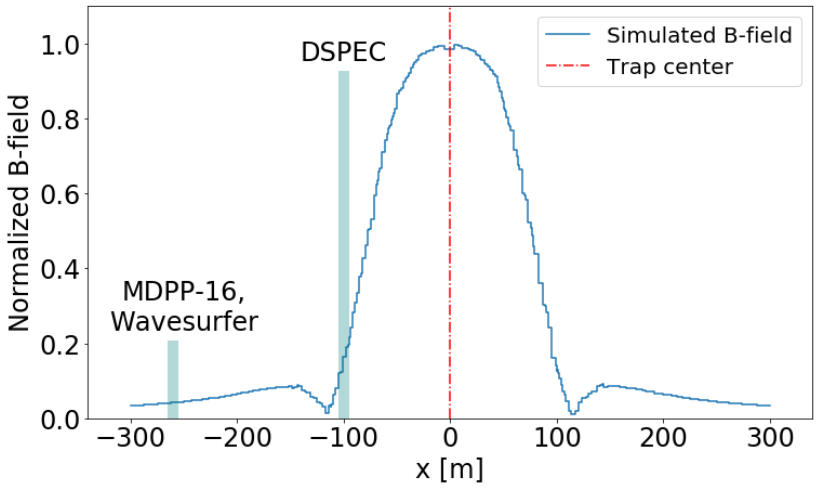

Figure 4.1: A plot of the simulated transverse magnetic field at the center of the EBIT. The approximate positions of the detector for each of the data acquisition methods is shown. Simulation performed with COMSOL Multiphysics® [56].

source. Region 1 contains the two photopeaks at 30.6 and 30.9 keV, Region 2 contains the two photopeaks at 80 and 81 keV, Region 3 contains the 302 keV photopeak, and Region 4 contains the 356 keV photopeak.

Figure 4.2 shows the effects that the magnetic field has on these four regions. Notice that the y-axis of the plot is split between the left side of the figure which shows the photon peaks below 100 keV and the right side which shows the photon peaks above 300 keV. We can make some initial observations about the peak characteristics in response to the magnetic field.

Region 1 In this region are the 30.6 and 30.9 keV peaks which partially overlap to give a single skewed distribution. Between 0 and 3.5 T it is difficult to notice a change in the distributions. When the magnetic field reaches 4.5 T, the distribution is significantly shifted and skewed towards a lower energy. At 5.5 T, the distribution is all but completely diminished. Near channel 440 there is a small bump that looks to be superimposed onto a step.

Region 2 In this region are the 80 and 81 keV peaks. Between 0 and 3.5 T the peaks

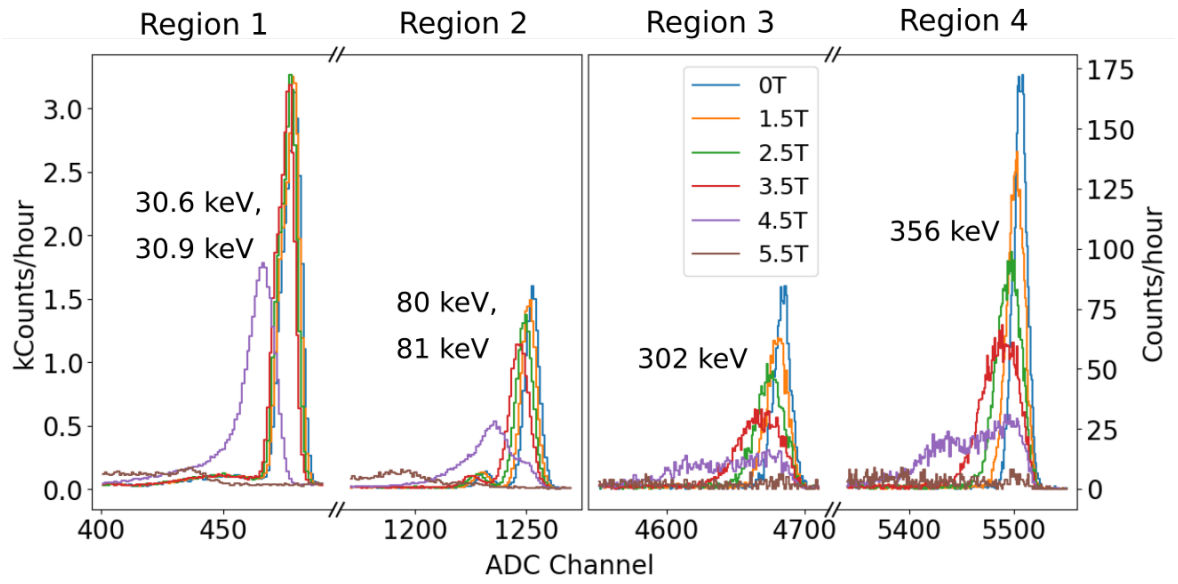

Figure 4.2: A plot showing four different regions of the photon spectrum as a function of the magnetic field at the trap center.

are well separated. As the magnetic field increases we can clearly see the 81 keV peak shift left and decline in height. At 4.5 T, we can no longer discern the two peaks and the distribution is very unrecognizable. At 5.5 T, we see a similar distribution as region 1. The peak is strongly diminished and shifted and it looks to be superimposed onto a step just below channel 1200.

Region 3 This region contains only the 302 keV peak alone. Between 0 and 3.5 T we see similar effects as regions 1 and 2. The peak is low-energy skewed, shifted and decreases in height. At 4.5 T the distribution takes a significantly broadened form and no longer looks like it has a peak. At 5.5 T the distribution is nearly gone, save for some low-energy counts.

Region 4 This region contains only the 356 keV peak. Between 0 and 3.5 T, we see a similar pattern to region 3. At 4.5 T the distribution is again significantly broadened and it looks like two peaks. At 5.5 T, the distribution is again nearly gone.

To conclude, the general effects that we see are a skewing and shifting of the peaks, both in the direction of lower energy. In region 1, we see that these effects are quite small in comparison to the higher energy regions. If we propose that the magnetic field causes us to lose a fraction of liberated e–h pairs, then this is an expected result and a quantitative study should instead look at the *relative* shifting and skewing of the peaks. Common among all four regions is that a significant peak degradation occurs when the magnetic field reaches 4.5 T. If we compare this between regions, it is also apparent that this effect is worse for higher energy regions.

Since the range of photons in Ge varies significantly from 30 keV to 356 keV, these results are expected. If a photon is deposited near the collection contacts, the magnetic field will have less of an effect on the charge collection process. The attenuation of a photon beam can be described by an exponential law as [84],

$$N = N_0 \exp(-\frac{\mu}{\rho}\rho t), \tag{4.1}$$

where N/N_0 is the fraction of incident photons that are attenuated in a monoenergetic beam per unit thickness t of a material with density ρ. The quantity μ/ρ is termed the mass attenuation coefficient. In figure 4.3, we have taken values of the Ge mass attenuation coefficient tabulated by the National Institute of Standards and Technology [131] as a function of photon energy. The plot shows the fraction of incident photons that are attenuated as a function of penetration depth into the Ge crystal. As we can see, 1 keV and 10 keV photons are quickly attenuated at the surface and higher energy photons such as 100 keV and 300 keV penetrate more into the crystal bulk. As such, low energy photons will be quickly collected and the magnetic field will have less of an effect to disrupt the charge collection process.

Returning to figure 4.2, in the range of 0 to 3.5 T we observe peak broadening and a decreasing height, but it looks as if the integral of these distributions is conserved.

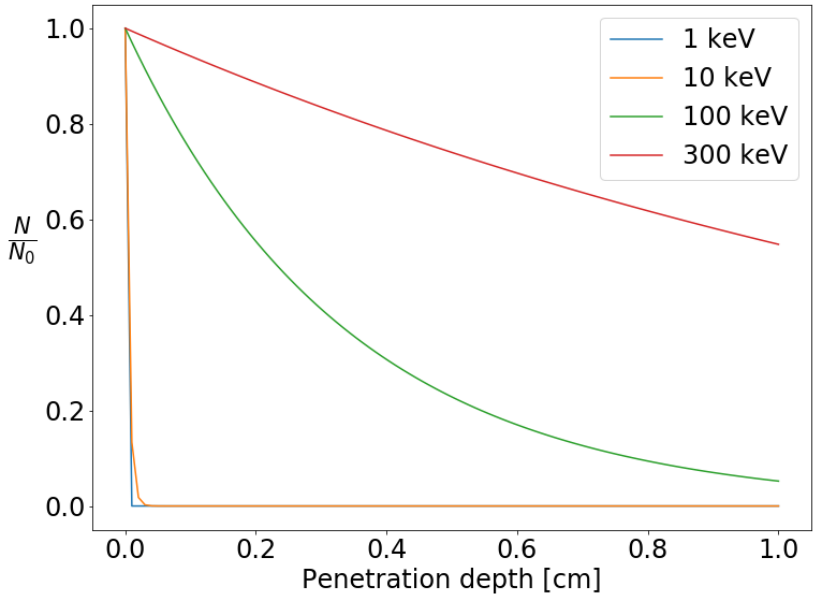

Figure 4.3: N/N_0 is the fraction of incident photons that are attenuated by the Ge material. Here it is plotted as a function of penetration depth into Ge material. This is representative of our crystal which has 1 cm thickness. Mass attenuation coefficient values obtained from NIST [131].

This would indicate that the magnetic field has affected the charge collection process, but we are not losing counting efficiency. To study these effects in more detail, we turn to quantitative methods and perform a simple analysis by channel integration.

4.2.1 Channel integration

A simple analysis is to pick channels that contain the peaks of interest and to plot the total number of counts as a function of the magnetic field. To account for the significant broadening and shifting of the distributions as the magnetic field increases, we choose a large span of channels. The channel spans for the four regions are as follows: Region 1 is channels 190–490, Region 2 is channels 1050–1270, Region 3 is channels 4380–4750, and Region 4 is channels 5100–5550. For each region we define the fractional count rate as:

$$\Delta\varepsilon = \frac{N_{B_i}}{N_{B=0}}, \tag{4.2}$$

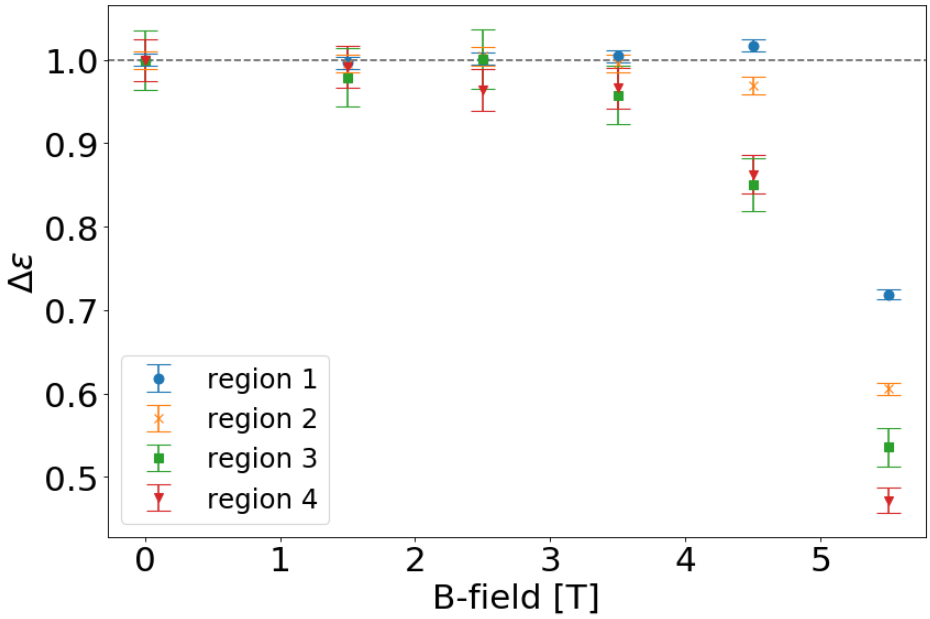

Figure 4.4: A plot of the fractional count rate in the four regions we have defined as a function of the magnetic field at the trap center. From this it is clear that the drop in count rate is more severe for the higher energy peaks (regions 3 and 4). Error bars are one standard deviation.

where $N_{B=0}$ is the total counts without a magnetic field and N_{B_i} is the total counts at a non-zero value of the magnetic field. Figure 4.4 shows the fractional count rate within the four defined regions as a function of the magnetic field. Within the bounds of the regions chosen, this plot shows a clear decrease in the number of counts registered by the DSPEC as the magnetic field increases past 3.5 T. From this plot it is also clear that the drop in count rate is more severe for the high energy photon events (regions 3 and 4). These results are in agreement with the qualitative observations made in the preceding section.

It is surprising that the drop in fractional count rate is more severe for higher energy events. To check that this observation is not depending strongly on the channel ranges we have chosen, we can expand and contract the sizes of the regions. Table 4.1 shows the channel ranges of the expanded and contracted regions in comparison to the originals. Figures B.1 and B.2 in Appendix B plot the fractional count rate in the

Region	Original	Contracted	Expanded
1	190 – 490	250 – 490	150 – 500
2	1050 – 1270	1090 – 1270	1010 – 1310
3	4380 – 4750	4420 – 4710	4340 – 4790
4	5100 – 5500	5140 – 5490	5060 – 5540

Table 4.1: A table of the channel ranges for each region.

newly defined regions as a function of B-field. These plots essentially show the same result: that the peak distributions start to severely deteriorate past 3.5 T and that this effect is much worse for higher energy peaks. The drawback of using this simple channel integration method is that we cannot account for how counts are lost or gained within the specific region.

A loss can occur when a count that would normally be digitized into one channel is instead digitized into a lower channel and exits the lower bounds of the region. In this case, the amplitude of the digitized signal is no longer representative of the total energy deposited by the photon. If the severity of the effect is strong, the count could be completely missed by the digitizer and no longer show up anywhere on the histogram. A gain can occur when a higher energy count loses some amplitude and is shifted down into the region.

To consider this further, we observe the count rate of the entire spectrum recorded by the DSPEC. This includes full-peak counts from the calibration source and any ambient background counts. A close look at our spectrum in figure 4.5 shows an increased count rate at the bottom end of the spectrum. These counts are due to false triggering when the noise level is above a threshold set by a constant fraction discriminator (CFD) in the digitizer. Therefore we see that the magnetic field increases noise and more of this is falsely triggered on by the digitizer. Figure 4.5 (**left**) shows the count rate in the threshold region as a function of the magnetic field. Figure 4.5 (**right**) shows the sum count rate in the threshold region as a function of the magnetic field.

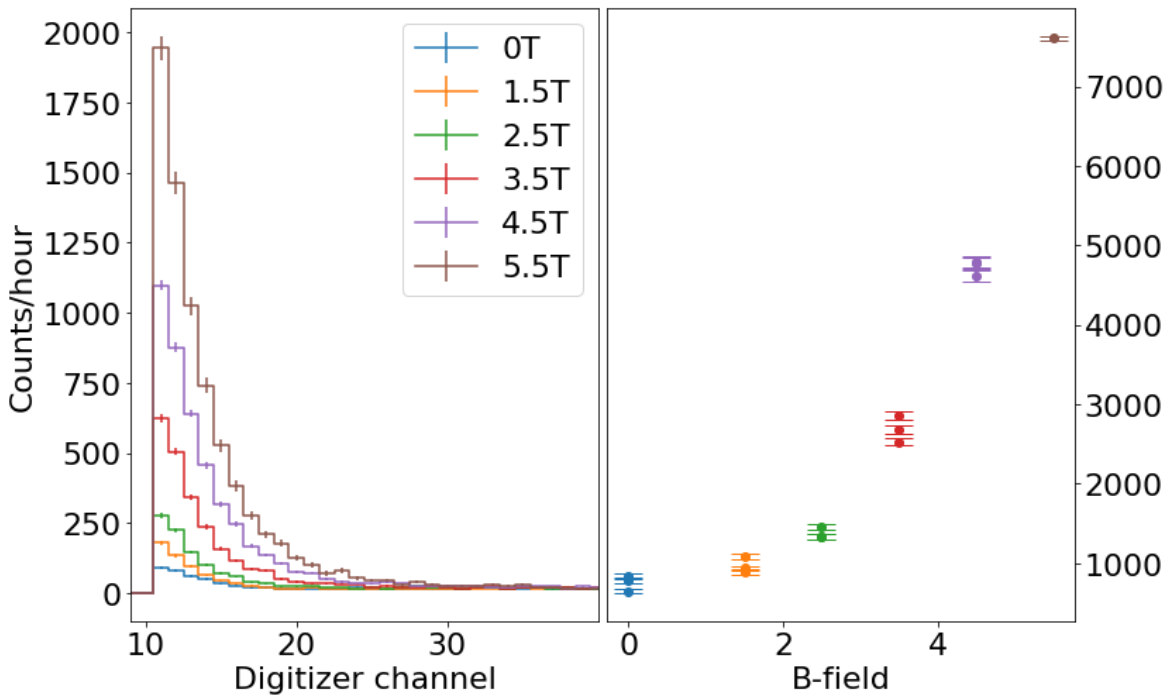

Figure 4.5: (**Left**) count rate in the threshold region as a function of the magnetic field at the trap center. (**Right**) the total count rate between channels 1 – 40 as a function of the magnetic field at the trap center. Error bars are given as one standard deviation assuming Poisson statistics in each channel.

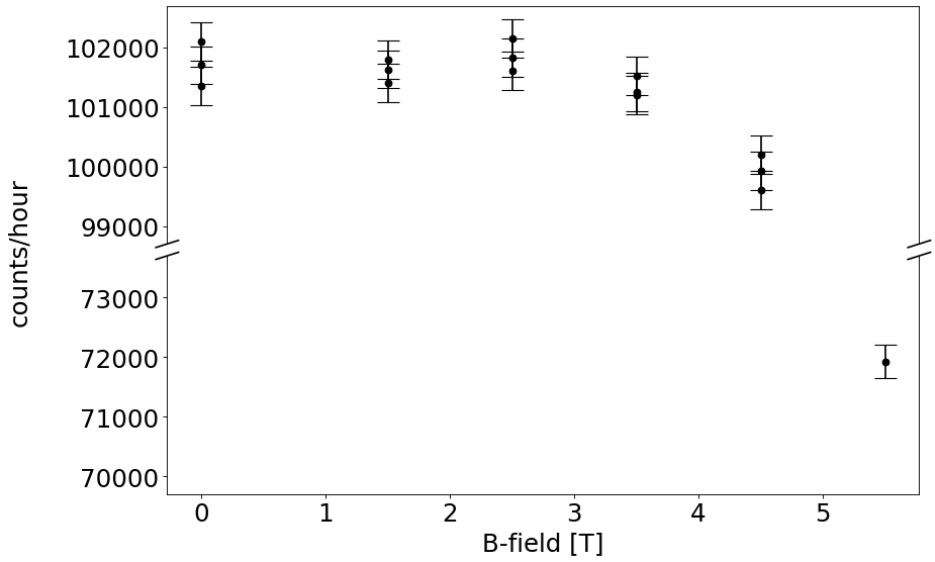

Figure 4.6: A plot of the total count rate of the spectrum with the low energy threshold region removed and as a function of the magnetic field at the trap center. Error bars are one standard deviation.

In figure 4.6 we have removed the counts from the threshold region and plotted the total counts/hour as a function of the magnetic field. This plot clearly follows the same downward trend seen in figures 4.4, B.1 and B.2. This shows that the overall measurement efficiency in counts/hour decreases as the magnetic field is increased. Between 0 and 3.5 T, there does not appear to be a difference outside of statistical uncertainty. However, at 4.5 and 5.5 T, the drop is very noticeable and well outside of statistical uncertainty.

One explanation for counts being lost is that the actual live time of the measurement system becomes a smaller fraction of the total measurement time due to an increased dead time. As discussed in section 2.5.2, it is possible that the magnetic field increases the leakage current through the detector leading to an increased reset frequency and therefore a larger fraction of system dead time. However, to account for the loss in counts observed, a very large percentage of the total measurement time would have to be dead time. For each measurement interval, the DSPEC produces the variables *real_time* and *live_time* which can be used to calculate the dead time. In analyzing this data, we did not see a significant increase in dead time with B-field that could account for such drops in count rate. In fact, the change in dead time that we calculated is so small that it would not change the counts/hour outside of any statistical uncertainty.

4.2.2 Peak and background fitting with *lmfit*

In this fitting analysis, the ^{133}Ba peaks at 80, 81, 302, and 356 keV are considered because they have sufficient statistics. The first step in the fitting analysis is to use the 0 T data to study which distribution models are best suited for the photo-peaks. The results in section 4.2.1 show good measurement stability between the three hour-long datasets for each value of the B-field. As such, we have combined all three hour-long datasets to perform the peak fitting. For the peaks above 300 keV, we used a background function that consisted of only a step function to approximate the low-

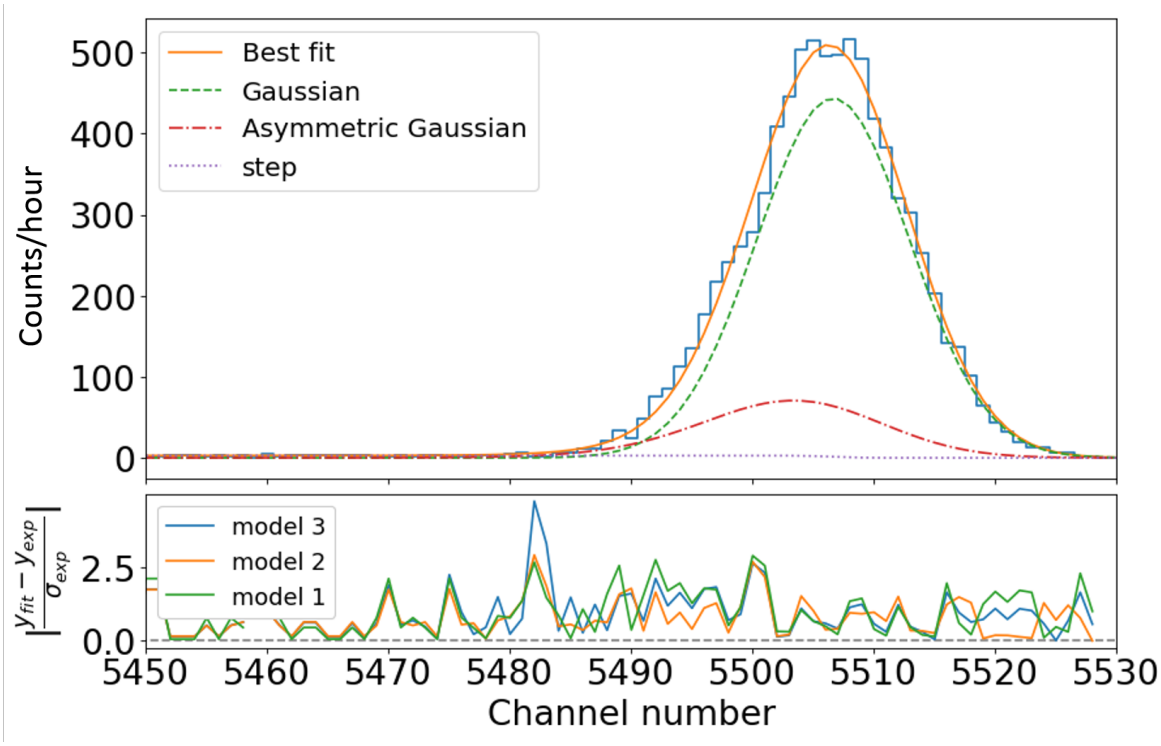

Figure 4.7: (Top) A plot of the 356 keV peak fitted with Model 3 with B=0. The symmetric Gaussian and the skewed Gaussian components are shown as well as the step-approximated background. (Bottom) the absolute value of the normalized residuals resulting from fitting with the three different models.

energy background. This is appropriate because the Compton continuum from the 356 keV peak does not show up until far below 300 keV. For the lower energy peaks we used a background function consisting of a step function and a linear function. To demonstrate the fitting results, figure 4.7 (top) shows the 356 keV peak fitted with Model 3 and showing its components. Recall that Model 1 is the symmetric Gaussian, Model 2 is the bi-Gaussian and Model 3 is composed of a Gaussian and an asymmetric Gaussian. Figure 4.7 (bottom) compares the normed residuals of the three models that were tested.

In the main part of the peak between channels 5500 and ∼5515, all three models have a similar performance. On the high energy side of the peak in the region of channel 5520, Models 2 and 3 perform better than Model 1. In using Model 3 to fit the

distributions, we found that it is easier to use the equation from Radware (eq. 3.4) rather than the skewed Gaussian (eq. 3.3) to model the asymmetric Gaussian component. This is due to the parameterization being easier to constrain when performing the least-squares fitting.

However, as has been noted by D. Radford [118], there is a significant cross-correlation between the heights of the Gaussian and asymmetric Gaussian components. If both the relative height of the asymmetric Gaussian and the parameter β from equation 3.4 are unknown, this leads to significant uncertainty in fitting. Through experience with peak fitting and systematic studies, they have shown that there are a few parameters of the fit that stay constant or are linear as a function of channel. The parameter R is the ratio of the height of the skewed Gaussian to the height of the total peak. The parameter *STEP* is the ratio of the height of the step to the height of the total peak. The parameter β is the same as that given in equation 3.4 for the skewed Gaussian. D. Radford has noted that the parameters *STEP* and *BETA* remain constant as a function of digitizer channel. The parameter R can usually be approximated as a linear function of digitizer channel.

In an attempt to mitigate our own fitting uncertainty with Model 3, we strongly constrained the parameters of the step function and the asymmetric Gaussian as functions of parameters of the symmetric Gaussian component. These constraints are all derived from the 356 keV peak at 0 T. Letting the parameters for amplitude and β of the asymmetric Gaussian vary freely, we performed a sweep of β and determined that a value between 3.0 and 4.0 gives the best resulting residuals. Inside of this range, there is a trade off in performance of the fitting function between the low- and high-energy sides of the distribution. However, these constraints were somewhat arbitrarily chosen and are not founded on any results from systematic studies of our detector with different calibration sources. Further studies are required before we can confidently use Model 3 as a fitting function. To continue with fitting the distributions in the presence

Centroid [keV]	FWHM [keV]
79.607 ±0.012	0.491 ±0.011
81.002 ±0.001	0.483 ±0.001
302.867 ±0.010	0.902 ±0.009
356.000 ±0.006	0.999 ±0.006

Table 4.2: A table of the centroids and FWHM for the four peaks used in the energy calibration at 0 T.

of the B-field, we only report values estimated from Model 2. However, we still show the fit with Model 3 because it gives us an idea of how well the function can perform.

To calibrate the energy of the measurement system, we performed a linear calibration with all of the four peaks using Model 2 as a fitting function. The DSPEC system shows good linearity between the centroids of these four peaks. Table 4.2 gives the centroids and FWHM of the four peaks used in the linear energy calibration at 0 T.

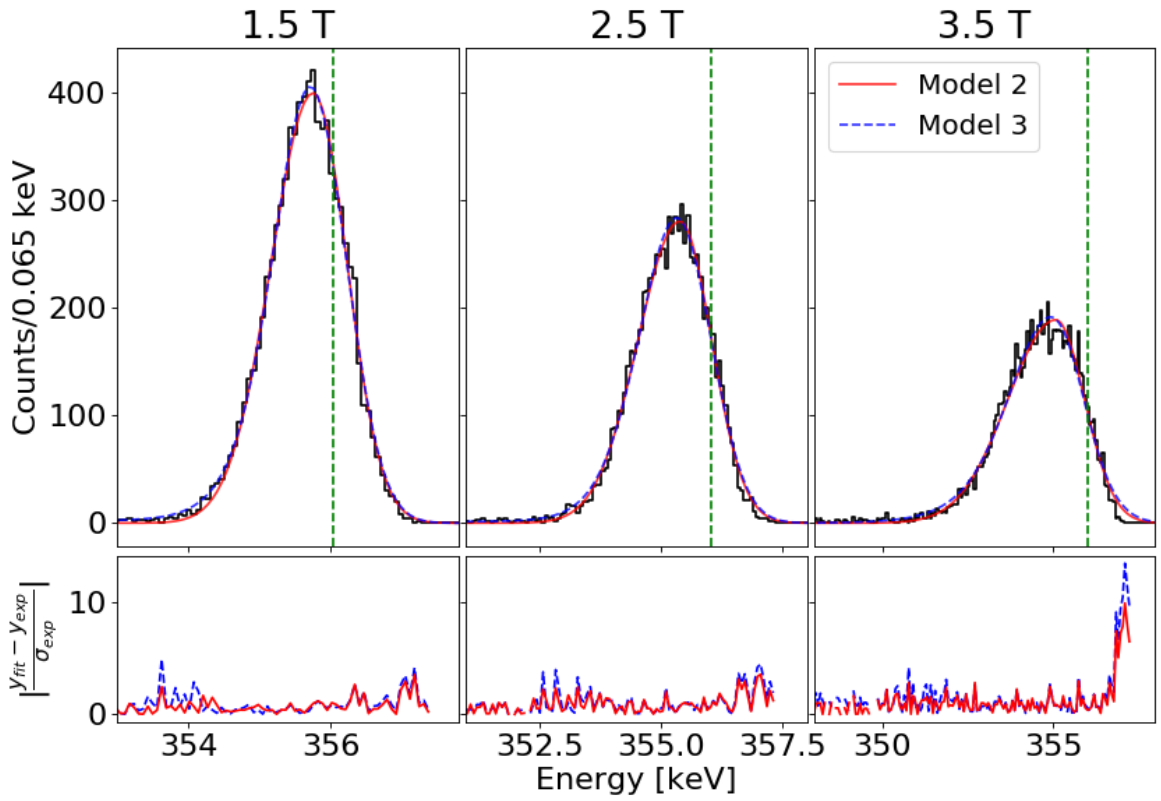

Figure 4.8: A plot comparing the fitting of the functions for Model 2 and Model 3 on the 356 keV peak as a function of the B-field at the trap center. For reference, the vertical dashed line on each plot marks the centroid of the distribution at 0 T.

Now we can attempt to fit the peak distributions when the B-field is present. Since there is obvious skewness in the distributions, we only use Models 2 and 3 as fitting functions. To illustrate the fitting results, we show the 356 keV peak. Figure 4.8 shows a plot of the 356 keV peak at three different values of the B-field. Each distribution is fitted with Models 2 (red) and 3 (dashed blue) and a green dashed vertical line is drawn in reference to the center of the distribution at 0 T. At 3.5 T on the high energy side of the peak, the residuals show that both model fits deviate from the distribution significantly. This indicates that the distribution deviates from the Poisson statistics that lead to a Gaussian shape. On the low energy side of the peak, we see that both fitting functions seem to estimate the distribution reasonably as the B-field increases.

As we discussed qualitatively at the beginning of section 4.2, when the B-field

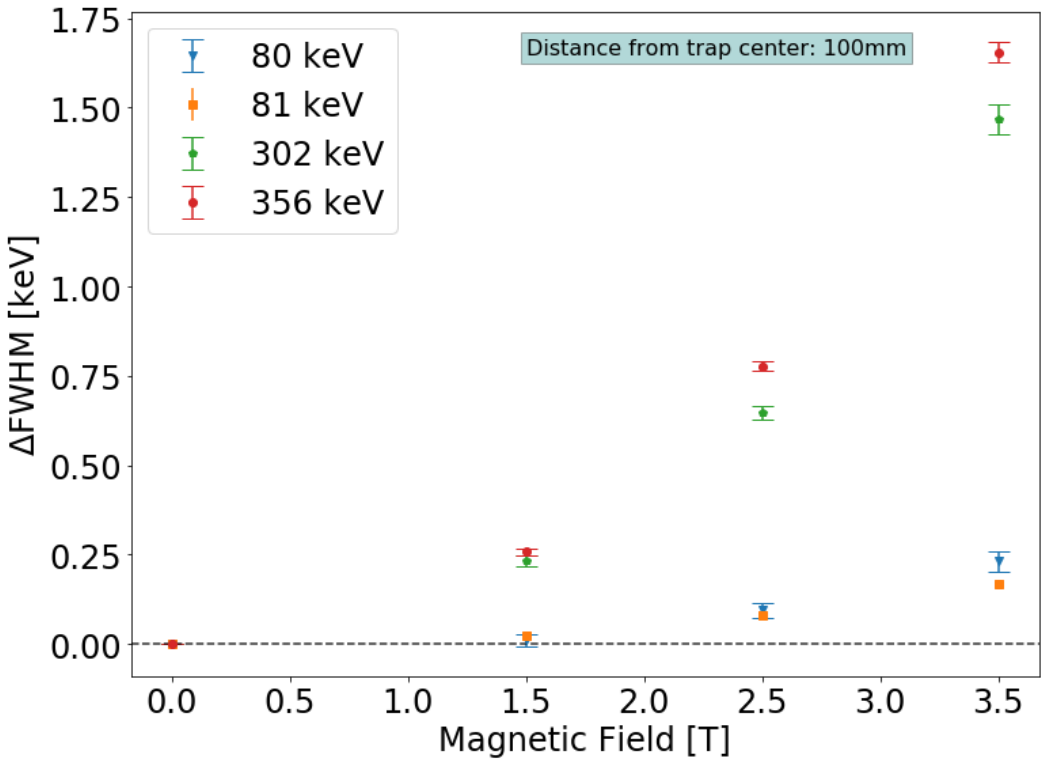

Figure 4.9: A plot showing the change in FWHM for each peak as a function of the magnetic field at the trap center.

reaches 4.5 and 5.5 T, the distributions are very clearly distorted from anything our fitting functions might be able to represent. The 80 and 81 keV peaks become indistinguishable from each other and the 302 and 356 keV peaks look almost like two separate distributions. As such, we give the results up to 3.5 T for the bi-Gaussian fitting.

Figure 4.9 plots the FWHM of each of the four peaks as a function of the magnetic field. Figure 4.10 shows the shift in peak center of the four peaks as a function of the magnetic field. Here, we have taken the absolute value so that a positive shift in peak center means the center is moving in the direction of lower energy. These results are in good agreement with the work performed by Agnello *et al.* [78] on coaxial HPGe detectors operating in magnetic fields up to 2.5 T.

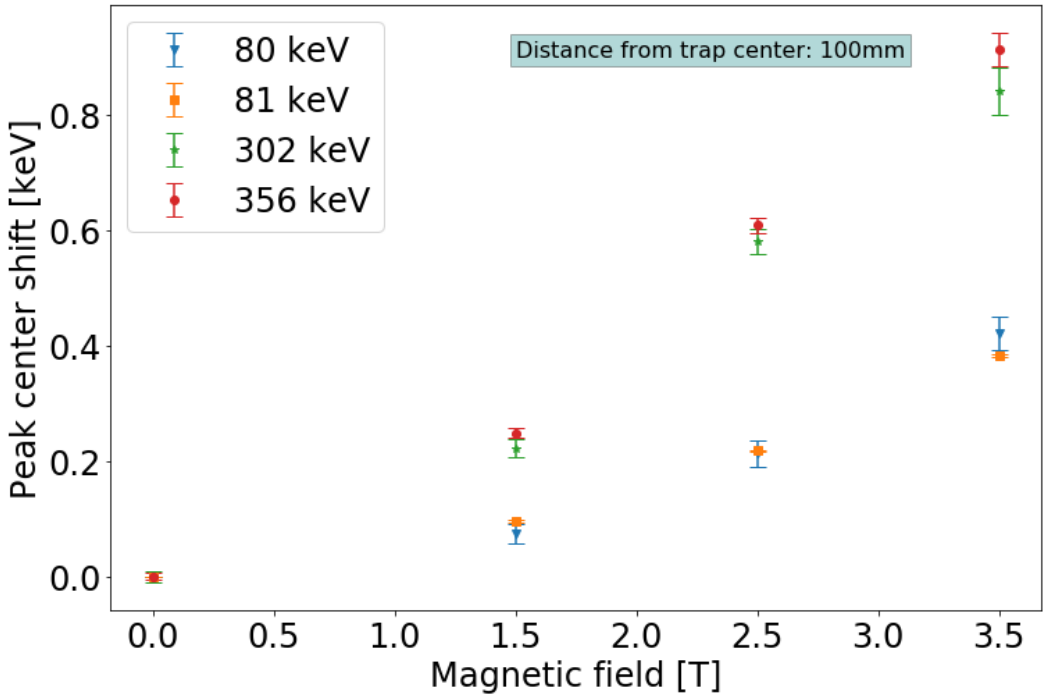

Figure 4.10: A plot of the shift in peak centers of the four photopeaks as a function of magnetic field at the trap center.

4.3 MDPP-16 Time and Amplitude Digitizer

Once the MDPP-16 was installed into the EBIT spectroscopy crate, we began to gather calibration data for tuning the operating parameters. Due to the mounting constraints of the sources explained in section 3.1, the event rate registered by the MDPP-16 was between 1 and 10 events/second depending on the source. As such, it was difficult to obtain enough statistics because long measurement times were required. At 0 T, The MDPP-16 showed very good channel linearity between the peaks at 81, 356, and 660 keV. All of the peaks were fitted with a Gaussian function with a background composed of a step and a linear function. A linear energy calibration was performed using the fitting results for the 81, 356, and 660 keV peaks.

Figure 4.11 presents a plot comparing the calculated FWHM values (at B=0 T) as a function of gamma-ray for both the DSPEC and MDPP-16 units. The results show

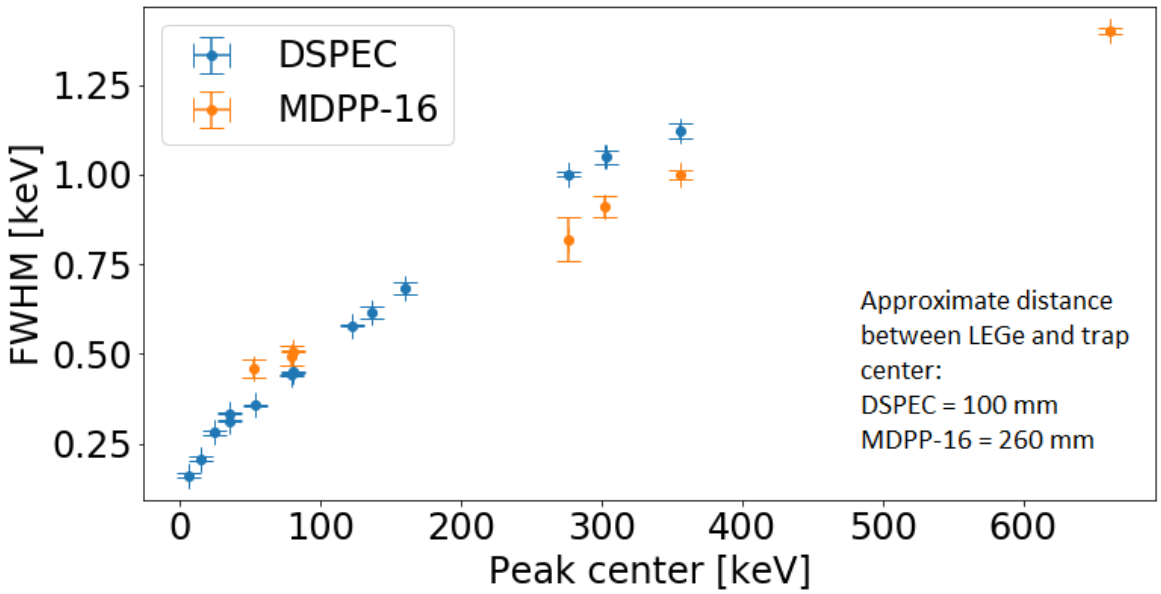

Figure 4.11: A plot comparing the calculated values of FWHM (at B=0 T) as a function of gamma-ray energy between the DSPEC and MDPP-16 units.

Parameter	Value
Timing filter differentiation time	0.250 μs
Coarse gain (jumpers)	1 V 96 Ω
Fine gain	2.18
Shaping time	3 μs
Reset time	50 μs
Signal rise time	1 μs

Table 4.3: MDPP-16 running parameters

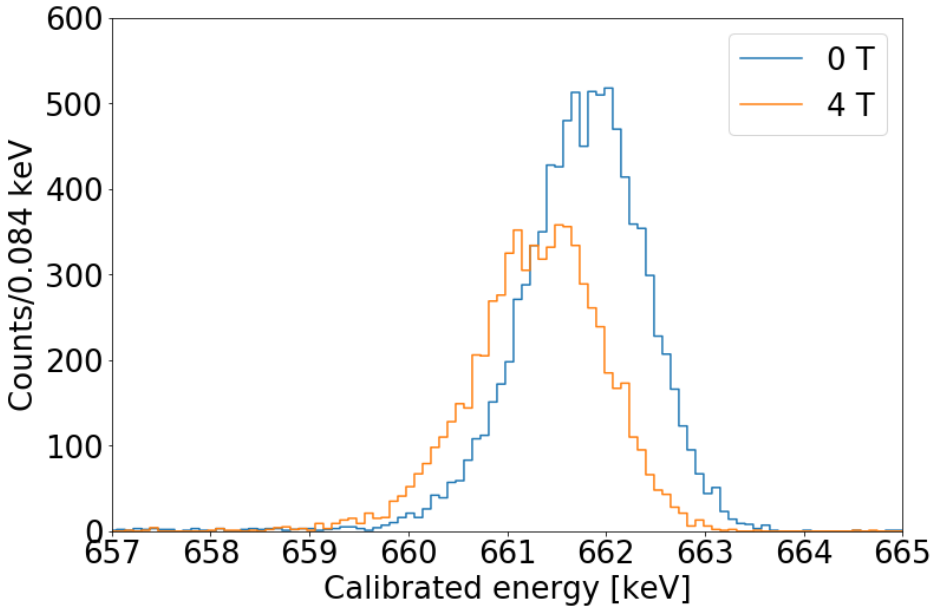

Figure 4.12: A photon spectrum recorded with the MDPP-16 shows the 661 keV peak from ^{137}Cs being affected by the magnetic field. The reported magetic field is at the trap center and the detector crystal is approximately 260 mm from the center.

that the MDPP-16 performs better in the range above ∼250 keV, but the DSPEC performs better in the energy range below ∼100 keV. Table 4.3 gives the MDPP-16 running parameters that were used to obtain these results. Our ability to change the value of the EBIT's magnetic field to study its affect on the photon spectra recorded with the MDPP-16 was limited. This was due to a nearby experiment being sensitive to the magnetic field, and as such we only had one opportunity to change the value and could not make measurements at multiple values. Comparison between the 4 T dataset and the 0 T dataset shows that the effect of the magnetic field still persists. This is displayed in figure 4.12 which shows the 661 keV peak from ^{137}Cs.

4.4 Lecroy Wavesurfer 3054

We first present the results from capturing ∼50,000 waveforms with low timing resolution. In capturing the waveforms, the largest voltage step we identified was approxi-

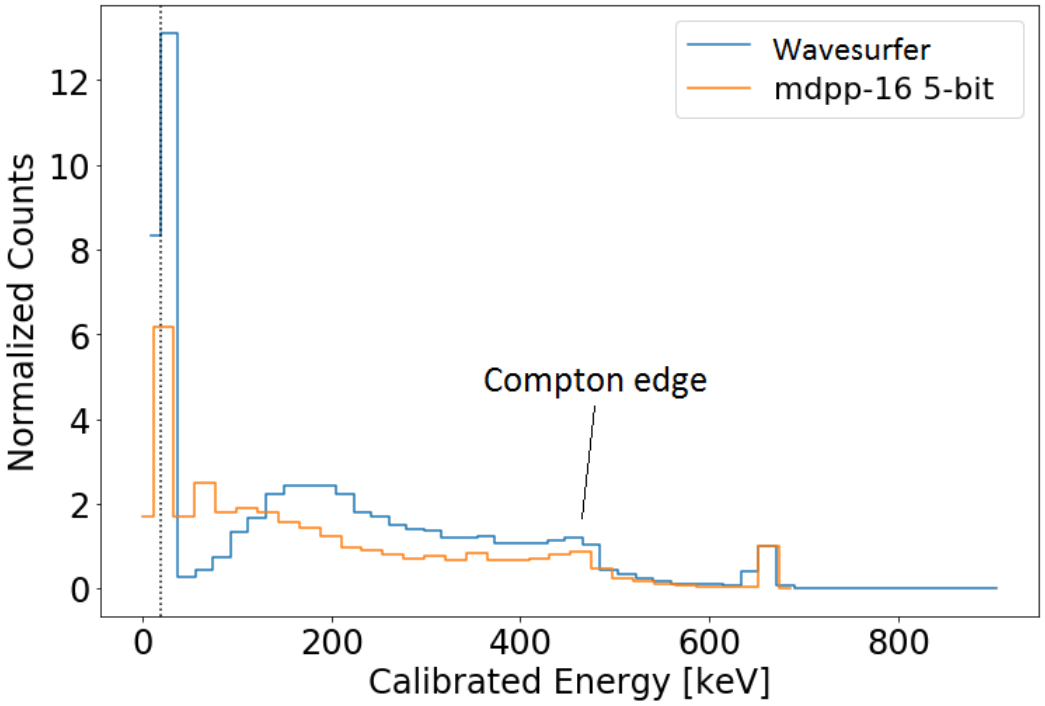

Figure 4.13: A plot showing a re-binned 5-bit MDPP-16 histogram overlapped with a histogram generated with the waveform capturing method. The MDPP-16 histogram is calibrated with the sharp lines at 660 and 81 keV and the waveform-captured histogram is calibrated with just the 660 keV peak alone. The vertical black dotted line on the left side of the graph shows the voltage resolution of the oscilloscope which is 0.021 V (∼19 keV calibrated). The counts are normalized to the total number of counts in the 660 keV bin.

mately centered around 0.45 V, which we interpret to be the highest energy photopeak at 660 keV from the ^{137}Cs source. Figure 4.13 shows the step-generated histogram overlapped with a re-binned 5-bit MDPP-16 histogram for comparison. The MDPP-16 histogram is calibrated using the 81 keV and 660 keV peaks and the step-generated histogram is calibrated using only the 660 keV peak. The latter decision was made because there is no clear indicator of other peaks in the histogram. For display purposes, both histograms are normalized to the total number of counts in the 660 keV peak. We observe that the Compton edge associated with the 660 keV peak lines up nicely between the two histograms. However, in the low energy region between 0 and 200 keV, there is discrepancy between the two histograms. In particular, the "knuckle"

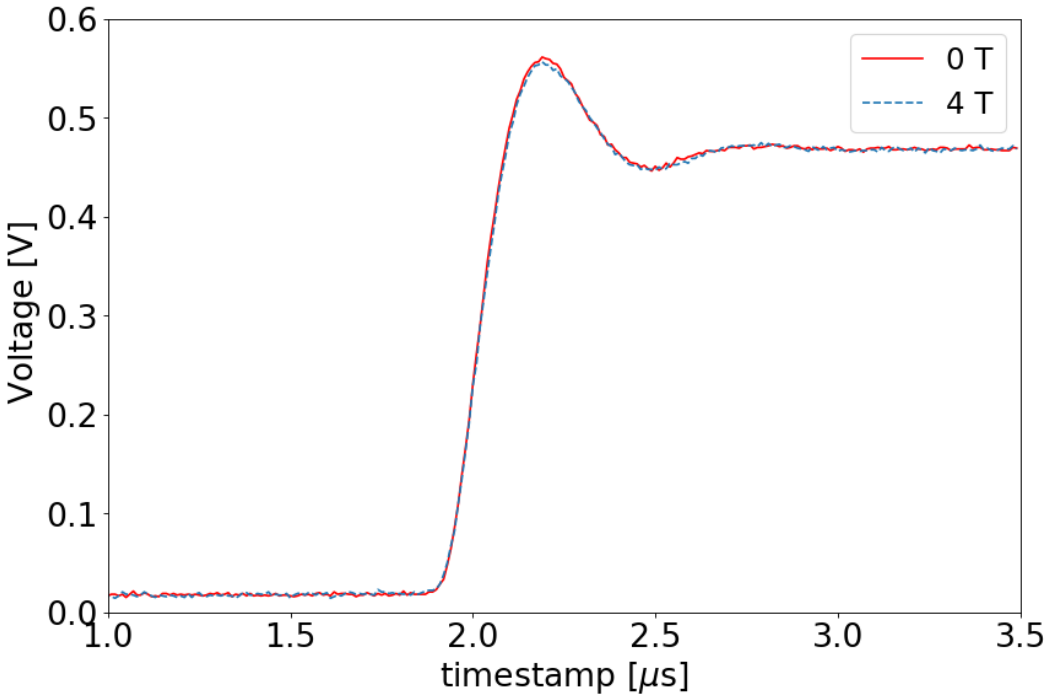

Figure 4.14: Comparison between voltage steps of the 660 keV peak at 0 T and 4 T at the trap center. Both signals are averaged over 42 recorded waveforms.

just below 200 keV of the step-generated histogram seems to fall off too quickly at lower energies in comparison to the MDPP-16 histogram. This discrepancy is possibly due to a systematic problem with estimating the point between the two linear interpolations when determining the step height. Further investigation is needed.

Despite the discrepancy, we have enough confidence that we have identified the 660 keV peak and can begin to study how the B-field affects the voltage step. As mentioned in section 3.4, we also captured waveforms with a slightly higher timing resolution with the EBIT magnet at 0 T and 4 T. After we performed linear interpolation to determine the step heights, we averaged the waveforms occurring in the same energy bin to look for differences between 0 T and 4 T datasets. Figure 4.14 shows the averaged waveforms for 0 T and 4 T. From this plot it is obvious that there is no noticeable difference in step characteristics such as the rise time. It is important to remind the reader that the value of 4 T is for the center of the EBIT. Given the positioning of the

detector at the time of capturing these waveforms, we estimate the B-field at the Ge crystal to be approximately ∼0.2 T. Therefore, this result is consistent with current literature on HPGe operating in B-fields: Sanches Lorente *et al.* show a similar plot comparing averaged voltage steps for a 1.336 MeV line (^{60}Co) between 0 T and 1.6 T at the detector crystal [77]. Averaging over 5000 events at both values of the magnetic field, they observed an approximately 0.3 μs increase in pulse rise time with B=1.6 T. Other publications on this topic such as [76] and [78] do not discuss observations of the characteristics of the voltage steps for different magnetic field values. Therefore it is likely that the results in figure 4.14 are simply because the magnetic field was too weak to cause any effects on the signal current from a deposited photon.

To obtain the proper signal amplitude from the LEGe, we split the output and terminated one side with 50 Ω to ground. This 50 Ω termination is then in parallel with the oscilloscope and the preamplifier output stage sees the correct impedance of approximately ∼50Ω. There is however still the problem of signal reflections from the 1 MΩ input impedance of the Wavesurfer. In Figure 4.14, following the rising edge of the voltage step there is a noticeable oscillation that decays to the final step height. We have identified that this is due to the presence of the large input impedance of the Wavesurfer [132]. The same characteristic decaying oscillation is also observed following reset periods of the preamplifier output. As of writing, we are unsure exactly what effect this has on our results and more exploration is needed. In section 3.4, we detailed the method of determining the voltage step heights by taking the difference between two linear interpolations on each side of the voltage step. A benefit of performing these linear interpolations is that the value of the slope gives us the detectors leakage current after integration by the preamplifier. Figure 4.15 shows a histogram built from these measured slopes compared between 0 T and 4 T. There is a clear increase in the slope of the leakage current from ∼400 V/s to ∼450 V/s as the magnetic field increases.

As a sample calculation, consider that our detector resets at a relative saturation

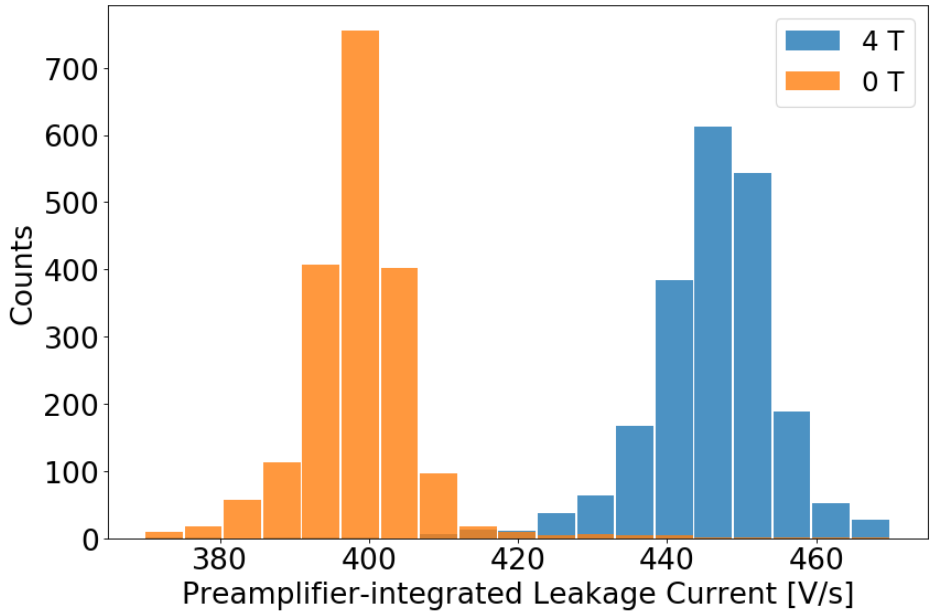

Figure 4.15: The distributions of calculated leakage current slopes for both 0 T and 4 T at the trap center. When the magnetic field is turned on, we observe that the slope increases from ∼400 to ∼445 V/s.

voltage of ∼3 V. Without the B-field, that means a typical live interval is 7.50 ms as opposed to 6.66 ms with the magnet set at 4 T. The reset period requires approximately 4 μs and therefore the dead time is nearly 0.053% without the B-field and 0.060% with the B-field. At a count rate of 10 events/second and a total measurement period of 1 hr, we expect 34,092 counts without the B-field and 33,840 counts with the B-field. This count difference is only barely outside of one standard deviation of the expected total counts for Poisson statistics. Therefore, even if we did not know the dead time, this increase in leakage current would not cause a significant enough change in counts to notice. Our observations in this section do not cover the range of magnetic field necessary to corroborate the DSPEC observations presented in section 4.2.1. Therefore, future studies of the leakage current and how it contributes to noise and dead time are required.

Chapter 5

Conclusion and outlook

5.1 Summary

In this work we have studied the consequences of operating a high-purity low-energy germanium semiconductor detector in a magnetic field. The motivation to understand this is within the context of developing methods for in-trap decay spectroscopy studies at the TITAN-EBIT. Because past literature has demonstrated that silicon drift detectors and coaxial HPGe detectors will lose efficiency and resolution when operated in a magnetic field, this becomes a crucial concern for the EC BR and 2-gamma experimental proposals outlined in sections 1.3.2 and 1.3.3. In our approach to study this effect on our own detector, we used three different devices to record data: an Ortec DSPEC amplitude digitizer, a Lecroy Wavesurfer 3054 high bandwidth oscilloscope, and a Mesytec MDPP-16 time and amplitude digitizer.

Data from the DSPEC was recorded prior to this thesis work and was performed with the LEGe approximately 100 mm from the trap center where Figure 4.1 shows the simulated strength. With the DSPEC, photopeak spectra from ^{133}Ba were recorded for six different values of the EBIT's magnetic field. In this work, we performed analyses using simple channel integration and fitting functions to study the efficiency and

resolution of the detector.

Data with the MDPP-16 was recorded during this thesis work in two separate instances: 1) for calibration and optimization before on-line experiment S1478 and 2) during experiment S1478. In both instances, the detector was positioned approximately 260 mm from the trap center. During the study prior to experiment S1478, photopeak spectra from ^{133}Ba and ^{137}Cs were recorded with the EBIT magnetic field at 0 and 4 T.

Finally, the Wavesurfer oscilloscope was used to record the live intervals of the LEGe's transistor reset preamplifier. During collection, the detector was positioned approximately 260 mm from the trap center. From the live intervals we extracted the voltage steps produced by incident photons from ^{133}Ba and ^{137}Cs sources. At 0 T, a set of low timing resolution data was recorded and this contained approximately 50,000 waveforms. This data was used to build a photopeak histogram and compared to a low-resolution MDPP-16 histogram for validation and to identify the highest energy photopeak (660 keV). After this, we recorded voltage step data at a higher timing resolution for magnetic field values of 0 T and 4 T. This data was then used to look for any characteristic differences of the 660 keV voltage step between 0 T and 4 T. We also used this data to evaluate the detector's leakage current as a function of the magnetic field.

5.2 Discussion and Outlook

5.2.1 DSPEC

In section 4.2.1 we observed the fractional count rate of four different regions as a function of the magnetic field. To rule out a dependency on how the channels ranges were chosen, we also looked at the fractional count rate for regions that were contracted and expanded in channel range relative to the originals. Figures 4.4, B.1, and B.2 display that the detection efficiency starts to drop at around 3.5 T and that this effect

is dependent on the photon energy. Figure 4.6 shows us that the total number of counts in the spectrum does not decrease outside of any significant uncertainty until 3.5 T. This is despite the significant shifting and broadening observed from the higher energy photopeaks even at low values of the magnetic field. From this we can conclude that up to 2.5 T, the detector resolution is affected, but the detection efficiency is not. At higher values of the magnetic field, both the detection efficiency and detector resolution are severely affected.

Figures 4.9 and 4.10 at the end of the DSPEC fitting analysis show that there is a correlation between the magnetic field and the observed shift in peak centers and FWHM. The next step would be to determine if we can apply a correction to the spectra to recover the shift and resolution as was done in the work of Agnello *et al.* [78] and Sanchez Lorente *et al.* [77]. To do so would first require a better fitting function than the bi-Gaussian that was used. The bi-Gaussian function does not have a strong theoretical basis, but is rather empirical. Model 3 (Gaussian with asymmetric Gaussian) has a much stronger theoretical basis, but requires more familiarity with the detector. Therefore, we would first like to perform more studies with the detector to better determine the parameters *STEP*, *BETA* and R mentioned in section 4.2.2.

5.2.2 MDPP-16

With the optimization of the running parameters of the Mesytec MDPP-16, we demonstrated that we could achieve a similar resolution to that of the DSPEC at 0 T. We also demonstrated that the effect of the magnetic field persists, but we did not gather enough data to perform an analysis like was done on the DSPEC data. The next step with the MDPP-16 is to perform an analysis on the magnetic-field-dependent photopeak spectra with different calibration sources, similar to that performed on the DSPEC data.

5.2.3 Wavesurfer

The data recorded with the Wavesurfer has demonstrated two results: 1) that the LEGe leakage current does increase with the magnetic field and 2) that we can study the effects of the magnetic field by recording high resolution voltage steps. Although the past studies by Agnello *et al.* [78], Sanchez Lorente *et al.* [77], and Szymanska *et al.* [76] have speculated that an enhanced Penning effect might result in an increased surface current, none of them have reported any observations. Despite observing an increase in leakage current, it remains unknown if this will cause a significant increase in detector dead-time because we only have two data points. Since the data we have taken is very limited, we would like to return to this method again to obtain more data points.

A simple study that we propose is to measure the leakage current through the detector as a function of the magnetic field in the absence of ionizing radiation. During this measurement, we would also have the opportunity to test if the detector electronics are affected by the magnetic field because this is something we did not address in this work. The LEGe preamplifier has an input that allows us to feed in a known signal and can be used to monitor the stability of the electronics over time. If we observe a significant increase in leakage current, the corresponding increase in detector dead time could explain some of the observed loss in detection efficiency.

Our results from the voltage step capturing are promising. We would like to redo the measurement but with multiple values of the magnetic field and with different size voltage steps. If we successfully observe characteristic differences in the voltage steps, the next step is to study how the shaping and digitizing circuit of the MDPP-16 responds to the voltage steps. This would provide insight to what can be done to mitigate the effects.

In addition, the impedance mismatch caused by the 1 MΩ input of the Wavesurfer needs to be addressed. A simple way to address this is to completely avoid it and to

use a 50 Ω oscilloscope that is purposed for high frequency circuits.

Another avenue we can traverse is to use one of the programs available with Radware [118] called Siggen. This is a finite element software that simulates detector signals generated by incident radiation and offers the option to apply an external magnetic field. The results from this could be used with our studies to infer more information about the physical processes occurring in the detector when the magnetic field is present.

5.3 Conclusion

To conclude, we have determined that depending on the magnetic field strength, there are more of less severe effects on the performance of the LEGe. This is characterized by the resolution and detection efficiency of the detector. We have also demonstrated that the leakage current through the LEGe does increase with the magnetic field; however the mechanism behind this is still unknown. We have briefly discussed future measurements that we can perform to further investigate these effects and to possibly develop a method to compensate for them.

Appendix A

Detector Drawings

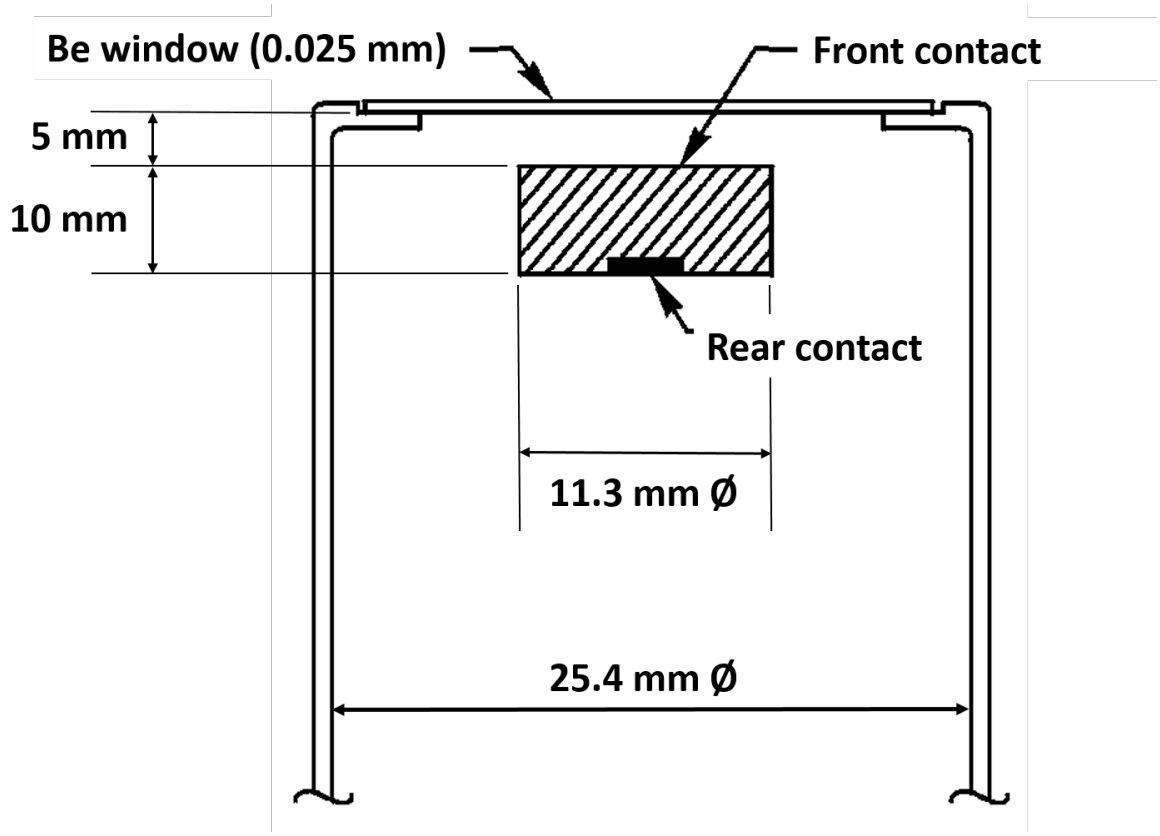

Figure A.1: A schematic of the LEGe detector in its endcap. The HPGe crystal sits inside of a cryostat at vacuum below 10^{-6} torr. The front contact is the p^+ side and the rear contact is the n^+ side.

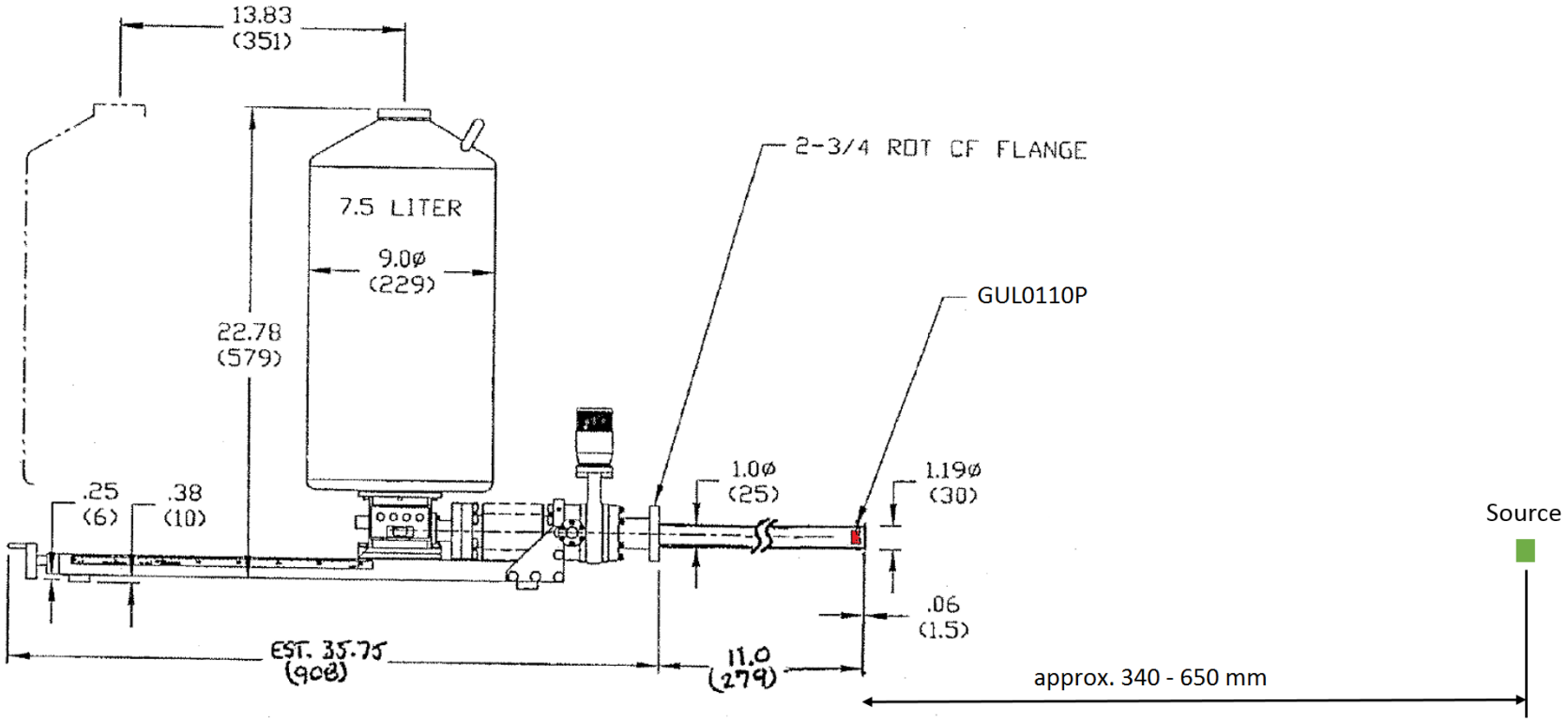

Figure A.2: A schematic of the retractable cryostat (Canberra model Nº GUL0110P). The LEGe detector is housed at the tip and shown as a red box. The placement of the radioactive calibration sources is shown with a green box.

Appendix B

Extra Plots

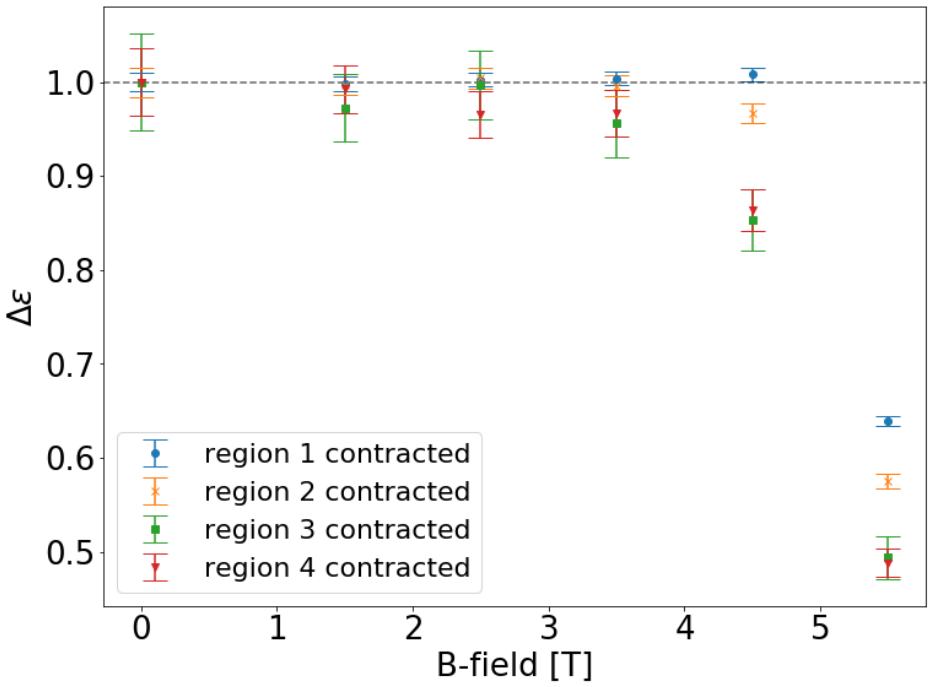

Figure B.1: The fractional count rate with the channel range contracted from the original four regions.

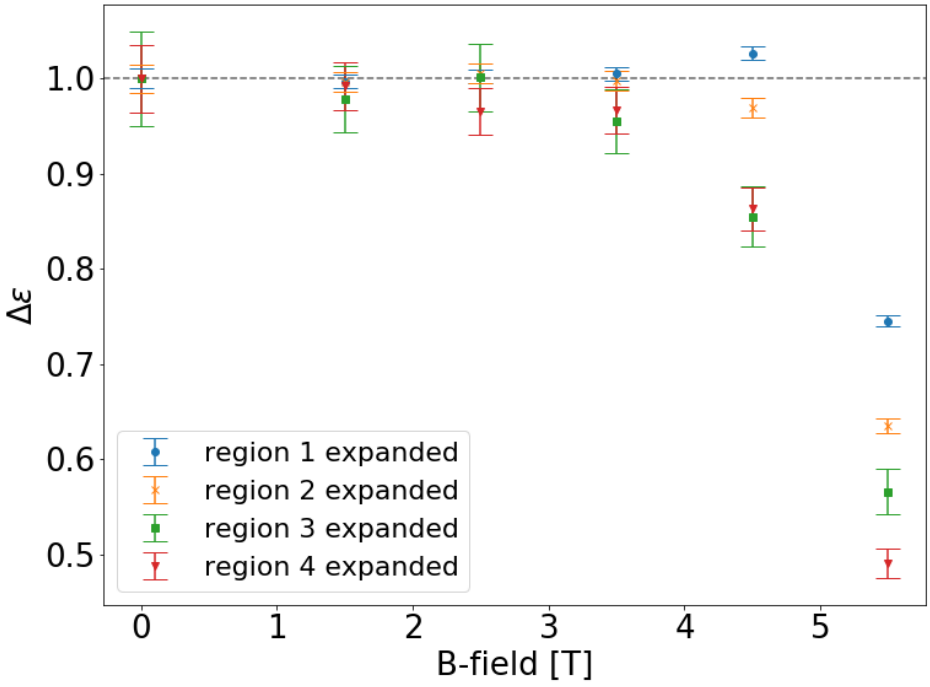

Figure B.2: The fractional count rate with the channel range expanded from the original four regions.

Bibliography

[1] *Research Topics*. accessed: 28-05-2018. URL: http://www.triumf.ca/research-program/research-topics.

[2] *Main Cyclotron and Beam Lines*. accessed: 28-05-2018. URL: http://www.triumf.ca/research-program/research-facilities/main-cyclotron-beam-lines.

[3] M. Dombsky et al. "Commissioning and initial operation of a radioactive beam ion source at ISAC". In: *Review of Scientific Instruments* 71.2 (2000), pp. 978–980. DOI: 10.1063/1.1150364. eprint: https://doi.org/10.1063/1.1150364. URL: https://doi.org/10.1063/1.1150364.

[4] *TRIUMF Center for Molecular and Materials Science*. accessed: 28-05-2018. URL: http://cmms.triumf.ca/.

[5] J. Dilling, R. Krücken, and G. Ball. "ISAC overview". In: *Hyperfine Interactions* 225.1 (Jan. 2014), pp. 1–8. ISSN: 1572-9540. DOI: 10.1007/s10751-013-0877-7. URL: https://doi.org/10.1007/s10751-013-0877-7.

[6] Y. Blumenfeld, T Nilsson, and P. Van Duppen. "Facilities and methods for radioactive ion beam production". In: *Physica Scripta* 2013.T152 (2013), p. 014023. URL: http://stacks.iop.org/1402-4896/2013/i=T152/a=014023.

[7] *TRIUMF-ISAC*. accessed: 01-06-2018. URL: https://www.mines.edu/electroweak/triumf-isac/.

[8] P. Bricault et al. “High power target developments at ISAC”. In: *Nuclear Instruments and Methods in Physics Research Section B: Beam Interactions with Materials and Atoms* 204 (2003). 14th International Conference on Electromagnetic Isotope Separators and Techniques Related to their Applications, pp. 319–324. ISSN: 0168-583X. DOI: https://doi.org/10.1016/S0168-583X(03)00504-4. URL: http://www.sciencedirect.com/science/article/pii/S0168583X03005044.

[9] J. Dilling, R. Krücken, and L. Merminga. *ISAC and ARIEL: The TRIUMF radioactive beam facilities and the scientific program*. Springer, Dordrecht, Jan. 2014, pp. 1–284. DOI: 10.1007/978-94-007-7963-1.

[10] A. A. Kwiatkowski et al. “TITAN: An ion trap facility for on-line mass measurement experiments”. In: *Hyperfine Interactions* 225.1 (Jan. 2014), pp. 143–155. ISSN: 1572-9540. DOI: 10.1007/s10751-013-0892-8. URL: https://doi.org/10.1007/s10751-013-0892-8.

[11] S. Paul. personal communication. May 2018.

[12] T. Brunner et al. “TITAN’s digital RFQ ion beam cooler and buncher, operation and performance”. In: *Nuclear Instruments and Methods in Physics Research Section A: Accelerators, Spectrometers, Detectors and Associated Equipment* 676 (2012), pp. 32–43. ISSN: 0168-9002. DOI: https://doi.org/10.1016/j.nima.2012.02.004. URL: http://www.sciencedirect.com/science/article/pii/S0168900212001398.

[13] Christian Jesch et al. “The MR-TOF-MS isobar separator for the TITAN facility at TRIUMF”. In: *Hyperfine Interactions* 235.1 (Nov. 2015), pp. 97–106. ISSN: 1572-9540. DOI: 10.1007/s10751-015-1184-2. URL: https://doi.org/10.1007/s10751-015-1184-2.

[14] A. Lapierre et al. "The TITAN EBIT charge breeder for mass measurements on highly charged short-lived isotopes—First online operation". In: *Nuclear Instruments and Methods in Physics Research Section A: Accelerators, Spectrometers, Detectors and Associated Equipment* 624.1 (2010), pp. 54–64. ISSN: 0168-9002. DOI: https://doi.org/10.1016/j.nima.2010.09.030. URL: http://www.sciencedirect.com/science/article/pii/S0168900210020231.

[15] D. Lascar et al. "A novel transparent charged particle detector for the CPET upgrade at TITAN". In: *Nuclear Instruments and Methods in Physics Research Section A: Accelerators, Spectrometers, Detectors and Associated Equipment* 868 (2017), pp. 133–138. ISSN: 0168-9002. DOI: https://doi.org/10.1016/j.nima.2017.07.003. URL: http://www.sciencedirect.com/science/article/pii/S0168900217307143.

[16] M. Brodeur et al. "New mass measurement of ^{6}Li and ppb-level systematic studies of the Penning trap mass spectrometer TITAN". In: *Phys. Rev. C* 80 (4 Oct. 2009), p. 044318. DOI: 10.1103/PhysRevC.80.044318. URL: https://link.aps.org/doi/10.1103/PhysRevC.80.044318.

[17] V. V. Simon et al. "Penning-trap mass spectrometry of highly charged, neutron-rich Rb and Sr isotopes in the vicinity of $\mathbf{A \approx 100}$". In: *Phys. Rev. C* 85 (6 June 2012), p. 064308. DOI: 10.1103/PhysRevC.85.064308. URL: https://link.aps.org/doi/10.1103/PhysRevC.85.064308.

[18] R. Klawitter et al. "Mass measurements of neutron-rich Rb and Sr isotopes". In: *Phys. Rev. C* 93 (4 Apr. 2016), p. 045807. DOI: 10.1103/PhysRevC.93.045807. URL: https://link.aps.org/doi/10.1103/PhysRevC.93.045807.

[19] U. Chowdhury et al. "First direct mass measurement of the neutron-deficient nucleus ^{24}Al". In: *Phys. Rev. C* 92 (4 Oct. 2015), p. 045803. DOI: 10.1103/

PhysRevC.92.045803. URL: https://link.aps.org/doi/10.1103/PhysRevC.92.045803.

[20] S. Malbrunot-Ettenauer et al. "Penning trap mass measurements utilizing highly charged ions as a path to benchmark isospin-symmetry breaking corrections in ^{74}Rb". In: *Phys. Rev. C* 91 (4 Apr. 2015), p. 045504. DOI: 10.1103/PhysRevC.91.045504. URL: https://link.aps.org/doi/10.1103/PhysRevC.91.045504.

[21] A. T. Gallant et al. "Breakdown of the Isobaric Multiplet Mass Equation for the $A = 20$ and 21 Multiplets". In: *Phys. Rev. Lett.* 113 (8 Aug. 2014), p. 082501. DOI: 10.1103/PhysRevLett.113.082501. URL: https://link.aps.org/doi/10.1103/PhysRevLett.113.082501.

[22] A. T. Gallant et al. "Mass determination near $N = 20$ for Al and Na isotopes". In: *Phys. Rev. C* 96 (2 Aug. 2017), p. 024325. DOI: 10.1103/PhysRevC.96.024325. URL: https://link.aps.org/doi/10.1103/PhysRevC.96.024325.

[23] E. Leistenschneider et al. "Dawning of the $N = 32$ Shell Closure Seen through Precision Mass Measurements of Neutron-Rich Titanium Isotopes". In: *Phys. Rev. Lett.* 120 (6 Feb. 2018), p. 062503. DOI: 10.1103/PhysRevLett.120.062503. URL: https://link.aps.org/doi/10.1103/PhysRevLett.120.062503.

[24] M. Smith et al. "First Penning-Trap Mass Measurement of the Exotic Halo Nucleus ^{11}Li". In: *Phys. Rev. Lett.* 101 (20 Nov. 2008), p. 202501. DOI: 10.1103/PhysRevLett.101.202501. URL: https://link.aps.org/doi/10.1103/PhysRevLett.101.202501.

[25] M. Brodeur et al. "First Direct Mass Measurement of the Two-Neutron Halo Nucleus ^{6}He and Improved Mass for the Four-Neutron Halo ^{8}He". In: *Phys. Rev.*

Lett. 108 (5 Jan. 2012), p. 052504. DOI: 10.1103/PhysRevLett.108.052504. URL: https://link.aps.org/doi/10.1103/PhysRevLett.108.052504.

[26] A. A. Kwiatkowski et al. "New determination of double-β-decay properties in ^{48}Ca: High-precision $Q_{\beta\beta}$-value measurement and improved nuclear matrix element calculations". In: *Phys. Rev. C* 89 (4 Apr. 2014), p. 045502. DOI: 10.1103/PhysRevC.89.045502. URL: https://link.aps.org/doi/10.1103/PhysRevC.89.045502.

[27] T. D. Macdonald et al. "Precision Penning-trap measurement to investigate the role of the ^{51}Cr$(e^-, \nu_e)^{51}$V Q value in the gallium anomaly". In: *Phys. Rev. C* 89 (4 Apr. 2014), p. 044318. DOI: 10.1103/PhysRevC.89.044318. URL: https://link.aps.org/doi/10.1103/PhysRevC.89.044318.

[28] D. Frekers et al. "Penning-trap Q-value determination of the Ga71(ν, e−)Ge71 reaction using threshold charge breeding of on-line produced isotopes". In: *Physics Letters B* 722.4 (2013), pp. 233–237. ISSN: 0370-2693. DOI: https://doi.org/10.1016/j.physletb.2013.04.019. URL: http://www.sciencedirect.com/science/article/pii/S0370269313002980.

[29] K. Blaum. "High-accuracy mass spectrometry with stored ions". In: *Physics Reports* 425.1 (2006), pp. 1–78. ISSN: 0370-1573. DOI: https://doi.org/10.1016/j.physrep.2005.10.011. URL: http://www.sciencedirect.com/science/article/pii/S0370157305004643.

[30] Alinka Lépine-Szily. "Experimental Overview of Mass Measurements". In: *Atomic Physics at Accelerators: Mass Spectrometry*. Ed. by David Lunney, Georges Audi, and H.-Jürgen Kluge. Dordrecht: Springer Netherlands, 2001, pp. 35–57. ISBN: 978-94-015-1270-1.

[31] J. D. Prestage, G. J. Dick, and L. Maleki. "New ion trap for frequency standard applications". In: *Journal of Applied Physics* 66.3 (1989), pp. 1013–1017. DOI:

10.1063/1.343486. eprint: https://doi.org/10.1063/1.343486. URL: https://doi.org/10.1063/1.343486.

[32] Wolfgang R Plaß et al. "High-performance multiple-reflection time-of-flight mass spectrometers for research with exotic nuclei and for analytical mass spectrometry". In: *Physica Scripta* 2015.T166 (2015), p. 014069. URL: http://stacks.iop.org/1402-4896/2015/i=T166/a=014069.

[33] M. Froese et al. "A high-current electron beam ion trap as an on-line charge breeder for the high precision mass measurement TITAN experiment". In: *TCP 2006*. Ed. by J. Dilling et al. Springer Berlin Heidelberg, 2007, pp. 241–248. ISBN: 978-3-540-73466-6.

[34] M. Blessenohl. personal communication. Nov. 2015.

[35] Gabriel Herrmann. "Optical Theory of Thermal Velocity Effects in Cylindrical Electron Beams". In: *Journal of Applied Physics* 29.2 (1958), pp. 127–136. DOI: 10.1063/1.1723053. eprint: https://doi.org/10.1063/1.1723053. URL: https://doi.org/10.1063/1.1723053.

[36] T D Märk. "Ionization by electron impact". In: *Plasma Physics and Controlled Fusion* 34.13 (1992), p. 2083. URL: http://stacks.iop.org/0741-3335/34/i=13/a=044.

[37] R. E. Marrs, S. R. Elliott, and D. A. Knapp. "Production and Trapping of Hydrogenlike and Bare Uranium Ions in an Electron Beam Ion Trap". In: *Phys. Rev. Lett.* 72 (26 June 1994), pp. 4082–4085. DOI: 10.1103/PhysRevLett.72.4082. URL: https://link.aps.org/doi/10.1103/PhysRevLett.72.4082.

[38] A. Lennarz. "In-trap decay spectroscopy on highly-charged radioactive ions towards measurements of intermediate nuclei in $\beta\beta$ decay". PhD thesis. Westfaelischen Wilhelms-Universitaet Muenster, 2015.

[39] K.G. Leach et al. "The TITAN in-trap decay spectroscopy facility at TRIUMF". In: *Nuclear Instruments and Methods in Physics Research Section A: Accelerators, Spectrometers, Detectors and Associated Equipment* 780 (2015), pp. 91–99. ISSN: 0168-9002. DOI: https://doi.org/10.1016/j.nima.2014.12.118. URL: http://www.sciencedirect.com/science/article/pii/S0168900215001023.

[40] S. Dobrodey. personal communication. Nov. 2015.

[41] Wolfgang Lotz. "An empirical formula for the electron-impact ionization cross-section". In: *Zeitschrift für Physik* 206.2 (Apr. 1967), pp. 205–211. ISSN: 0044-3328. DOI: 10.1007/BF01325928. URL: https://doi.org/10.1007/BF01325928.

[42] Nagayasu Oshima et al. "Project to produce cold highly charged ions using positron and electron cooling techniques". In: *Journal of Physics: Conference Series* 2.1 (2004), p. 127. URL: http://stacks.iop.org/1742-6596/2/i=1/a=016.

[43] Z Ke. "A cooler ion trap for the TITAN on-line trapping facility at TRIUMF". PhD thesis. University of Manitoba, 2008.

[44] L. S. Brown and G. Gabrielse. "Geonium theory: Physics of a single electron or ion in a Penning trap". In: *Rev. Mod. Phys.* 58 (1 Jan. 1986), pp. 233–311. DOI: 10.1103/RevModPhys.58.233. URL: https://link.aps.org/doi/10.1103/RevModPhys.58.233.

[45] Marshall Alan G., Hendrickson Christopher L., and Jackson George S. "Fourier transform ion cyclotron resonance mass spectrometry: A primer". In: *Mass Spectrometry Reviews* 17.1 (Dec. 1998), pp. 1–35. DOI: 10.1002/(SICI)1098-2787(1998)17:1<1::AID-MAS1>3.0.CO;2-K. eprint: https://onlinelibrary.wiley.com/doi/pdf/10.1002/%28SICI%291098-2787%281998%2917%3A1%3C1%3A%3AAID-MAS1%3E3.0.CO%3B2-K. URL: https://onlinelibrary.wiley.

com/doi/abs/10.1002/%28SICI%291098-2787%281998%2917%3A1%3C1%3A%3AAID-MAS1%3E3.0.CO%3B2-K.

[46] S. Eliseev et al. "Phase-Imaging Ion-Cyclotron-Resonance Measurements for Short-Lived Nuclides". In: *Phys. Rev. Lett.* 110 (8 Feb. 2013), p. 082501. DOI: 10.1103/PhysRevLett.110.082501. URL: https://link.aps.org/doi/10.1103/PhysRevLett.110.082501.

[47] G. Gräff, H. Kalinowsky, and J. Traut. "A direct determination of the proton electron mass ratio". In: *Zeitschrift für Physik A Atoms and Nuclei* 297.1 (Mar. 1980), pp. 35–39. ISSN: 0939-7922. DOI: 10.1007/BF01414243. URL: https://doi.org/10.1007/BF01414243.

[48] M. Koenig et al. "Quadrupole excitation of stored ion motion at the true cyclotron frequency". English (US). In: *International Journal of Mass Spectrometry* 142.1-2 (Mar. 1995), pp. 95–116. ISSN: 1387-3806. DOI: 10.1016/0168-1176(95)04146-C.

[49] G. Bollen. "Mass measurements of short-lived nuclides with ion traps". In: *Nucl. Phys.* A693 (2001), pp. 3–18. DOI: 10.1016/S0375-9474(01)00353-0.

[50] C. Carlberg et al. "The SMILETRAP facility". In: *Physica Scripta* 1995.T59 (1995), p. 196. URL: http://stacks.iop.org/1402-4896/1995/i=T59/a=025.

[51] S. Ettenauer et al. "First Use of High Charge States for Mass Measurements of Short-Lived Nuclides in a Penning Trap". In: *Phys. Rev. Lett.* 107 (27 Dec. 2011), p. 272501. DOI: 10.1103/PhysRevLett.107.272501. URL: https://link.aps.org/doi/10.1103/PhysRevLett.107.272501.

[52] Kyle G. Leach et al. "Electroweak Decay Studies of Highly Charged Radioactive Ions with TITAN at TRIUMF". In: *Atoms* 5.14 (1 2017). ISSN: 2218-2004. DOI: 10.3390/atoms5010014. URL: http://www.mdpi.com/2218-2004/5/1/14.

[53] D. Frekers, J. Dilling, and I. Tanihata. "Electron capture branching ratios for the odd–odd intermediate nuclei in double-beta decay using the TITAN ion trap facility". In: *Canadian Journal of Physics* 85.1 (2007), pp. 57–75. DOI: 10.1139/p07-009. eprint: https://doi.org/10.1139/p07-009. URL: https://doi.org/10.1139/p07-009.

[54] T. Brunner. "In-Trap Decay Spectroscopy for $\beta\beta$ Decays". PhD thesis. Technische Universität München, 2011.

[55] M. Good. personal communication. Nov. 2017.

[56] COMSOL AB. *COMSOL Multiphysics*. www.comsol.com.

[57] *Detector Specifications and Performance Data*. Canberra Industries. Aug. 2007.

[58] T. Brunner et al. "Trapped-ion decay spectroscopy towards the determination of ground-state components of double-beta decay matrix elements". In: *The European Physical Journal A* 49.11 (Nov. 2013), p. 142. ISSN: 1434-601X. DOI: 10.1140/epja/i2013-13142-4. URL: https://doi.org/10.1140/epja/i2013-13142-4.

[59] T. Brunner et al. "Design of a β-detector for TITAN-EC and the first electron-capture branching ratio measurement in a Penning trap". In: *Journal of Physics: Conference Series* 312.7 (2011), p. 072006. URL: http://stacks.iop.org/1742-6596/312/i=7/a=072006.

[60] A. Lennarz et al. "In-Trap Spectroscopy of Charge-Bred Radioactive Ions". In: *Phys. Rev. Lett.* 113 (8 Aug. 2014), p. 082502. DOI: 10.1103/PhysRevLett.113.082502. URL: https://link.aps.org/doi/10.1103/PhysRevLett.113.082502.

[61] B. M. Penetrante et al. "Evolution of ion-charge-state distributions in an electron-beam ion trap". In: *Phys. Rev. A* 43 (9 May 1991), pp. 4861–4872. DOI: 10.

1103/PhysRevA.43.4861. URL: https://link.aps.org/doi/10.1103/PhysRevA.43.4861.

[62] *Chart of nuclides*. accessed: 22-05-2018. URL: https://www.nndc.bnl.gov/chart/chartNuc.jsp.

[63] M. Rosenbusch et al. "Ion bunch stacking in a Penning trap after purification in an electrostatic mirror trap". In: *Applied Physics B* 114.1 (Jan. 2014), pp. 147–155. ISSN: 1432-0649. DOI: 10.1007/s00340-013-5702-0. URL: https://doi.org/10.1007/s00340-013-5702-0.

[64] C. Andreoiu et al. "Electron Capture Branching Ratios for the Odd-Odd Intermediate Nuclei in Double-Beta Decay using TITAN". In: (2013). URL: https://mis.triumf.ca/science/experiment/view/S1066.

[65] J. Dilling et al. "Investigating Electron-Capture Rates of Highly-Charged Ions". In: (2014). URL: https://mis.triumf.ca/science/experiment/view/S1478.

[66] C. Andreoiu et al. "In-trap decay spectroscopy measurements for double-beta decay experiments". In: (2015). URL: https://mis.triumf.ca/science/experiment/view/S1622.

[67] E. Leistenschneider. "Nuclear two-photon emission unveiled through suppression of first-order decay processes". In: (2016). URL: https://mis.triumf.ca/science/experiment/view/S1695.

[68] J. Kramp et al. "Nuclear two-photon decay in 0+ → 0+ transitions". In: *Nuclear Physics A* 474.2 (1987), pp. 412–450. ISSN: 0375-9474. DOI: https://doi.org/10.1016/0375-9474(87)90625-7. URL: http://www.sciencedirect.com/science/article/pii/0375947487906257.

[69] J. Schirmer et al. "Double Gamma Decay in ^{40}Ca and ^{90}Zr". In: *Phys. Rev. Lett.* 53 (20 Nov. 1984), pp. 1897–1900. DOI: 10.1103/PhysRevLett.53.1897. URL: https://link.aps.org/doi/10.1103/PhysRevLett.53.1897.

[70] E. Beardsworth et al. "Double Gamma Decay in ^{40}Ca". In: *Phys. Rev. C* 8 (1 July 1973), pp. 216–229. DOI: 10.1103/PhysRevC.8.216. URL: https://link.aps.org/doi/10.1103/PhysRevC.8.216.

[71] E. R. Mucciolo and O. Helene. "Double gamma decay in ^{90}Zr". In: *Phys. Rev. C* 40 (5 Nov. 1989), pp. 2403–2405. DOI: 10.1103/PhysRevC.40.2403. URL: https://link.aps.org/doi/10.1103/PhysRevC.40.2403.

[72] N Pietralla et al. "First observation of the competitive double-gamma ($\gamma\gamma/\gamma$) decay process". In: *Journal of Physics: Conference Series* 724.1 (2016), p. 012039. URL: http://stacks.iop.org/1742-6596/724/i=1/a=012039.

[73] C. Walz et al. "Observation of the competitive double-gamma nuclear decay". In: *Nature* 526 (Oct. 2015), pp. 406–409. DOI: 10.1038/nature15543. URL: http://dx.doi.org/10.1038/nature15543.

[74] Kenneth S. Krane and David Halliday. *Introductory Nuclear Physics*. 3rd ed. Wiley, 1987.

[75] Kris Heyde and John L. Wood. "Shape coexistence in atomic nuclei". In: *Rev. Mod. Phys.* 83 (4 Nov. 2011), pp. 1467–1521. DOI: 10.1103/RevModPhys.83.1467. URL: https://link.aps.org/doi/10.1103/RevModPhys.83.1467.

[76] Katarzyna Szymanska-Mertens et al. "Resolution, efficiency and stability of HPGe detector operating in a magnetic field at various gamma-ray energies". In: *Nuclear Instruments and Methods in Physics Research Section A: Accelerators, Spectrometers, Detectors and Associated Equipment* 592 (July 2008), pp. 486–492. DOI: 10.1016/j.nima.2008.04.017.

[77] A Lorente et al. "Performance of HPGe Detectors in High Magnetic Fields". In: *Nuclear Instruments and Methods in Physics Research Section A: Accelerators, Spectrometers, Detectors and Associated Equipment* 573 (Apr. 2007), pp. 410–417. DOI: 10.1016/j.nima.2006.12.030.

[78] M. Agnello et al. "Study of the performance of HPGe detectors operating in very high magnetic fields". In: *Nuclear Instruments and Methods in Physics Research Section A: Accelerators, Spectrometers, Detectors and Associated Equipment* 606 (July 2009), pp. 560–568. DOI: 10.1016/j.nima.2009.04.035.

[79] E. Belau et al. "Charge collection in silicon strip detectors". In: *Nuclear Instruments and Methods in Physics Research* 214.2 (1983), pp. 253–260. ISSN: 0167-5087. DOI: https://doi.org/10.1016/0167-5087(83)90591-4. URL: http://www.sciencedirect.com/science/article/pii/0167508783905914.

[80] A. Castoldi et al. "Performance of silicon drift detectors in a magnetic field". In: *Nuclear Instruments and Methods in Physics Research Section A: Accelerators, Spectrometers, Detectors and Associated Equipment* 399.2 (1997), pp. 227–243. ISSN: 0168-9002. DOI: https://doi.org/10.1016/S0168-9002(97)00909-1. URL: http://www.sciencedirect.com/science/article/pii/S0168900297009091.

[81] S.U. Pandey et al. "Transport properties of electrons in silicon drift detectors measured in large magnetic fields". In: *Nuclear Instruments and Methods in Physics Research Section A: Accelerators, Spectrometers, Detectors and Associated Equipment* 383.2 (1996), pp. 537–546. ISSN: 0168-9002. DOI: https://doi.org/10.1016/S0168-9002(96)00778-4. URL: http://www.sciencedirect.com/science/article/pii/S0168900296007784.

[82] Gerhard Lutz. *Semiconductor Radiation Detectors*. 1st ed. Springer-Verlag Berlin Heidelberg, 1999.

[83] Helmuth Spieler. *Semiconductor detector systems*. 1st ed. Series on semiconductor science and technology, 12. Oxford University Press, 2005.

[84] Glenn F. Knoll. *Radiation Detection and Measurement*. 4th ed. Wiley, 2010.

[85] F. N. Flakus. "Detecting and measuring ionizing radiation -a short history". In: *IAEA Bulletin* 23 (4 Dec. 1981), pp. 31–36. ISSN: 0020-6067.

[86] Jr. Hastings A. Smith and Marcia Lucas. *Passive Nondesctructive Assay Manual – PANDA*. accessed: 22-05-2018. URL: http://www.lanl.gov/orgs/n/n1/panda/.

[87] J. B. Birks. *The Theory and Practice of Scintillation Counting*. Ed. by J. B. Birks. 1964. DOI: https://doi.org/10.1016/B978-0-08-010472-0.50006-9. URL: http://www.sciencedirect.com/science/article/pii/B9780080104720500069.

[88] G. R. Gilmore. "Radioactive Decay and the Origin of Gamma and X-Radiation". In: *Practical Gamma-Ray Spectrometry*. Wiley-Blackwell, 2008. Chap. 1, pp. 1–24. ISBN: 9780470861981. DOI: 10.1002/9780470861981.ch1. eprint: https://onlinelibrary.wiley.com/doi/pdf/10.1002/9780470861981.ch1. URL: https://onlinelibrary.wiley.com/doi/abs/10.1002/9780470861981.ch1.

[89] R. D. Evans. *The Atomic Nucleus*. 1st ed. McGraw-Hill Book Company, 1955.

[90] J. Eberth and J. Simpson. "From Ge(Li) detectors to gamma-ray tracking arrays–50 years of gamma spectroscopy with germanium detectors". In: *Progress in Particle and Nuclear Physics* 60.2 (2008), pp. 283–337. ISSN: 0146-6410. DOI: https://doi.org/10.1016/j.ppnp.2007.09.001. URL: http://www.sciencedirect.com/science/article/pii/S0146641007000828.

[91] Paul E. Koehler, Stephen A. Wender, and Jon S. Kapustinsky. "Improvements in the energy resolution and high-count-rate performance of bismuth germanate". In: *Nuclear Instruments and Methods in Physics Research Section A: Accelerators, Spectrometers, Detectors and Associated Equipment* 242.3 (1986), pp. 369–372. ISSN: 0168-9002. DOI: https://doi.org/10.1016/0168-9002(86)

90431-6. URL: http://www.sciencedirect.com/science/article/pii/0168900286904316.

[92] L.J. Arnold et al. "Portable gamma spectrometry with cerium-doped lanthanum bromide scintillators: Suitability assessments for luminescence and electron spin resonance dating applications". In: *Radiation Measurements* 47.1 (2012), pp. 6–18. ISSN: 1350-4487. DOI: https://doi.org/10.1016/j.radmeas.2011.09.001. URL: http://www.sciencedirect.com/science/article/pii/S1350448711004422.

[93] J.M Hollander. "The impact of semiconductor detectors on gamma-ray and electron spectroscopy". In: *Nuclear Instruments and Methods* 43.1 (1966). Proceedings of the Tenth Summer Meeting of Nuclear Physicists, pp. 65–109. ISSN: 0029-554X. DOI: https://doi.org/10.1016/0029-554X(66)90533-7. URL: http://www.sciencedirect.com/science/article/pii/0029554X66905337.

[94] W. L. Hansen. "High-purity germanium crystal growing". In: *Nuclear Instruments and Methods* 94.2 (1971), pp. 377–380. DOI: 10.1016/0029-554X(71)90593-3.

[95] R. N. Hall and T. J. Soltys. "High Purity Germanium for Detector Fabrication". In: *IEEE Transactions on Nuclear Science* 18.1 (Feb. 1971), pp. 160–165. ISSN: 0018-9499. DOI: 10.1109/TNS.1971.4325857.

[96] I Y Lee, M A Deleplanque, and K Vetter. "Developments in large gamma-ray detector arrays". In: *Reports on Progress in Physics* 66.7 (2003), p. 1095. URL: http://stacks.iop.org/0034-4885/66/i=7/a=201.

[97] Kai Vetter. "Recent Developments in the Fabrication and Operation of Germanium Detectors". In: *Annual Review of Nuclear and Particle Science* 57.1 (2007), pp. 363–404. DOI: 10.1146/annurev.nucl.56.080805.140525. eprint:

https://doi.org/10.1146/annurev.nucl.56.080805.140525. URL: https://doi.org/10.1146/annurev.nucl.56.080805.140525.

[98] J.R. Fiebiger and R.S. Muller. "Pair-Production Energies in Silicon and Germanium Bombarded with Low-Energy Electrons". In: *Journal of Applied Physics* 43.7 (1972), pp. 3202–3207. DOI: 10.1063/1.1661685. eprint: https://doi.org/10.1063/1.1661685. URL: https://doi.org/10.1063/1.1661685.

[99] ORTEC. *Review of the physics of semiconductor detectors*. accessed: 25-05-2018. URL: https://www.ortec-online.com/-/media/ametekortec/catalog%20files/detectors.pdf?la=en.

[100] Q. Looker, M. Amman, and K. Vetter. "Leakage current in high-purity germanium detectors with amorphous semiconductor contacts". In: *Nuclear Instruments and Methods in Physics Research Section A: Accelerators, Spectrometers, Detectors and Associated Equipment* 777 (2015), pp. 138–147. ISSN: 0168-9002. DOI: https://doi.org/10.1016/j.nima.2014.12.104. URL: http://www.sciencedirect.com/science/article/pii/S0168900215000066.

[101] Zhong He. "Review of the Shockley–Ramo theorem and its application in semiconductor gamma-ray detectors". In: *Nuclear Instruments and Methods in Physics Research Section A: Accelerators, Spectrometers, Detectors and Associated Equipment* 463.1 (2001), pp. 250–267. ISSN: 0168-9002. DOI: https://doi.org/10.1016/S0168-9002(01)00223-6. URL: http://www.sciencedirect.com/science/article/pii/S0168900201002236.

[102] W. Shockley. "Currents to Conductors Induced by a Moving Point Charge". In: *Journal of Applied Physics* 9.10 (1938), pp. 635–636. DOI: 10.1063/1.1710367. eprint: https://doi.org/10.1063/1.1710367. URL: https://doi.org/10.1063/1.1710367.

[103] S. Ramo. "Currents Induced by Electron Motion". In: *Proceedings of the IRE* 27.9 (Sept. 1939), pp. 584–585. ISSN: 0096-8390. DOI: 10.1109/JRPROC.1939.228757.

[104] Uri Lachish. "The role of contacts in semiconductor gamma radiation detectors". In: *Nuclear Instruments and Methods in Physics Research Section A: Accelerators, Spectrometers, Detectors and Associated Equipment* 403.2 (1998), pp. 417–424. ISSN: 0168-9002. DOI: https://doi.org/10.1016/S0168-9002(97)01100-5. URL: http://www.sciencedirect.com/science/article/pii/S0168900297011005.

[105] G. Forcinal. "Efficiency of Ge(Li) thin window detectors near absorption edge of germanium". In: *Nuclear Instruments and Methods* 107.1 (1973), pp. 125–129. ISSN: 0029-554X. DOI: https://doi.org/10.1016/0029-554X(73)90022-0. URL: http://www.sciencedirect.com/science/article/pii/0029554X73900220.

[106] Nora L. Maidana et al. "Efficiency calibration of x-ray HPGe detectors for photons with energies above the Ge K binding energy". In: *Nuclear Instruments and Methods in Physics Research Section A: Accelerators, Spectrometers, Detectors and Associated Equipment* 729 (2013), pp. 371–380. ISSN: 0168-9002. DOI: https://doi.org/10.1016/j.nima.2013.07.033. URL: http://www.sciencedirect.com/science/article/pii/S0168900213010097.

[107] N.Q. Huy, D.Q. Binh, and V.X. An. "Study on the increase of inactive germanium layer in a high-purity germanium detector after a long time operation applying MCNP code". In: *Nuclear Instruments and Methods in Physics Research Section A: Accelerators, Spectrometers, Detectors and Associated Equipment* 573.3 (2007), pp. 384–388. ISSN: 0168-9002. DOI: https://doi.org/10.

1016/j.nima.2006.12.048. URL: http://www.sciencedirect.com/science/article/pii/S0168900207001118.

[108] C. Fleischmann et al. "Impact of ammonium sulfide solution on electronic properties and ambient stability of germanium surfaces: towards Ge-based microelectronic devices". In: *J. Mater. Chem. C* 1 (26 2013), pp. 4105–4113. DOI: 10.1039/C3TC30424H. URL: http://dx.doi.org/10.1039/C3TC30424H.

[109] G. Maggioni et al. "Characterization of different surface passivation routes applied to a planar HPGe detector". In: *The European Physical Journal A* 51.11 (Nov. 2015), p. 141. ISSN: 1434-601X. DOI: 10.1140/epja/i2015-15141-9. URL: https://doi.org/10.1140/epja/i2015-15141-9.

[110] H. Utsunomiya et al. "Surface channel effect on γ-ray response functions of coaxial germanium detectors". In: *Nuclear Instruments and Methods in Physics Research Section A: Accelerators, Spectrometers, Detectors and Associated Equipment* 548.3 (2005), pp. 455–463. ISSN: 0168-9002. DOI: https://doi.org/10.1016/j.nima.2005.04.062. URL: http://www.sciencedirect.com/science/article/pii/S0168900205010508.

[111] E.L. Hull et al. "Temperature sensitivity of surface channel effects on high-purity germanium detectors". In: *Nuclear Instruments and Methods in Physics Research Section A: Accelerators, Spectrometers, Detectors and Associated Equipment* 364.3 (1995), pp. 488–495. ISSN: 0168-9002. DOI: https://doi.org/10.1016/0168-9002(95)00339-8. URL: http://www.sciencedirect.com/science/article/pii/0168900295003398.

[112] H. L. Malm and R. J. Dinger. "Charge collection in surface channels on high-purity ge detectors". In: *IEEE Transactions on Nuclear Science* 23 (1 Feb. 1976), pp. 75–80. DOI: 10.1109/TNS.1976.4328218.

[113] D. A. Landis et al. “Transistor Reset Preamplifier for High Rate High Resolution Spectroscopy”. In: *IEEE Transactions on Nuclear Science* 29.1 (Feb. 1982), pp. 619–624. ISSN: 0018-9499. DOI: 10.1109/TNS.1982.4335922.

[114] *MDPP-16 SCP/RCP Datasheet*. version V00.16. Mesytec GmbH & Co. KG. URL: https://www.mesytec.com/products/nuclear-physics/MDPP-16.html.

[115] L.A. McNelles and J.L. Campbell. “Analytic approximations to peak shapes produced by Ge(Li) and Si(Li) spectrometers”. In: *Nuclear Instruments and Methods* 127.1 (1975), pp. 73–81. ISSN: 0029-554X. DOI: https://doi.org/10.1016/0029-554X(75)90304-3. URL: http://www.sciencedirect.com/science/article/pii/0029554X75903043.

[116] H.H. Jorch and J.L. Campbell. “On the analytic fitting of full energy peaks from Ge(Li) and Si(Li) photon detectors”. In: *Nuclear Instruments and Methods* 143.3 (1977), pp. 551–559. ISSN: 0029-554X. DOI: https://doi.org/10.1016/0029-554X(77)90246-4. URL: http://www.sciencedirect.com/science/article/pii/0029554X77902464.

[117] J.L. Campbell and H.H. Jorch. “On the analytic fitting of full energy peaks from Ge(Li) and Si(Li) photon detectors. II”. In: *Nuclear Instruments and Methods* 159.1 (1979), pp. 163–170. ISSN: 0029-554X. DOI: https://doi.org/10.1016/0029-554X(79)90344-6. URL: http://www.sciencedirect.com/science/article/pii/0029554X79903446.

[118] David Radford. *Radware*. https://radware.phy.ornl.gov/.

[119] R. G. Helmer and M. A. Lee. “Analytical functions for fitting peaks from Ge semiconductor detectors”. In: *Nuclear Instruments and Methods* 178.2 (1980), pp. 499–512. ISSN: 0029-554X. DOI: https://doi.org/10.1016/0029-

554X(80)90830-7. URL: http://www.sciencedirect.com/science/article/pii/0029554X80908307.

[120] D. J. Griffiths. *Introduction to electrodynamics*. 4th ed. Cambridge University Press, 2017.

[121] C. S. Hung and J. R. Gliessman. "Resistivity and Hall Effect of Germanium at Low Temperatures". In: *Phys. Rev.* 96 (5 Dec. 1954), pp. 1226–1236. DOI: 10.1103/PhysRev.96.1226. URL: https://link.aps.org/doi/10.1103/PhysRev.96.1226.

[122] P. E. Siska. "Molecular-beam studies of Penning ionization". In: *Rev. Mod. Phys.* 65 (2 Apr. 1993), pp. 337–412. DOI: 10.1103/RevModPhys.65.337. URL: https://link.aps.org/doi/10.1103/RevModPhys.65.337.

[123] Duc T. Vo. *Comparisons of the DSPEC and DSPEC Plus spectrometer systems*. Tech. rep. LA-13671-MS. Los Alamos National Laboratory, Los Alamos, NM (US), Nov. 1999. DOI: 10.2172/752375.

[124] *Wavesurfer-3054*. accessed: 07-07-2018. Teledyne LeCroy. URL: http://teledynelecroy.com/oscilloscope/wavesurfer-3000-oscilloscopes/wavesurfer-3054.

[125] Matthew Newville et al. "LMFIT: Non-Linear Least-Square Minimization and Curve-Fitting for Python". In: (Sept. 2014). DOI: 10.5281/zenodo.11813.

[126] T. S. Buys and K. De Clerk. "Bi-Gaussian fitting of skewed peaks". In: *Analytical Chemistry* 44.7 (1972), pp. 1273–1275. DOI: 10.1021/ac60315a005. eprint: https://doi.org/10.1021/ac60315a005. URL: https://doi.org/10.1021/ac60315a005.

[127] Zygmunt Patyk et al. "Orbital electron capture decay of hydrogen- and helium-like ions". In: *Phys. Rev. C* 77 (1 Jan. 2008), p. 014306. DOI: 10.1103/PhysRevC.77.014306. URL: https://link.aps.org/doi/10.1103/PhysRevC.77.014306.

[128] Yu. A. Litvinov et al. "Measurement of the β^+ and Orbital Electron-Capture Decay Rates in Fully Ionized, Hydrogenlike, and Heliumlike ^{140}Pr Ions". In: *Phys. Rev. Lett.* 99 (26 Dec. 2007), p. 262501. DOI: 10.1103/PhysRevLett.99.262501. URL: https://link.aps.org/doi/10.1103/PhysRevLett.99.262501.

[129] N. Winckler et al. "Orbital electron capture decay of hydrogen- and helium-like ^{142}Pm ions". In: *Physics Letters B* 679.1 (2009), pp. 36–40. ISSN: 0370-2693. DOI: https://doi.org/10.1016/j.physletb.2009.07.019. URL: http://www.sciencedirect.com/science/article/pii/S0370269309008296.

[130] D. R. Atanasov et al. "Half-life measurements of stored fully ionized and hydrogen-like 122 I ions". In: *The European Physical Journal A* 48.2 (Feb. 2012), p. 22. ISSN: 1434-601X. DOI: 10.1140/epja/i2012-12022-9. URL: https://doi.org/10.1140/epja/i2012-12022-9.

[131] *X Ray Mass Attenuation Coefficients*. accessed: 14-12-2018. URL: https://www.nist.gov/pml/x-ray-mass-attenuation-coefficients.

[132] D. Radford. *International Workshop on Germanium Radiation Detector Technology 2017*. personal communication. Dec. 2017. URL: https://sites.google.com/a/lbl.gov/intl-germanium-workshop/.